The Dissertation Committee for Matthew Scott Walters
certifies that this is the approved version of the following dissertation:

Dynamic Modeling of Post-Combustion Amine Scrubbing for Process Control Strategy Development

Committee:

Gary T. Rochelle, Supervisor

Thomas F. Edgar, Supervisor

Michael Baldea

Maruthi R. Akella

Eric Chen

Dynamic Modeling of Post-Combustion Amine Scrubbing for Process Control Strategy Development

by

Matthew Scott Walters, BS ChE, BS Chem, MSE

DISSERTATION

Presented to the Faculty of the Graduate School of

The University of Texas at Austin

in Partial Fulfillment

of the Requirements

for the Degree of

DOCTOR OF PHILOSOPHY

THE UNIVERSITY OF TEXAS AT AUSTIN

May 2016

Dedicated to my family, friends, and groupmates.

Acknowledgments

I want to acknowledge the many people who, throughout my life, have helped me reach the point of completing my PhD. First and most importantly, I would like to thank my mother and late father who always believed in me. Without their love and encouragement, I would not have been half the person I am today. I have been blessed with a wonderful family, and I am deeply grateful for the support they have provided to me over the years.

Next I would like to thank my academic advisers, Dr. Gary Rochelle and Dr. Thomas Edgar. I can confidently say that I am a much smarter person as a result of working under these two brilliant engineers for the past five years. Through our weekly meetings, Dr. Rochelle has helped tune my intuition for process engineering. By observing the way Dr. Rochelle approaches problems, I have learned how to ask intelligent questions to be able to understand complicated subjects. Dr. Edgar has provided me with invaluable insight into process control, both through his course and feedback on my work. I have also learned several soft skills from Dr. Edgar, such as how to tailor a presentation to a specific audience, that will help me to effectively communicate my ideas in future endeavors.

I am very appreciative of my groupmates who made graduate school more enjoyable. We suffered through seemingly insurmountable obstacles, but were able to persevere together. My groupmates were always willing to put down what they were doing to answer a technical question or to just have a casual conversation when I needed a break from research. Thank you all for making graduate school a positive experience for me.

While there are too many people who influenced my life leading up to graduate school to thank each of them individually, I would like acknowledge some that stand out in my mind. I want to thank my high school cross country coach, Jeremy Fisher, for instilling a sense of relentlessness in me that I have been able to apply to everything I do. I also want to express my gratitude to the generous donors at Eli Lilly who enabled me to attend Purdue University on scholarship to earn my undergraduate degree. I would not have been able to afford to attend a top ranked engineering school without this gift. I want to thank Dr. Ramachandran at Purdue for giving me the opportunity to perform undergraduate research in his lab, which undoubtedly helped prepare me for my graduate school career. I would also like to thank my friends. You are the people who make me laugh, listen to me when I complain about research, and give me something to look forward to when I leave work. I value having each and every one of you in my life.

Lastly, I want to acknowledge the financial support of the Texas Carbon Management Program, the Cockrell School of Engineering Abell Chair Endowment, and the Cockrell School of Engineering Thrust 2000 Fellowship.

Dynamic Modeling of Post-Combustion Amine Scrubbing for Process Control Strategy Development

Matthew Scott Walters, Ph.D.
The University of Texas at Austin, 2016

Supervisors: Gary T. Rochelle
Thomas F. Edgar

Intensified process designs with advanced solvents have been proposed to decrease both capital and operating costs of post-combustion carbon capture with amine scrubbing. These advanced flowsheets create process control challenges because process variables are designed to operate near constraints and the degrees of freedom are increased due to heat recovery. Additionally, amine scrubbing is tightly integrated with the upstream power plant and downstream enhanced oil recovery (EOR) facility. This work simulated an amine scrubbing plant that uses an intercooled absorber and advanced flash stripper configuration with aqueous piperazine to capture CO_2 from a 550 MWe coal-fired power plant. The objective of this research was to develop a process control strategy that resulted in favorable closed-loop dynamics and near-optimal conditions in response to disturbances and off-design operation.

Two models were created for dynamic simulation of the amine scrubbing system: a medium-order model of an intercooled absorber column and a low-order model of the

entire plant. The purpose of the medium-order model was to accurately predict the absorber temperature profile in order to identify a column temperature that can be controlled by manipulating the solvent circulation rate to maintain a constant liquid to gas ratio. The low-order model, which was shown to sufficiently represent dynamic process behavior through validation with pilot plant data, was used to develop a plantwide control strategy.

A regulatory control layer was implemented and tested with bounding cases that represent either electricity generation requirements, CO_2 emission regulations, or EOR constraints dominating the control strategy. Satisfying the operational and economic objectives of one system component was found to result in unfavorable dynamic performance for the remainder of the system. Self-optimizing control variables were identified for the energy recovery flowrates of the advanced flash stripper that maintained good energy performance in off-design conditions.

Regulatory control alone could not satisfactorily achieve the set point for CO_2 removal rate from the flue gas. A supervisory model predictive controller was developed that manipulates the set point for the stripper pressure controller in order to control removal. The straightforward single-input, single-output constrained linear model predictive controller exhibited a significant improvement compared to PI control alone.

Table of Contents

List of Tables

List of Figures

Chapter 1

Introduction

Carbon dioxide (CO_2) is the largest anthropogenic source of greenhouse gas (GHG) emissions and is known to be a major cause of climate change (IEA, 2015). The rise in global temperature as a result of GHGs has been implicated in melting glaciers (Radić et al., 2014), rising sea levels (Hinkel et al., 2014), acidification of marine ecosystems (Kroeker et al., 2013; Doney et al., 2009), intensified drought (Trenberth et al., 2014), increased ultraviolet-B radiation (Hegglin and Shepherd, 2009), and increased fire frequency (Bowman et al., 2009), all of which threaten biodiversity (Pimm et al., 2014) and human food supplies (Rosenzweig et al., 2014). Electricity generation accounts for nearly a third of U.S. GHG emissions, with coal-fired power plants responsible for a 40% share of total electricity generation in 2014 (EIA, 2015). It is therefore desirable to mitigate CO_2 emissions from large, point source electricity generation power plants through carbon capture and sequestration (CCS) technology in order to slow global climate change. Figure 1.1 shows IEA CO_2 emissions projections for a "business as usual" scenario and predicts the action required to limit the rise in average global temperature to 2 °C (IEA, 2015). While the bulk of emission reductions will likely come from higher penetration of renewables, increases in both generation and end-use efficiencies, and fuel switching, CCS is projected to be a critical CO_2 abatement strategy.

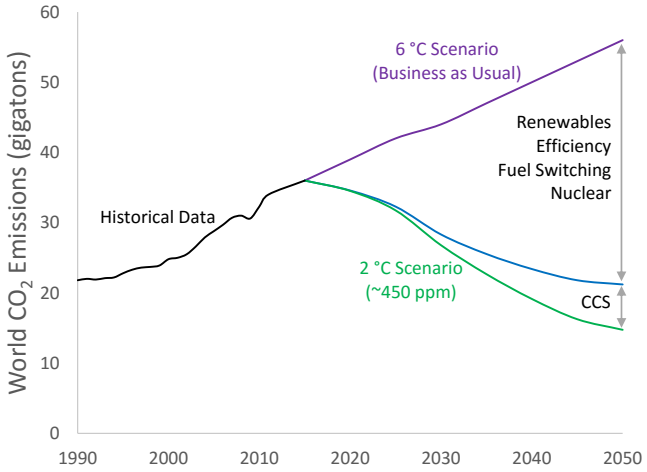

Figure 1.1: Historical CO_2 emissions and IEA projections for the 6 °C Scenario, which is largely an extrapolation of current trends, and the 2 °C Scenario, which lays out a pathway that will give at least a 50% chance of limiting the rise of average global temperature to 2 °C (IEA, 2015)

One of the leading technologies for post-combustion CCS is aqueous amine scrubbing (Rochelle, 2009; Boot-Handford et al., 2014), which is a commercially demonstrated process for capturing CO_2 from coal-fired power plant emissions (Stéphenne, 2014; Scherffius et al., 2013). The research presented here is focused on dynamic modeling and process control strategy development for amine scrubbing. The goal of this work is to improve operational stability, energy performance, and process economics, thereby advancing the feasibility of widespread deployment of amine scrubbing for CCS from power plants.

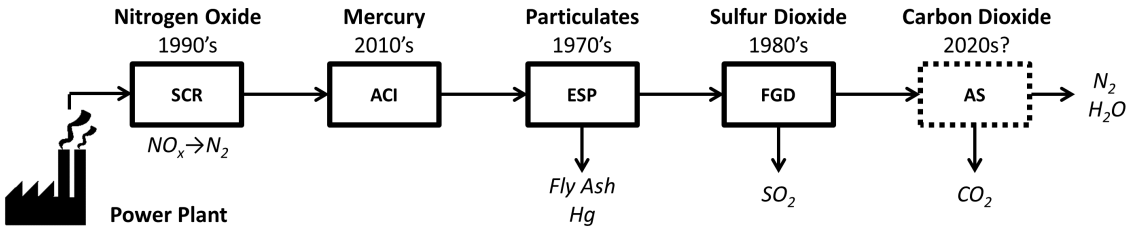

Figure 1.2: Pollution control steps for coal-fired power plants

1.1 Regulation of CO_2 Emissions

The Supreme Court case Massachusetts v. EPA (2007) classified CO_2 as a pollutant under the Clean Air Act (CAA), requiring the EPA to regulate CO_2 emissions. New source performance standards have already been implemented by the EPA to limit power plant emissions at the level of a natural gas combined cycle plant (EPA, 2016), and there are pending existing source standards (EPA, 2015). The CAA has long been used to regulate post-combustion power plant emissions. As shown in Figure 1.2, electrostatic precipitation (ESP) for particulate removal, flue gas desulfurization (FGD) for SO_2 removal, selective catalytic reduction (SCR) to reduce NOx to N_2, and activated carbon injection (ACI) for mercury removal have been added to coal-fired power plants over the past several decades because of EPA and state regulations. Amine scrubbing is a tail-end technology that will allow power plant operators to comply with future EPA rules, just as other post-combustion pollution control technologies have historically facilitated the control of particulates, sulfur dioxide, nitrogen oxide, and mercury as a result of EPA regulation.

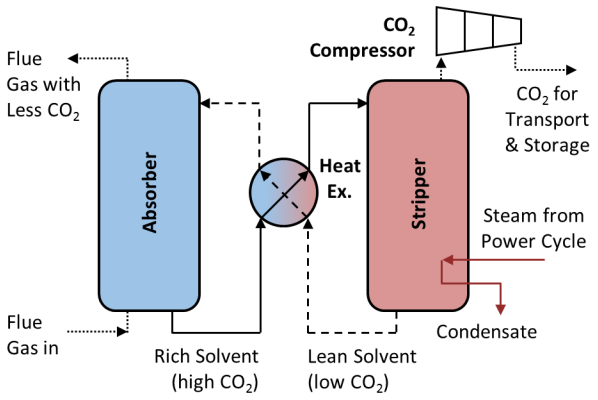

Figure 1.3: Basic flowsheet of an amine scrubbing plant

1.2 Overview of Amine Scrubbing

The main operating units of amine scrubbing are an absorber, stripper, and cross heat exchanger, as shown in Figure 1.3. Amine scrubbing is a heat-driven, thermal-swing process: CO_2 in the flue gas is absorbed by an amine solvent in a low-temperature absorber, and then the CO_2-rich solvent is heated in a stripper to regenerate gaseous CO_2. The heat required for regeneration is derived by extracting low-quality steam from the power plant turbines, and the efficiency of the process depends on effective cross exchange between the hot and cold solvent. The CO_2 exiting the stripper is compressed to 150 bar for geological sequestration.

1.2.1 Baseline MEA Process

Previous dynamic modeling studies have exclusively considered the basic process shown in Figure 1.3 with monoethanolamine (MEA) solvent, as summarized in Table 1.1. This configuration is commercially proven for acid gas treating and is commonly used as a case study for post-combustion CO_2 capture. However, the basic process may not be

Table 1.1: Previously published plantwide amine scrubbing dynamic models

	Solvent	Absorber	Stripper
Lin et al. (2011)	MEA	Simple	Reboiled
Lawal et al. (2012)	MEA	Simple	Reboiled
Ziaii-Fashami (2012)	MEA	Simple	Reboiled
Ceccarelli et al. (2014)	MEA	Simple	Reboiled
Nittaya et al. (2014)	MEA	Simple	Reboiled
Enaasen Flø et al. (2015)	MEA	Simple	Reboiled

representative of an optimized system, which contains additional degrees of freedom due to energy integration and operates closer to process constraints, for process control studies.

1.2.2 Advanced Amine Scrubbing Process

Because of the high capital cost and large energy penalty associated with CO_2 capture, a commercial plant will likely use an advanced solvent with an intensified process. This work considers an optimized process flowsheet and second generation solvent, described in the following subsections. The advanced amine scrubbing process is used as a case study for all modeling and control work that will be presented in subsequent chapters.

1.2.2.1 Piperazine as a Second Generation Solvent

Piperazine (PZ) has been identified as a second generation solvent with superior properties to MEA (Rochelle et al., 2011). Additionally, PZ solvent properties are readily available in the literature and can incorporated into a process model. Table 1.2 compares key solvent properties of MEA and PZ. PZ is a fast solvent, and therefore the height of the

Table 1.2: Solvent properties comparison, with best value shown in bold (Rochelle et al., 2011)

Property	7 m MEA	8 m PZ	5 m PZ
Rate ($mol/Pa \cdot m^2 \cdot s$)	4.3	8.5	**11.3**
Capacity (mol CO_2/mol alkalinity)	0.5	**0.79**	0.63
Viscosity (cP @ 40 °C)	**2.5**	10.8	3
Degradation T (°C)	121	**163**	**163**
Max Stripper P (bar)	2.2	**14.3**	**14.3**

absorber column is smaller than a system with MEA. Because PZ has a higher degradation temperature than MEA, the stripper can be operated at a higher pressure for superior energy performance. PZ is used as the amine in this work to examine a system that will likely be more representative of a future commercial solvent than MEA.

Two drawbacks to PZ are its relatively high viscosity compared to MEA and solid solubility issues (Ma et al., 2012). 5 molal (m) PZ was selected over 8 m PZ for this work because of the reduced viscosity and wider solid solubility window. The improvement in viscosity, and therefore the heat transfer coefficient, likely outweighs the decrease in solvent capacity. The high temperature/high pressure stripping operation creates safety constraints that must be considered during process control strategy development.

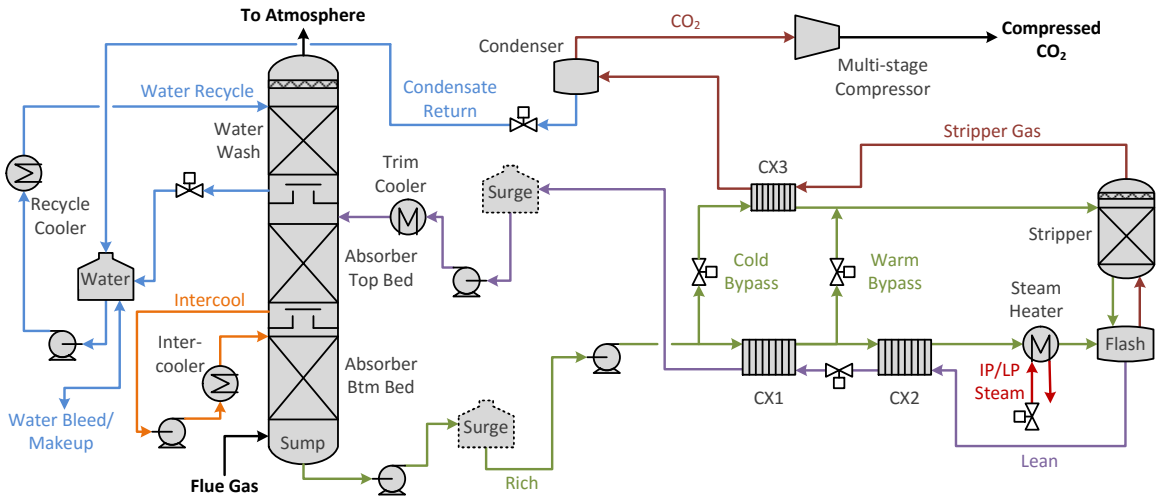

Figure 1.4: In-and-out intercooled absorber with advanced flash stripper configuration

1.2.2.2 Optimized Process Flowsheet

The optimized process configuration used in this work is an in-and-out intercooled absorber with the advanced flash stripper (Figure 1.4). Absorber intercooling reduces the required solvent flowrate and height of structured packing by decreasing the temperature bulge in the column that results from the exothermic absorption of CO_2 (Sachde and Rochelle, 2014). The energy performance of the advanced flash stripper configuration is better than a reboiled stripper due to the effective recovery of stripping steam heat (Lin et al., 2014). However, this configuration increases process complexity because of the increased number of heat exchangers compared to the simple absorber and reboiled stripper configuration.

1.3 Process Control Challenges

Amine scrubbing is not a new technology; it is widely used for removing CO_2 from natural gas and hydrogen, with the basic process patented in 1930 (Bottoms, 1930). However, the throughput of an amine scrubbing plant that treats flue gas from a commercial scale power plant will be an order of magnitude larger than the throughput of a natural gas processing facility. Additionally, capital cost has been the dominant consideration in the design of amine plants for current applications, whereas operating cost is likely more important for CCS from power plants. It is estimated that the parasitic power demand of the system is equivalent to 20–25% of typical power plant output as a result of steam draw-off for solvent regeneration and compression for geological sequestration (Lin and Rochelle, 2016). Finally, operation is dependent on the upstream power plant and downstream compressor, making amine scrubbing in CCS a highly integrated, complex system. Because of this increased scale, energy demand, and complexity, there is a significant need for research in the optimum design, operation, and control of the system prior to widespread commercial scale implementation.

1.3.1 Hierarchical Process Control

A hierarchical approach is taken for designing a process control strategy for the amine scrubbing system, described by Figure 1.5 (Seborg et al., 2011; Scattolini, 2009). The first level of process control is the regulatory control layer, which consists of feedback and feedforward controllers that regulate a process to its steady state in the presence of disturbances and set point changes. The next level is the supervisory model predictive control (MPC) layer, which is responsible for coordinating the action of the individual control

loops of the regulatory control layer. The top level is real-time optimization (RTO), which regularly calculates new optimum controller set point values based on changing economic factors. RTO is not explicitly considered in this work, although realistic changes in process set points that could result from RTO are examined when evaluating control strategy performance. The reader is referred to the work of Cohen (2012) for further information on RTO of amine scrubbing.

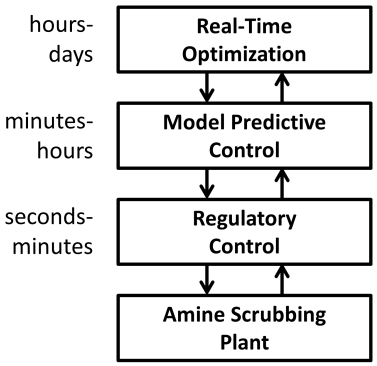

Figure 1.5: Hierarchy of process control (Seborg et al., 2011; Scattolini, 2009)

1.4 Research Summary

There were two primary components of this research: (1) dynamic modeling and (2) process control strategy development. A low-order, control relevant dynamic model of the amine scrubbing plant was formulated and validated with pilot plant data. The low-order model was used as a tool for evaluating proposed control structures. A medium-order dynamic model of CO_2 absorption was also created to explore the dynamics of the absorber column temperature profile. A regulatory control strategy was developed, taking into account competing objectives between the capture plant, power plant, and enhanced oil

recovery facility. Controlling the performance of the heat integrated advanced flash stripper and intercooled absorber was also addressed. Finally, supervisory model-based control was used to account for the higher-level system objective of maintaining a desired CO_2 removal rate from the flue gas.

The dissertation is organized as follows:

- Chapter 2: Literature review of process modeling and control of amine scrubbing (Walters et al., 2016b,c)
- Chapter 3: Low-order dynamic model development and validation for the advanced amine scrubbing process configuration (Walters et al., 2016c)
- Chapter 4: Demonstration of time scale multiplicity for key process variables using singular perturbation analysis (Walters et al., 2014)
- Chapter 5: Regulatory control strategy recommendations for varying system objectives (Walters et al., 2016b)
- Chapter 6: Identification of self-optimizing controlled variables for the advanced flash stripper (Walters et al., 2016d)
- Chapter 7: Medium-order dynamic absorber model development and L/G control (Walters et al., 2016a)
- Chapter 8: Implementation and evaluation of a supervisory model predictive controller
- Chapter 9: Conclusions and recommendations

Chapter 2

Literature Review

2.1 First Principles Modeling of Amine Scrubbing

There are limited examples of equation-based plantwide dynamic models of post-combustion amine scrubbing in the literature. Ziaii-Fashami (2012) developed a dynamic model of the absorber/stripper process in Aspen Custom Modeler® for a 100 MWe coal-fired power plant, but did not perform any validation to quantify model performance. Enaasen Flø et al. (2015) implemented a dynamic pilot plant model in MATLAB® and performed both steady state and dynamic model validation. Nittaya et al. (2014) created a model in gPROMS® for capture from a 750 MWe coal-fired power plant. The absorber from this model was validated using steady state pilot plant data in previous work (Harun et al., 2012). Lawal et al. (2012) presented a dynamic model formulation that was implemented in gPROMS® to simulate a pilot plant scale system, as well as a full-scale 500 MWe coal-fired power plant. The pilot-scale model was validated with steady state pilot plant data. Ceccarelli et al. (2014) used Process System Enterprise's proprietary gCCS package in gPROMS® to capture CO_2 from a 350 MWe NGCC plant but did not provide any model validation. All of the previous research presented here used monoethanolamine (MEA) as the solvent with the basic process configuration shown in Figure 1.3.

There are five fundamental model components necessary to create a plantwide amine scrubbing model (either steady state or dynamic): flow type, thermodynamics, transport, kinetics, and contactor and exchanger characteristics. The following discussion briefly reviews the various levels of complexity with which these properties can be incorporated into the overall model.

2.1.1 Flow Type

Flow type refers to how the bulk properties of a fluid are calculated along the spatial dimension of the flow in columns or heat exchangers. Discretized partial differential equations represent a plug flow regime in a distributed model, while a lumped model uses ordinary differential equations at one or more well-mixed nodes to approximate the distributed system (Oh and Pantelides, 1996). Equations 2.1a–2.1b show a liquid side mole balance on component i for structured packing using distributed and lumped models, respectively:

$$\frac{\partial\left(\varepsilon C_i^L\right)}{\partial t} = -\left(\frac{4}{\pi D^2}\right)\frac{\partial\left(x_i F^L\right)}{\partial Z} + N_i, \qquad Z/L \in [0,1) \tag{2.1a}$$

$$\frac{d\left(\varepsilon C_{i,k}^L\right)}{dt} = \left(\frac{4Ns}{\pi D^2 L}\right)\left(x_{i,k-1}F_{k-1}^L - x_{i,k}F_k^L\right) + N_{i,k}, \qquad \forall k \tag{2.1b}$$

where C is molar concentration, D is column diameter, F is molar flowrate, L is total length of the packing, N is volume-specific interphase molar transfer rate, Ns is the total number of well-mixed stages, x is liquid mole fraction, Z is the axial dimension, ε is liquid hold-up, superscript L refers to the liquid phase, and subscript k refers to the stage number. As $Ns \rightarrow \infty$, the lumped model approaches the distributed model.

2.1.2 Thermodynamics

Electrolyte activity coefficient models (Chen et al., 1982) are the recommended thermodynamic method to rigorously predict vapor-liquid equilibrium (VLE) of a CO_2-amine-water system (Austgen et al., 1989). This approach requires all true ionic species present in solution to be defined in the model. Figure 2.1 describes the difference between true and apparent species representations. Alternatively, a simplified semi-empirical model (Equation 2.2) was developed by Xu (2011) to calculate CO_2 VLE using the concentration of the apparent species in solution:

$$ln\left(P^*_{CO2}\right) = c_1 + c_2\frac{1}{T} + c_3\alpha + c_4\alpha^2 + c_5\frac{\alpha}{T} + c_6\frac{\alpha^2}{T} \tag{2.2}$$

where P^*_i is the equilibrium partial pressure, T is temperature, α is loading defined as moles CO_2/moles alkalinity, and c is a constant. The accompanying VLE relation for water (Equation 2.3), based on Raoult's Law, assumes no free CO_2 exists in solution:

$$P^*_{H2O} = \frac{x_{H2O}}{1 - x_{CO2}} P^{sat}_{H2O}\left(T\right) \tag{2.3}$$

where P^{sat}_{H2O} is the saturation pressure of water at a given T.

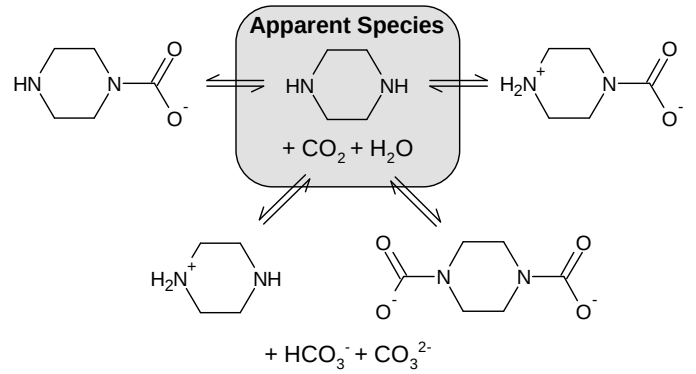

(a) The total apparent species (CO_2, PZ, H_2O) exist as true species in an electrolyte solution

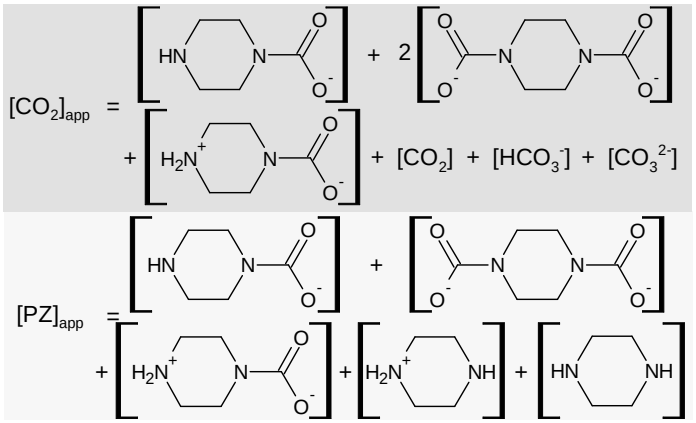

(b) Apparent concentration of CO_2 and PZ

Figure 2.1: True versus apparent species representation

In a thermodynamically consistent model, the heat of absorption of CO_2 (ΔH_{CO2}) and heat capacity of the loaded solution (Cp^L) should be related to the VLE (Lewis and Randall, 1923; Mathias and O'Connell, 2012). To simplify the calculation, ΔH_{CO2} and Cp^L may be treated as constants that can be adjusted to account for uncertainty in the energy balance.

2.1.3 Material and Energy Transport

CO_2 absorption and desorption is known to be a mass-transfer limited process, and therefore must be modeled using rate-based nonequilibrium equations (Taylor et al., 2003). The most sophisticated model for calculating multicomponent mass transfer through a two-film boundary layer is Maxwell-Stefan diffusion (Bird et al., 2002). The Maxwell-Stefan equations require binary diffusion coefficients for all species and therefore the true speciation must be known.

A simpler approach uses two-film resistance theory with an apparent species mass transfer coefficient. The amine can be assumed to be non-volatile ($N_{Am} = 0$) and O_2 and N_2 in the flue gas can assumed to be insoluble ($N_{O2}, N_{N2} = 0$) without significantly affecting the overall process dynamics. In general, there are $N_{comp} - 1$ independent flux equations, where N_{comp} is the number of components. It is valid to assume negligible bulk convection and write N_{comp} independent flux equations in the cases of: (1) low total flux, (2) presence of an inert in high concentration, or (3) equimolar counterdiffusion. Because the absorber gas is mostly insoluble N_2 and O_2 (case 2), the assumption holds in the absorber column. The stripper does not fall into any of the three cases for the negligible bulk convection assumption to be valid.

The two-film equations with apparent species mass transfer coefficients are given in Equations 2.4a–2.4d:

$$N_{i,k}^{L} = V_k k_{l,i} a\left(x_{i,k}^{I} - x_{i,k}\right) \tag{2.4a}$$

$$N_{i,k}^{V} = V_k k_{g,i} a\left(P_{i,k} - P_{i,k}^{I}\right) \tag{2.4b}$$

$$N_{i,k}^{L} + r_{i,k} = N_{i,k}^{V} = N_{i,k} \tag{2.4c}$$

$$y_k^I = f(x_k^I, T_k^I, P) \tag{2.4d}$$

where a is specific interfacial area, k_g and k_l are gas and liquid film apparent mass transfer coefficients, N^V and N^L are transfer rates through the vapor and liquid films, P is total pressure, r is reaction rate, V is volume, and superscript I refers to the gas/liquid interface. These equations assume that the gas/liquid interface: (1) has no accumulation (Equation 2.4c) and (2) is at equilibrium (Equation 2.4d). In the most general case, the mass transfer coefficients are a function of the apparent diffusion coefficient, temperature, fluid velocity, and packing geometry. In the low-order model, the mass transfer coefficients are treated as constant, adjustable parameters.

Interphase energy transfer occurs as a result of two phenomena: enthalpy transfer from interphase material flux and natural convection due to a temperature gradient. Because the thermal conductivity of the liquid is much greater than that of the gas, the low-order model assumes that there is no temperature gradient in the liquid film ($T_k^L = T_k^I$). The interphase energy transport (N_H) is determined by Equation 2.5:

$$N_{H,k} = V_k h_k^V a(T_k^V - T_k^L) + N_{T,k}\hat{H}_k^V \tag{2.5}$$

where $\hat{H}$ is specific enthalpy and h is the convective heat transfer coefficient. h is related to the gas mass transfer coefficient for water through the Chilton-Colburn analogy.

2.1.4 Kinetics

Low-temperature CO_2 absorption is further limited by reaction kinetics occurring in the liquid film, which can be explicitly modeled using the Arrhenius equation for calculating reaction rate or implicitly modeled as an enhancement to the apparent mass-transfer

coefficient. The parameter k_g' has been defined (Dugas and Rochelle, 2011) to account for the enhancement due to chemical reaction of the apparent CO_2 liquid film mass transfer coefficient. This parameter is measurable experimentally, unlike a true enhancement factor, and is mostly a function of CO_2 loading.

The entire resistance to mass transfer across the two-film boundary (K_g) is calculated using a series resistance model (Equation 2.6a), and the total interphase flux is determined based on a partial pressure driving force between the bulk gas and bulk liquid (Equation 2.6b):

$$\frac{1}{K_g} = \frac{1}{k_g} + \frac{1}{k_g'} \tag{2.6a}$$

$$N_i = V K_{g,i} a (P_i - P_i^*) \tag{2.6b}$$

where P_i is partial pressure of the bulk vapor. Figure 2.2 summarizes the physical and chemical resistances occurring in the boundary layer.

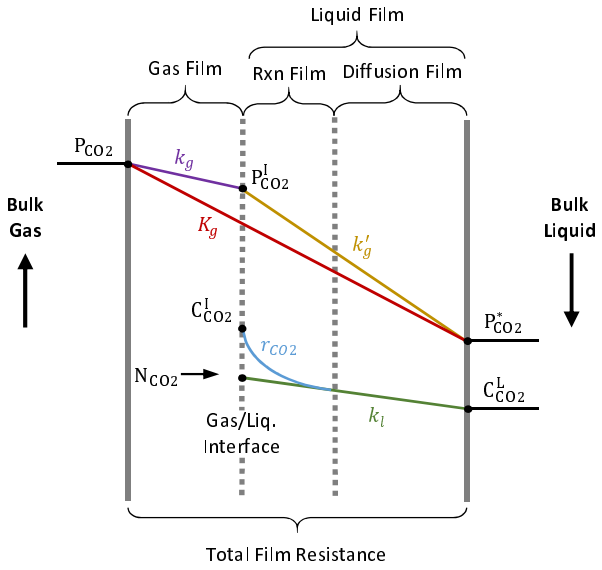

Figure 2.2: In the gas film, there is physical resistance to mass transfer (k_g). The liquid film has both physical resistance (k_l) and a rate-limited chemical reaction (r). The liquid resistances are lumped into the parameter k'_g. The total two-film resistance is lumped into the parameter K_g.

2.1.5 Contactor and Exchanger Characteristics

The type of packing used in the absorber and stripper affects mass and heat transfer coefficients as well as hydraulic properties. Similarly, heat exchanger design is important for calculating the overall heat transfer coefficient and hydraulics. In general, the transfer coefficients, liquid hold-up, and pressure drop are functions of geometry and fluid velocity.

2.1.6 Summary of Model Complexity

Table 2.1 assigns the model parameters discussed in the preceding sections into high-, medium-, and low-order models. The groupings attempt to pair model properties that have approximately equivalent levels of complexity.

Table 2.1: Overview of model complexity

	High-Order	Medium-Order	Low-Order
Flow Type	Distributed (plug flow)	Distributed (plug flow)	Lumped (well-mixed)
Thermo	Activity-Based (true species)	Activity-Based (true species)	Semi-Empirical (apparent species)
Transport	Rate-Based (Maxwell-Stefan)	Rate-Based (variable apparent k_g and k_l)	Rate-Based (constant apparent K_g)
Kinetics	Reactions in Discretized Liquid Film	Embedded in Variable Apparent k'_g	Embedded in Constant Apparent K_g
Contactor Characteristics	Variable Hydraulics (geometry and velocity dependent)	Variable Hydraulics (geometry and velocity dependent)	Constant Hydraulics (fixed at design point)

Table 2.2 summarizes the characteristics of previously published plantwide dynamic models. Based on these characteristics, an overall level of model order is assigned according to the guidelines in Table 2.1. Low- and medium-order models are developed in this work (Chapters 3 and 7, respectively) and are included in the table.

Table 2.2: Previously published equation-based plantwide dynamic models

	Model Type	Thermo	Transport	Kinetics	Overall Order
Ziaii-Fashami (2012)	Lumped	Semi-Empirical	Rate-Based	Embedded in k'_g	Medium
Enaasen-Flø et al. (2015)	Distributed	Semi-Empirical	Rate-Based	Enhancement Factor	Medium
Nittaya et al. (2014)	Distributed	Semi-Empirical	Rate-Based	Enhancement Factor	Medium
Lawal et al. (2012)	Distributed	e-NRTL	Rate-Based	Instantaneous Reaction	Low
Ceccarelli et al. (2014)	Distributed	gSAFT	Rate-Based	Instantaneous Reaction	Low
This Work Medium-Order	Distributed	e-NRTL	Rate-Based	Embedded in k'_g	Medium
This Work Low-Order	Lumped	Semi-Empirical	Rate-Based	Embedded in K_g	Low

Table 2.2 shows that there are currently no published high-order plantwide dynamic models, which include rate-based mass transfer with explicit reactions occurring in the liquid film. The discretized film reactions cause high-order models to be difficult to initialize and not robust in off-design conditions, making them unsuitable for dynamic simulation of disturbances and set point changes.

2.2 Control Strategies for Integrated Amine Scrubbing Plants

Previously published plantwide process control strategies have focused on controlling the system from the perspective of the capture plant. Panahi and Skogestad (2011; 2012) selected self-optimizing controlled variables (CVs) for a simple absorber and reboiled stripper process with MEA capturing CO_2 from a coal-fired power plant. After satisfying level control requirements and process constraints, two degrees of freedom (DOFs) remained for the process. The two best self-optimizing CVs were identified as the CO_2 removal in the absorber (Rem) and the temperature of a tray within the stripper column (T_{ST}). Stripper pressure (P_{ST}) was considered an equality constraint and was controlled using the CO_2 delivery rate from the stripper (F_{CO2}). When flue gas rates deviated up to +20%, the solvent circulation rate (F_s) and the reboiler duty (Q_{RB}) were manipulated using PI controllers to control Rem and T_{ST}, respectively. Model predictive control was also considered using the same CVs and manipulated variables (MVs) as the self-optimizing PI control scheme, and marginal improvements were found in the economic performance.

Ziaii-Fashami (2012) designed a multiloop PI control strategy for the same simple absorber and reboiled stripper system with MEA to handle a reduction in coal-fired power plant load, a change in the desired steam extraction rate, and an increase in liquid hold-up from foaming in the absorber. Three DOFs were found after level control requirements were satisfied, which is one more than Panahi and Skogestad considered because P_{ST} was not an equality constraint. Several different control structures were evaluated, and it was concluded that the most stable structure resulted from controlling P_{ST}, reboiler temperature (T_{RB}), and F_s. The set points for these CVs were adjusted using a feedforward scheme where the desired values for a given set of conditions were predetermined from an offline

optimization. With this strategy, there is no guarantee that an optimum will be achieved or process constraints will be obeyed in the case of plant-model mismatch or unmeasured disturbances. Attempting to explicitly control Rem by manipulating F_s was shown to result in oscillations of process variables and was deemed to not be a stable configuration. This work included a steady state model of the power plant steam turbines to predict off-design steam conditions in the stripper reboiler.

Lawal et al. (2010) also considered the same basic process, with disturbances in flue gas load, Q_{RB}, and CO_2 in the flue gas. When operating at normal power plant load, Q_{RB} and F_s were manipulated to control T_{RB} and Rem, respectively. A perfect back-pressure regulator was included at the top of the stripper to maintain P_{ST} at a constant value. This valve will incur a pressure drop penalty and increase the work required by the multi-stage compressor. In the case of an increase in flue gas rate, the Rem controller was turned off and F_s is either kept constant or used to control the liquid to gas (L/G) ratio in the absorber to a constant value. Constant F_s resulted in a lower value for Rem with better energy performance, while constant L/G ratio kept Rem approximately constant with a slight decrease in energy performance. In the case of a reduction in Q_{RB}, both the T_{RB} and Rem controllers were turned off. Keeping F_s and P_{ST} constant with a drop in Q_{RB} will result in poor energy performance from the resulting drop in T_{RB}, and is therefore considered to be an unrealistic control strategy.

The simple absorber and reboiled stripper configuration was again used by Nittaya et al. (2014) with a range of disturbances in the coal-fired power plant, as well as a set point change to Rem. P_{ST} was set to a constant value with no explanation of how this could be practically implemented, although it could possibly occur by using a back-pressure valve

as proposed by Lawal et al. (2010). In a control structure developed using RGA analysis, F_s and Q_{RB} were used to control T_{RB} and Rem, respectively. The reverse pairing was also considered and found to have superior performance to the structure that resulted from the RGA analysis.

Ceccarelli et al. (2014) investigated capture from an NGCC plant using a simple absorber and reboiled stripper with MEA. The simulation was configured to control P_{ST} using F_{CO2} in response to a 30% drop in flue gas rate to the absorber. The ratios of F_s and F_{steam} to the flue gas load were controlled at constant values during the disturbance. While the Rem value is maintained close to its operating target of 85% throughout the disturbance, the plant takes over three hours to reach a new steady state. The authors suggest that feedforward or advanced process control is necessary to improve the response time of the system.

Table 2.3 summarizes the PID feedback control strategies used in the previously published works discussed in this section. There are several works that used non-rigorous models to develop amine scrubbing control strategies (for example, Lin et al. (2011)) or considered just one part of the process (for example, Åkesson et al. (2012)). However, only plantwide models using rate-based mass transfer have been reviewed here.

Table 2.3: Summary of previously published process control strategies for post-combustion amine scrubbing

	MVs	CVs
Panahi & Skogestad (2011; 2012)	F_{CO2}, Q_{RB}, F_s	P_{ST}, T_{ST}, Rem
Ziaii-Fashami (2012)	F_{CO2}, F_{steam}, F_s	P_{ST}, T_{RB}, $F_s = f(F_{flue})$
Lawal et al. (2010)	Q_{RB}, F_s	T_{RB}, Rem (or $\frac{F_s}{F_{flue}}$)
Nittaya et al. (2014)	Q_{RB}, F_s	T_{RB}, Rem
Ceccarelli et al. (2014)	F_{CO2}, F_{steam}, F_s	P_{ST}, $\frac{F_{steam}}{F_s}$, $\frac{F_s}{F_{flue}}$

Chapter 3

Low-Order Dynamic Model

3.1 Overview of Low-Order Model

Developing a dynamic model for the amine scrubbing system is necessary to understand the effects of disturbances on process operation and for controller design. A low-order model of an advanced amine scrubbing process using aqueous piperazine (PZ) is formulated in Appendix A, using the guidelines from Chapter 2. The low order model uses a lumped formulation (Equation 2.1b) with a small value for Ns in the packed sections, where Ns is the number of well-mixed stages. The model has an apparent species representation (Figure 2.1) with a semi-empirical VLE equation (Equation 2.2) and constant values for heat capacity and heat of phase change. The low-order model uses a simplified rate-based representation (Figure 2.2) where the total mass transfer coefficient, $K_g a$, and heat transfer coefficient, ha, are both treated as independent adjustable parameters. Negligible bulk convection is assumed in the stripper of the low-order model to avoid solving a highly nonlinear system of equations. Hydraulic properties are assumed to be constant at their design point.

Concentration (C) and absorber pressure (P_{abs}) were assumed to be constant. The values of these constant model parameters are given in Table 3.1. Parameters used to describe the packed sections within the system are given in Table 3.2. Billet (1995) provides

experimental liquid hold-up (ε^L) values for a range of different packings. For structured packings with a specific area of 250 m^2/m^3, ε^L typically ranges from 0.02–0.10 when the packing is at less than 70% flood. As shown in the table, a midpoint value was arbitrarily selected to represent the hold-up in the low-order model.

Table 3.1: Constant Model Parameters

	Value
C^L (kmol/m^3)	43.9
C^V_{abs} (mol/m^3)	38.4
C^V_{strip} (mol/m^3)	284
P_{abs} (bar)	1

Table 3.2: Packed Column Parameters

	Value
$Ns_{abs,top}$	10
$Ns_{abs,btm}$	10
Ns_{strip}	6
Ns_{ww}	4
$\varepsilon^L_{abs,top}$ (m^3/m^3)	0.05
$\varepsilon^L_{abs,btm}$ (m^3/m^3)	0.05
ε^L_{strip} (m^3/m^3)	0.05

Two case studies were considered for model validation: a full-scale commercial plant and the Separations Research Program (SRP) pilot plant at the University of Texas

at Austin. Equipment dimensions for both the full-scale plant and the SRP pilot plant are given in Table 3.3, where D is diameter and L is height.

Table 3.3: Equipment Dimensions

	Full Plant	SRP
$D_{abs}(m)$	18.5	0.43
$D_{flash}(m)$	9.6	0.46
$D_{strip}(m)$	7.1	0.15
$D_{surge}(m)$	12.1	1.37
$L_{abs,top}(m)$	4	3.05
$L_{abs,btm}(m)$	4	3.05
$L_{waterwash}(m)$	0.38	-
$L_{strip}(m)$	2	2
$L_{distributor}(m)$	0.05	

The model was implemented in MATLAB® and solved using ODE15s. A small number of adjustable parameters in the model help account for uncertainties. The intent of this low-order model is to capture the general behavior of the process for screening regulatory control strategies; a high-order model is required for rigorous process design and optimization studies (Frailie, 2014).

3.2 Model Validation

3.2.1 Steady State Off-Design Validation with High-Order Model

The first objective of the low-order model validation activity was to quantify the model performance as the system moves away from its design point. The off-design steady

state solutions of the model should be sufficiently accurate to predict energy performance and general plant behavior. Here we compare the off-design steady state solutions of the low-order model to a rigorous and previously validated high-order model.

3.2.1.1 Case Study

The system was designed to handle flue gas from a 550 MWe coal-fired power plant specified by Case 11 of NETL (2010). The flue gas conditions for the 100% load case are given in Table 3.4. It is assumed that the flue gas was passed through a direct contact cooler before entering the absorber to cool it to 40°C. This model makes no restrictions on the availability of steam extracted from the power cycle for CO_2 regeneration. The flowrate of CO_2 out of the condensate tank is set by a multistage compressor, and it is assumed that the compressor can always achieve the specified flow.

Table 3.4: Inlet flue gas conditions for 100% power plant load

	Value
F	18.8 kmol/s
y_{CO2}	14.78%
y_{N2}	75.42%
y_{O2}	2.66%
y_{H2O}	7.14%

3.2.1.2 High-Order Aspen Plus® Model

A high-order Aspen Plus® model (Frailie, 2014) was previously used to design the process in Figure 1.4 for this case study (Trimeric Corporation, 2015). The high-order

model was simulated for a range of off-design power plant loads to compare to the low-order model. In each off-design case, the following conditions were maintained:

- Constant L/G ratio in the absorber of 4.32 kg/kg;
- 5 molal PZ entering the absorber;
- Constant c_{CX} in the equation $UA = c_{CX} F_{avg}^{0.7}$ for the main cross exchangers, where F_{avg} is the average molar flowrate of the hot and cold sides of the exchanger and c_{CX} is fit for both exchangers to give the correct $LMTD$ at the design point;
- Constant UA for the overhead vapor exchanger;
- No H_2O accumulation or depletion in the system by adjusting the water wash recycle flowrate;
- 90% CO_2 removal by adjusting lean loading into the absorber;
- Constant flash tank temperature by adjusting the heat duty;
- Constant cold and warm bypass ratios of 9% and 35%, respectively;
- Lean loading target for the absorber met by adjusting the flash tank pressure.

The overall mass and heat transfer coefficients in the absorber, water wash, and stripper used in the Aspen Plus® simulation were found by plotting the transfer rate against the driving force predicted by the high-order model for each bed of packing and determining the slope. Figure 3.1 demonstrates this procedure for the absorber top bed of packing. Table 3.5 summarizes the transfer coefficients found for the packed sections within the

system. While there is a good fit for the heat transfer coefficient and the mass transfer coefficient of H_2O, there is clearly uncertainty in the CO_2 mass transfer coefficient. The nonlinear behavior in the CO_2 transfer profile occurred because the temperature bulge from the exothermic absorption of CO_2 affected the reaction kinetics. The maximum liquid temperature of 60.4°C for the absorber top bed of packing was observed at a CO_2 partial pressure driving force of 5.1 kPa, which corresponds to the minimum in the CO_2 transfer rate profile.

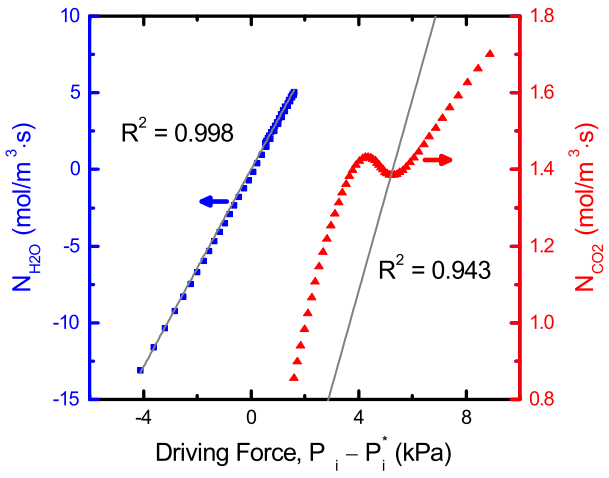

(a) Molar transfer rates

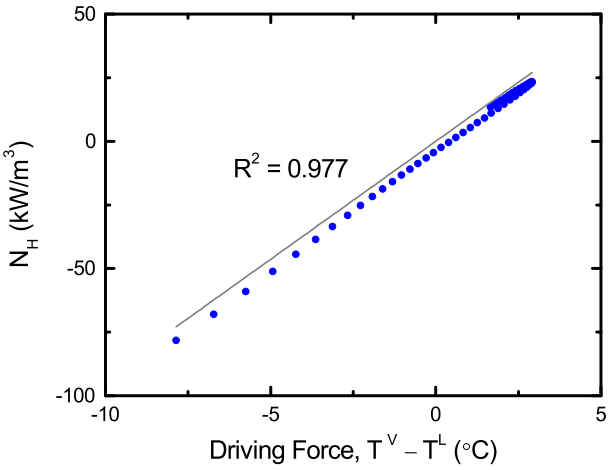

(b) Energy transfer rate

Figure 3.1: Transfer rates versus driving force for the absorber top bed predicted by high-order Aspen Plus® model, using Sulzer 250X packing and a lean loading of 0.22

Table 3.5: Overall mass and heat transfer coefficients for packed beds fitted from Aspen Plus® model

	$K_{g,CO2}a$ (mol/kPa·m^3·s)		$K_{g,H2O}a$ (mol/kPa·m^3·s)		ha (kW/m^3·K)	
	Value	R^2	Value	R^2	Value	R^2
Absorber Top Bed	0.29	0.943	3.2	0.998	9.3	0.977
Absorber Btm Bed	0.11	0.926	2.9	0.972	9.2	0.957
Stripper	0.12	0.871	1.2	0.969	13.0	0.998
Water Wash	-	-	4.2	1.000	7.1	0.999

Heat exchanger overall transfer coefficients (UA) are given in Table 3.6. These coefficients were set by specifying a $LMTD$ of 7.7°C and 7.0°C on the two main exchangers (CX1 and CX2, respectively) and a $LMTD$ of 20°C on the overhead vapor exchanger (CX3).

Table 3.6: Overall heat transfer coefficients specified for design case of Aspen Plus® model

	CX1	CX2	CX3
Design $LMTD$ (°C)	7.7	7.0	20.0
Design UA (MW/K)	77.7	36.2	2.6
Design $\frac{UA}{F_{avg}}$ (J/mol·K)	806	452	401

The non-volatile amine assumption was examined using the high-order model. Figure 3.2 plots the PZ vapor fraction for a range of possible flash tank operating conditions. The vapor fraction was well under 1% for design case, as well as for any off-design condition that might reasonably occur.

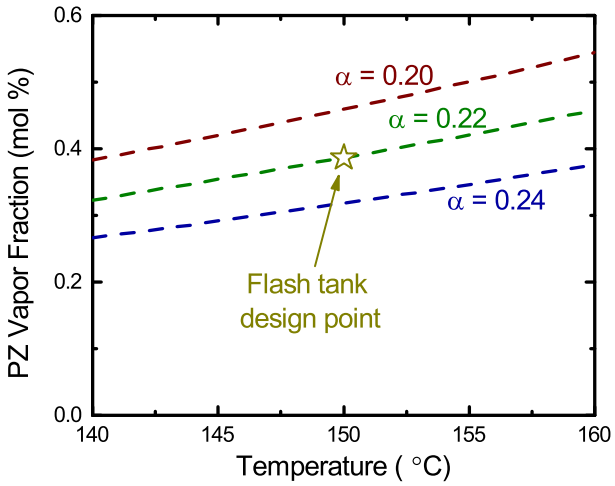

Figure 3.2: Vapor fraction of PZ predicted by high-order model for a range of temperatures and lean loadings (α)

3.2.1.3 Adjusted Parameters

Several parameters were adjusted in the low-order MATLAB® model to match the design conditions from the high-order Aspen Plus® model. The normalized squared error between the low-order model and design case was minimized to adjust the parameters simultaneously in each section of the system (absorber side, stripper side, and entire plant), as summarized in Table 3.7. The table shows that seven physically significant parameters were used to match seven experimentally measurable target values from the design case only; a nonlinear parameter estimation using data from a range of power plant loads was not performed.

Table 3.7: Adjusted parameters in low-order model

	Adjusted Parameter	Target
Absorber	$K_{g,CO2}a$	CO_2 removal
	Cp^V	T^V_{out} flue gas
Stripper	ΔH_{CO2}, ΔH_{H2O}	Flash Tank T & P
	$K_{g,CO2}a$	CO_2 stripping rate
	Cp^V	T^V_{out} stripper gas
Plantwide	Cp^L	$Q_{CX1,hot}$ = $Q_{CX1,cold}$

To match the 90% CO_2 removal rate at design conditions, $K_{g,CO2}a$ was allowed to vary by ± 20%. The ratio of the overall CO_2 mass transfer coefficient for the top and bottom absorber beds was kept constant, according to Equation 3.1:

$$\frac{K_{g,CO2,top}}{K_{g,CO2,btm}} = \left(\frac{K_{g,CO2,top}}{K_{g,CO2,btm}}\right)_{old} \tag{3.1}$$

where the subscript old denotes the value from Table 3.5. The values used in the low-order model are given in Table 3.8.

Table 3.8: CO_2 mass transfer coefficients used in low-order absorber model for validation with high-order model

	$K_{g,CO2}a$ (mol/kPa·m^3·s)
Absorber Top	0.339
Absorber Btm	0.125
Stripper	0.128

The nominal values for ΔH_{CO2} and ΔH_{H2O} were assumed in the absorber. To match the VLE on the stripping side of the process, these values were varied by ± 20%. Cp^L was calculated based on the performance of CX1 and Cp^V was set to match the outlet temperature of the absorber or stripper gas. The thermodynamic parameters are listed in Table 3.9. Figure 3.3 compares the constant solvent thermodynamic parameters of the low-order model to a range of values predicted by the thermodynamically consistent high-order model.

Table 3.9: Thermodynamic parameters used in low-order model for validation with high-order model

	Absorber	Stripper
ΔH_{CO2} (kJ/mol)	70	69.6
ΔH_{H2O} (kJ/mol)	40	34.2
Cp^L (kJ/mol·K)	0.085	
Cp^V (kJ/mol·K)	0.029	0.038

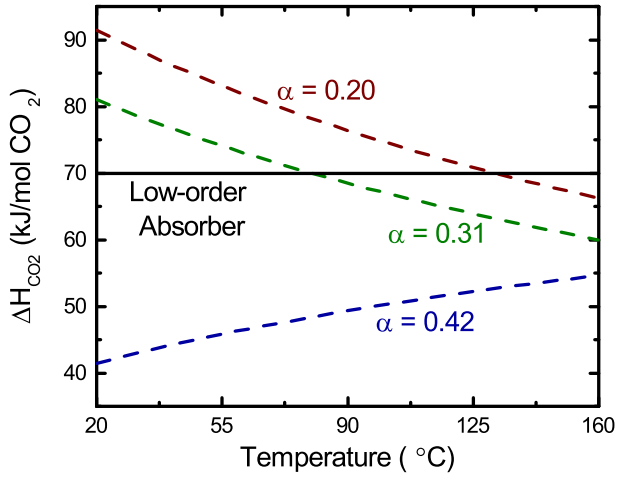

(a)

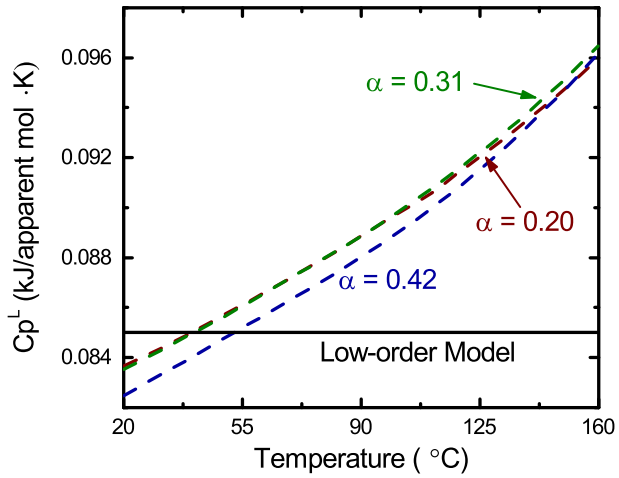

(b)

Figure 3.3: Constant thermodynamic parameters from the low-order model (solid) compared to values predicted by the thermodynamically consistent high-order Aspen Plus® model for a range of temperatures and loadings

3.2.1.4 Results from Boiler Load Reduction

100% to 85% part-load operation of the coal-fired power plant was examined, assuming that the inlet flowrate of flue gas is be directly proportional to load and the flue gas CO_2 concentration is constant. Figure 3.4 gives the inputs to the low-order model based on the results from the high-order model. Figure 3.5 shows that the low-order model is well-behaved near the design load.

3.2.2 Dynamic Validation with Pilot Plant Data

The second objective of the low-order model validation is to show that it captures the general behavior of the process dynamics. In order to have confidence in a control system designed using the low-order model, the model should accurately represent the major time constants present in the system. The dynamic response of the model was compared to pilot plant data to quantify its ability to predict the characteristic time of the total CO_2 inventory in the system.

3.2.2.1 Separations Research Program Pilot Plant

While a growing body of steady-state amine scrubbing pilot plant data is available for model validation, dynamic data are relatively scarce. Enaasen Flø et al. (2015) has previously performed a dynamic model validation that used data from the Gløshaugen pilot plant. SRP at the University of Texas at Austin has an amine scrubbing pilot plant that uses synthetic flue gas equivalent to a 0.1 MWe coal-fired power plant (Chen et al., 2013). The pilot plant is configured similar to Figure 1.4 but does not contain a water wash section of the absorber or a compressor. The amine solvent is nominally 5 molal PZ. In the Spring

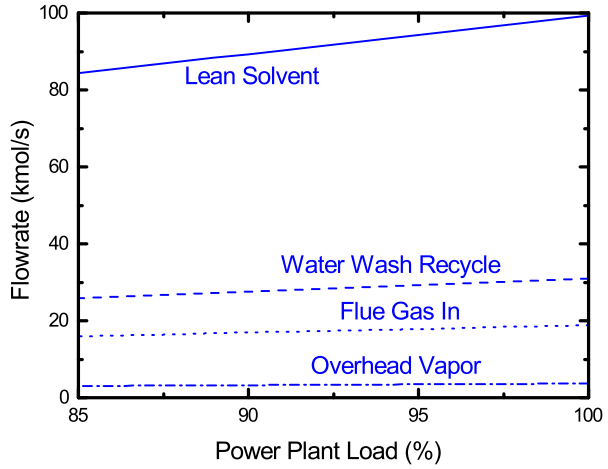

(a)

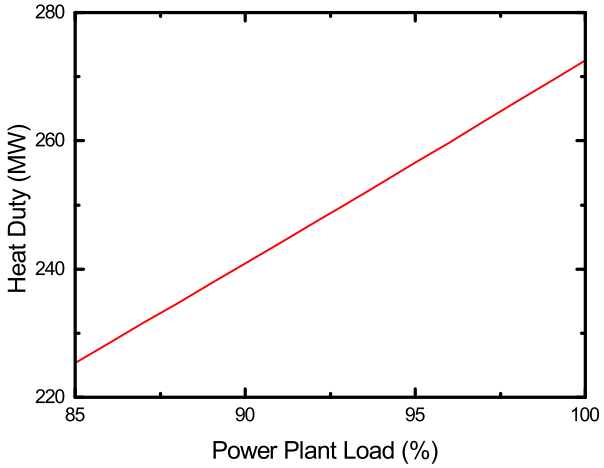

(b)

Figure 3.4: Inputs to low-order MATLAB® model calculated from high-order Aspen Plus® simulation

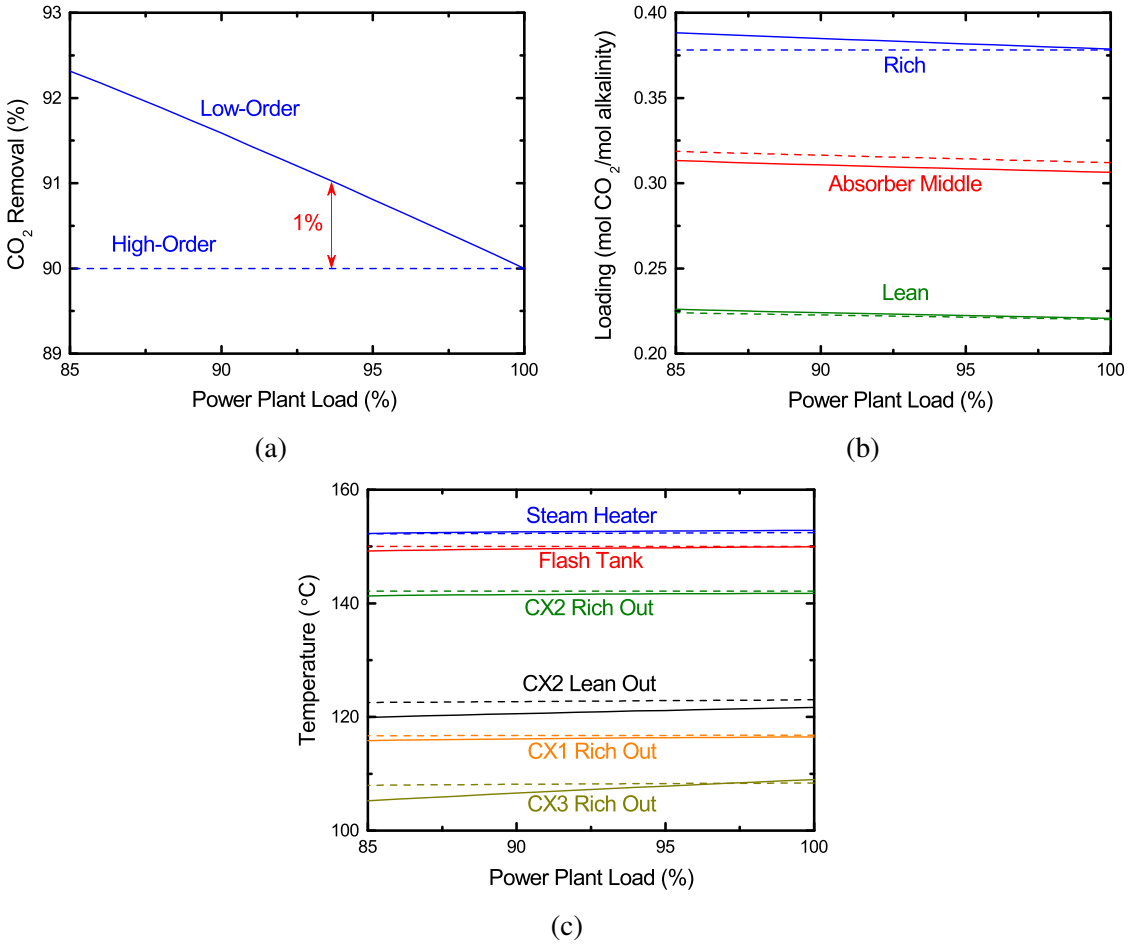

Figure 3.5: Validation of low-order MATLAB® model with high-order Aspen Plus® model

2015 SRP campaign, dynamic step tests were completed to acquire meaningful data which can be easily interpreted and used to validate a dynamic model.

An experiment was performed to test the dynamics of the total CO_2 inventory of the system. When the desired steady state was reached, the stripper pressure control valve in Figure 3.6 was switched from automatic to manual. A step change was made in the valve position, which effectively changed the flowrate of stripped CO_2 out of the process. An increase in valve position, corresponding to a decrease in stripper pressure, was selected for safety considerations to ensure the pressure ratings on the process equipment would not be exceeded. A relatively modest increase in valve position was made to avoid flooding the stripper or loosing control of the level in the flash tank. When the step change occurred, the stripper pressure immediately decreased, CO_2 was flashed out of the solvent at a faster rate, and the temperature of the flash tank decreased. Due to the non-aggressive tuning of the temperature controller on the flash tank, there was a slow ramp up in heat duty after the step change as the controller attempts to maintain the temperature set point. As the system began to approach steady state, the heat duty ramped back down.

Figure 3.7 shows the inputs to the dynamic model to simulate the step change. The heat duty reported in Figure 3.7 is a filtered signal, so the noise has been eliminated. It is assumed the inlet conditions to the absorber, all controlled levels, and all controlled flows remained constant during the dynamic test. The values of the constant inputs to the low-order model can be found in Table 3.10.

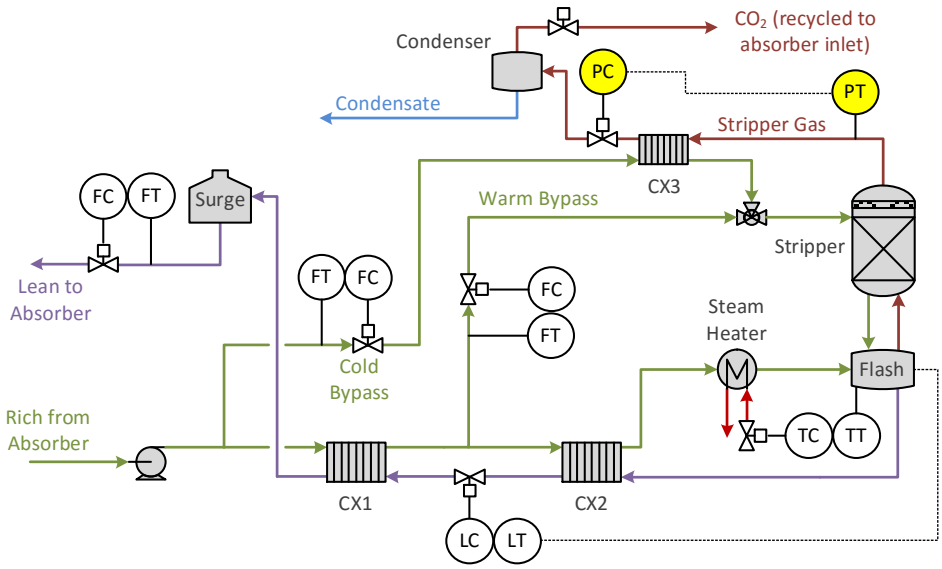

Figure 3.6: SRP pilot plant control system

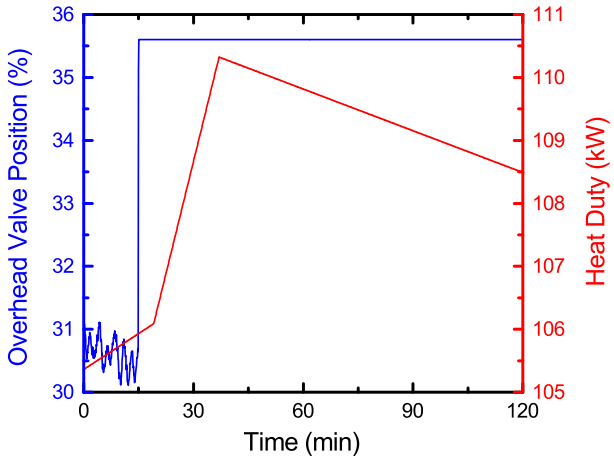

Figure 3.7: Inputs to model

Table 3.10: Constant inputs to low-order model

	Value
$C_{PZ,lean}$	$4.86\ \frac{mol}{kg\,H_2O}$
F_{lean}	$28.8\ \frac{mol}{s}$
F_{flue}	$6.89\ \frac{mol}{s}$
y_{CO2}	12.0%
y_{N2}	69.0%
y_{O2}	18.3%
y_{H2O}	0.7%
$Cold\,BP$	4.6%
$Warm\,BP$	22.4%
T^V	$9.1°C$
Q_{loss}	$46\,kW$

The pressure control valve is an equal percentage valve, and it is operating at choked conditions as a result of the downstream condenser being at approximately atmospheric pressure. The flowrate through the valve can therefore be modeled according to Equation 3.2, which contains constants that have been fitted to the pilot plant data:

$$F_{CO2}\,[kg/s] = (9.66 \times 10^{-5})(29.51)^{q_v - 1}(P\,[Pa])\sqrt{\rho^V\,[kg/m^3]} \tag{3.2}$$

where q_v is the stem position of the valve (between 0 and 1) and ρ^V is the gas density at the valve inlet. Equation 3.2 assumes that condensed water that is in the two-phase flow leaving the hot side of CX3 has no effect on the CO_2 flowrate through the pressure control

valve. Equation 3.2 predicts the measured CO_2 flowrate within 5% for 20 out of 21 steady state runs with varying conditions (Figure 3.8).

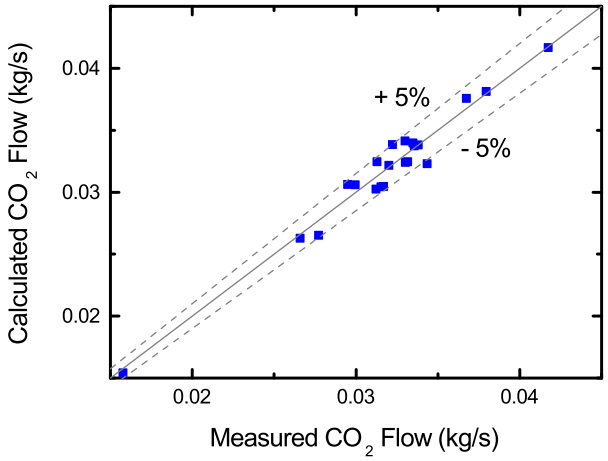

Figure 3.8: Stripper overhead CO_2 flowrate parity plot for stripper gas conditions of 4–7 bar and 8–18°C

Several model parameters were adjusted to match the pilot plant data at steady state before the step change occurs. To achieve the desired removal and stripping rates, the CO_2 mass transfer coefficients were adjusted (Table 3.11). The change from the high-order values from the absorber are in good agreement with a previous pilot plant data reconciliation using the high-order Aspen Plus® model, where the interfacial area in the absorber was adjusted by a factor of 0.74 (Chen et al., 2013). UA values were also calculated for pilot plant conditions and are given in Table 3.12. All of the thermodynamic values from high-order model validation remained the same for the pilot plant validation.

Table 3.11: Fitted $K_{g,CO2}a$ (mol/kPa·m^3·s) for packed sections

	Fit from high-order	Fit from SRP	$\frac{K_{g,CO2}a\ SRP}{K_{g,CO2}a\ High\ Order}$
Top Bed	0.339	0.253	0.744
Bottom Bed	0.125	0.094	
Stripper	0.128	0.128	1.00

Table 3.12: Overall heat transfer coefficients for exchangers fitted from SRP data

	CX1	CX2	CX3
Steady State $LMTD$ (°C)	4.0	3.4	16.8
UA (kW/K)	44	23	0.5
$\frac{UA}{F_{avg}}$ (J/mol·K)	1590	933	441

3.2.2.2 Results from Open-Loop Step Test

After 15 minutes of steady state operation, the stripper overhead valve was placed in manual and a 5% step change increase was made to the position of the valve (Figure 3.7). Density, which is measured online, was used to quantify the changes in lean and rich loadings over time. The Freeman density equation (Freeman, 2011) was used to calculate the density predicted by the low-order model at a given loading. This density was normalized by the density of water at the predicted temperature to remove the temperature dependence on density. The calculated value was compared to the measured value, which was normalized by the density of water at the temperature measured by the densitometer. Figure 3.9 compares the model response with the measured dynamics. The SRP data in Figure 3.9

were sampled at a rate of 5 seconds from the lean stream at a flowrate of 10 gpm and from the cold rich stream at a flowrate of 0.5 gpm.

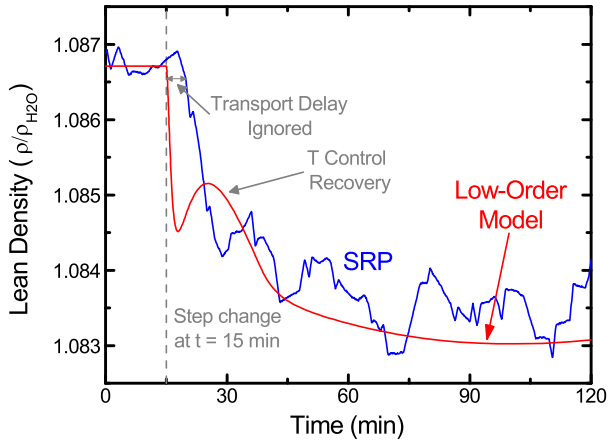

(a) Lean density

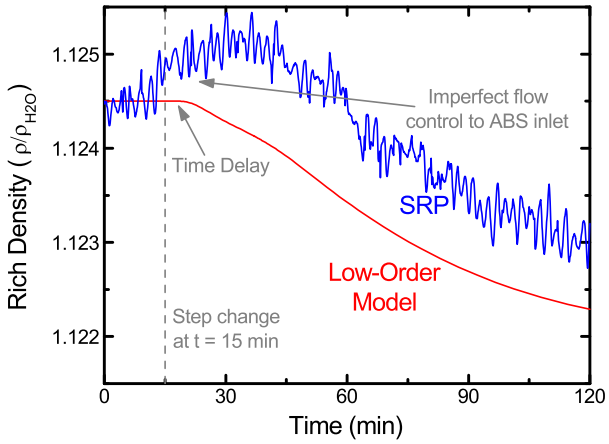

(b) Rich density

Figure 3.9: Dynamic response to a step change in the overhead valve position

Transport delay from piping is ignored in the low-order model, leading to the delay between the predicted and measured lean density response shown in Figure 3.9a. This

delay does not significantly impact the overall response. As previously mentioned, non-aggressive tuning on the flash tank temperature controller caused a slow response in the heat duty supplied to the steam heater. This recovery back to the temperature set point is reflected as an increase in lean density both in the model and experimental data. Figure 3.9b shows that there is an initial small increase in the rich density immediately after the step change is made. This is likely an artificial effect caused by recycling the stripped CO_2 back to the absorber inlet in pilot plant operation. Imperfect flow control of the absorber inlet gas caused an increase in CO_2 concentration; in the true process this will not occur since the inlet flue gas composition is set by the upstream power plant. This change in inlet gas conditions is not captured by the low-order model, causing an offset between the measured and predicted rich density. The shape of the two curves, however, is the same. There is a time delay of approximately 15 minutes in the response of the rich loading in the low-order model, which largely reflects the capacity of the lean surge tank and absorber. The increase in the measured signal begins to level off after 15 minutes, which is consistent with the time delay predicted by the model.

3.3 Discussion

The CO_2 removal rate (Figure 3.5a) is the most important indicator of model performance since maintaining a removal target is likely the primary control objective of the process. The high- and low-order model removal rates agree within 1% when the power plant load is within 6% of the design case. This is sufficient for screening a regulatory control structure where disturbances in a base-loaded power plant are expected to be small. While the lean loading of the low-order model closely tracks the Aspen Plus® simulation,

rich loading is over-predicted as the power plant load decreases (Figure 3.5b). This indicates the absorber performance is being over-predicted, and that the decrease in the overall CO_2 mass transfer coefficient with decreasing fluid velocity is significant. This observation is consistent with the systematically high removal rate prediction. The predicted temperatures (Figure 3.5c) are in good agreement, showing a small number of adjustable thermodynamic parameters are sufficient. The rich side exchanger temperatures for the main cross exchanger with constant UA tracks the temperatures predicted using a UA which depends on fluid flowrate. Therefore it can be concluded that constant UA is a good assumption at part-load when operating near the design case. For all cases, the low-order MATLAB® model converged when given a set of set of initial conditions that were near the steady state solution; the high-order Aspen Plus® model requires multiple initialization steps for convergence.

Processes with material and energy recycle are known to complicate process dynamics and control compared to cascaded units without recycle (Luyben, 1993; Morud and Skogestad, 1996). In the amine scrubbing system, the recycled lean solvent causes positive feedback in the absorber and increases the system time constant. Processes with heavy material recycle have historically included surge tanks to buffer disturbances at the expense of added capital cost and increased total inventory. The SRP pilot plant includes a large lean surge tank prior to the inlet to the absorber. The time constant for the CO_2 removal rate is associated with the total CO_2 inventory, most of which is in the lean surge tank. In the step change experiment, the rich loading time constant is representative of the total inventory. The pilot plant was not allowed to run to steady state after the step change occurred. However, simulating the model to steady-state in Figure 3.10 (by holding the

heat duty at its final value in Figure 3.7) showed that the characteristic time of the CO_2 inventory is 77 minutes. This is much longer than the total liquid residence time of 47.7 minutes (Table 3.13) because of the significant material recycle from the stripper back to the absorber.

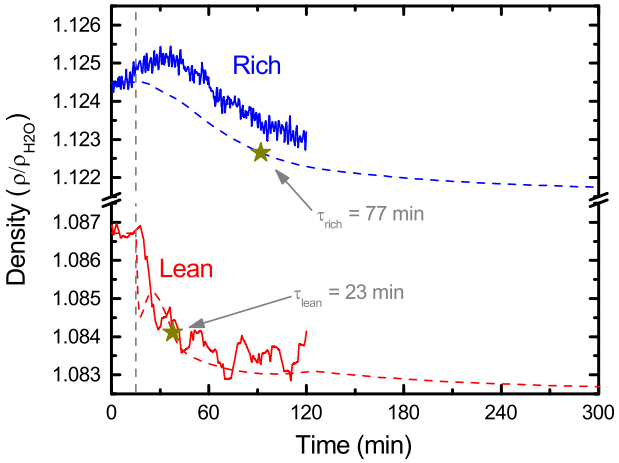

Figure 3.10: Characteristic times of density measurements

Table 3.13: Liquid residence times for SRP unit operations

	Residence Time (min)
Lean Surge Tank	37.5
Absorber Sump	2.7
CX1	2.1
Flash Tank	1.3
Absorber Chimney Tray	1.3
CX2	1.3
Absorber Packing	1.1
Absorber Distributor	0.2
Stripper Packing	0.2
Total	47.7

A commercial post-combustion capture plant will not be designed with a large surge tank because it increases safety risks by maintaining a large inventory of amine, presents operational challenges for solvents operating near their solid solubility limit, and is prohibitively expensive. A sensitivity analysis was performed with the low-order model by varying the hold-up of SRP solvent in the presence of the step change in overhead valve position, shown in Figure 3.11. All other residence times listed in Table 3.13 remained constant. To remove the dynamics associated with the varying heat duty, a step change was also made simultaneously to the steam heater duty to its final value in Figure 3.7. Both a lean surge tank and rich surge tank were considered. In the case of a rich surge tank, which was included as part of the absorber sump inventory for the simulation, the lean surge tank

was given an initial level that corresponds to the original absorber sump inventory from Table 3.13.

The response of rich loading was compared to a first-order transfer function with the same gain and characteristic time, demonstrating that the rich loading displays a first-order response (top row of Figure 3.11). With a lean surge tank, the change in lean loading was buffered by the surge tank before it entered the absorber, causing a relatively slow initial response in CO_2 removal (bottom left of Figure 3.11). There was a fast initial response to CO_2 removal that tracked the lean loading in the case of a rich surge tank, followed by a slow approach to steady state as a result of feedback from the stripping side of the process (bottom right of Figure 3.11). Plotting the characteristic time versus the liquid residence time in Figure 3.12 shows that the slope was constant as the surge tank size was varied. In both lean and rich surge tank cases, the characteristic time was slower than the residence time. However, it was significantly slower in the case of a rich surge tank because there was a much larger inventory of CO_2 compared to the lean case. The slow characteristic time is important because it complicates tightly controlling the removal rate.

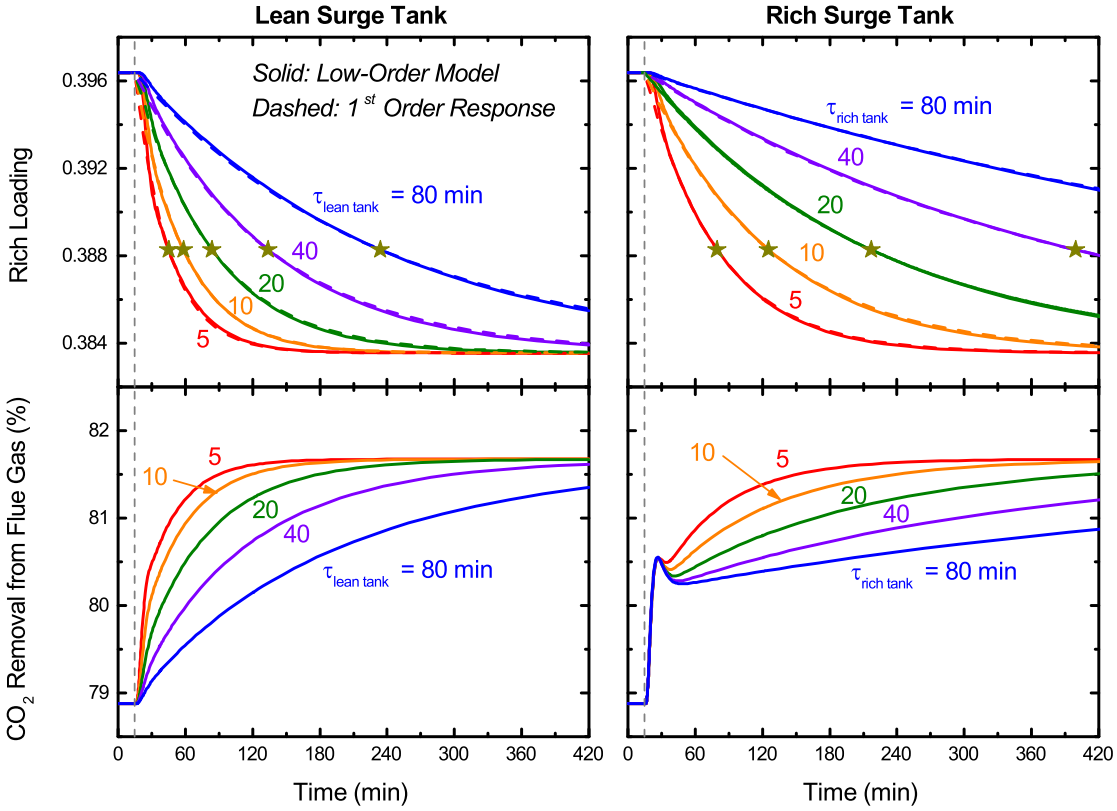

Figure 3.11: SRP surge tank sensitivity analysis showing the response of rich loading and CO_2 removal to a step change in overhead valve position predicted by the low-order model, with stars denoting the characteristic time of the response

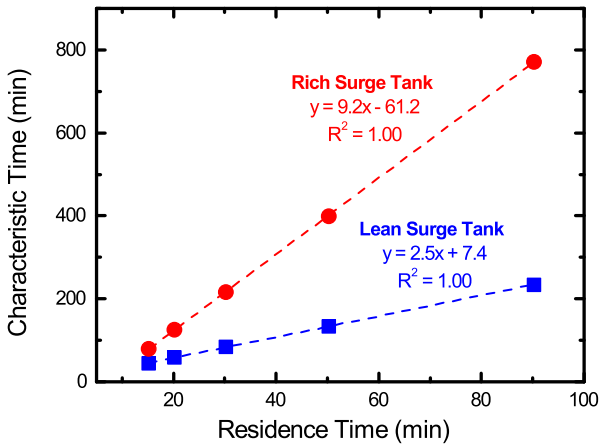

Figure 3.12: Dependence of the characteristic time of the rich loading on the total liquid residence time

3.4 Conclusions

When compared to off-design steady state solutions of a high-order model, the low-order model is in good agreement near the design point. However, the low-order model systematically over-predicts absorber performance as the flue gas load decreases. The low-order model also correctly predicts the dynamic behavior of the overall CO_2 inventory when compared to SRP pilot plant data. Therefore, the low-order model presented here will be used in future work to design a regulatory control layer for the amine scrubbing process. Because of solvent recycle, the characteristic time of the pilot plant rich loading in response to a step change was 60% slower than the total liquid residence time. A sensitivity analysis showed that a lean surge tank causes a slow response in CO_2 removal from the flue gas, while a rich surge tank leads to a faster response in the absorber but a slower approach to steady state.

Chapter 4

Demonstrating Time Scale Multiplicity of Amine Scrubbing

4.1 Introduction

The general trend in the chemical industry is the development of increasingly integrated process designs that use extensive material and energy recycling as well as minimize the overall chemical inventory. With large capital and operating costs, post-combustion amine scrubbing adheres to this trend. After the amine solvent has absorbed CO_2 from the flue gas, it is regenerated at high temperature and completely recycled back to the absorber. Most of the sensible heat from the thermal swing process is recovered either through direct contact packing or a cross heat exchanger. Designing an effective plantwide control strategy of processes with recycle streams is often nonobvious and is much less studied than systems without recycle (Luyben, 1993). An early solution in the process industry to reduce disturbance propagation in recycle systems was to install large surge tanks between interacting process units (Seborg et al., 2011). Large surge tanks are unlikely to be acceptable in amine scrubbing because of the added capital cost, along with oxidation, solid solubility, and safety issues associated with large amine hold-ups. Therefore, any storage tank in the plant will not be able to effectively dampen disturbances that propagate through the recycle streams.

In order to develop a plantwide control strategy for recycle systems with minimal inventory, the multiple time scale behavior that emerges as a result of material and energy recycling must be taken into consideration. There are two distinct time scales that exist in the amine scrubbing process dynamics: a fast time scale at the unit level associated with the large recycle flows and a slow time scale at the process level associated with the small feed and product flows. The time scales of the process variable will be identified using singular perturbation theory. Standard singularly perturbed model form is shown in Equations 4.1–4.2, where $\boldsymbol{\xi}$ represents the slow variables, $\boldsymbol{\eta}$ represents the fast variables, and ε is some small parameter. Arranging the model of the amine scrubbing system in this form allows for the systematic identification of slow and fast variables. In the limit where $\varepsilon \to 0$, the left hand side of Equation 4.2 becomes zero and the fast variables are approximately at steady state (Kokotović et al., 1986).

$$\dot{\boldsymbol{\xi}} = f(\boldsymbol{\xi}, \boldsymbol{\eta}) \tag{4.1}$$

$$\varepsilon\dot{\boldsymbol{\eta}} = g(\boldsymbol{\xi}, \boldsymbol{\eta}) \tag{4.2}$$

4.2 Dynamic Model Description

The model developed in Chapter 3 is used for the process flowsheet shown in Figure 4.1. In contrast to Figure 1.4, the analysis in this chapter models a heated flash tank and does not include a water wash section of the absorber. While a simple absorber with no intercooling is considered in this chapter, the absorber temperature profile is not expected to have a large influence on the system time constants; intercooling is primarily a design choice that reduces the required height of the packing. 8 m PZ was used as the solvent for this analysis. Table 4.1 summarizes the inputs and parameters used for the design case of

the low-order model for the time scale analysis. Figure 4.2 compares the absorber performance of the low-order model at these conditions to a rigorous Aspen Plus® simulation.

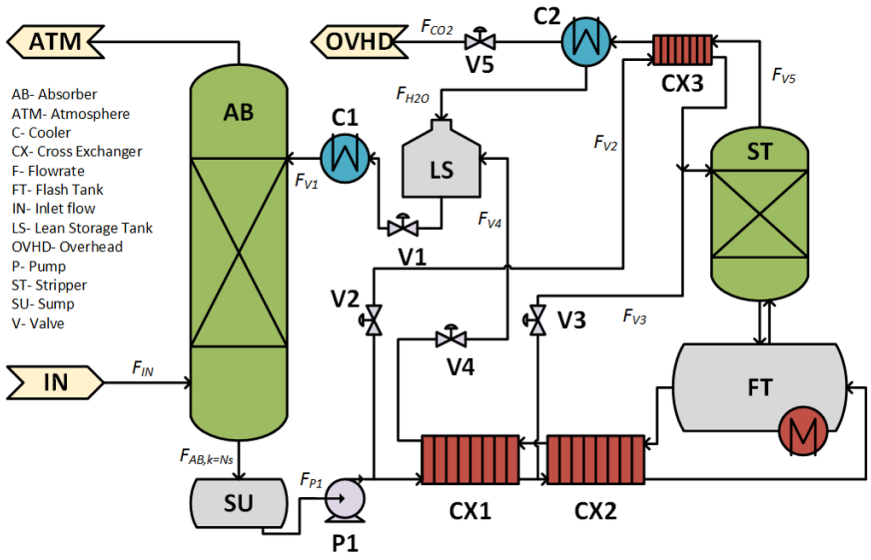

Figure 4.1: Process flow diagram used for the time scale analysis

Table 4.1: Model inputs and parameters for time scale analysis

Inputs	Thermo & Transport Params	Physical Params
F_{V1}^{L} = 139.9 kmol/s	Cp^{L} = 0.11 kJ/mol·K	C^{L} = 35.7 kmol/m^3
F_{V2}^{L} = $0.15F_{V1}^{L}$	Cp^{V} = 0.03 kJ/mol·K	C_{AB}^{V} = 0.038 kmol/m^3
F_{V2}^{L} = $0.20F_{V1}^{L}$	ΔH_{CO2} = 70 kJ/mol	C_{AB}^{V} = 0.350 kmol/m^3
F_{V5}^{L} = 2.9 kmol/s	ΔH_{H2O} = 40 kJ/mol	D_{AB} = 18 m
Q_s = 385 MW	$K_{AB,CO2}a$ = 0.483 mol/kPa·m^3·s	D_{SU} = 18 m
F_{IN} = 18.85 kmol/s	$K_{AB,H2O}a$ = 11.6 mol/kPa·m^3·s	D_{FT} = 10.6 m
T_{IN}^{V} = 313.15 K	$K_{ST,CO2}a$ = 0.966 mol/kPa·m^3·s	D_{ST} = 3 m
$y_{CO2,IN}$ = 0.147	$K_{ST,H2O}a$ = 11.6 mol/kPa·m^3·s	D_{LS} = 10 m
$y_{N2,IN}$ = 0.752	ha_{AB} = 9.3 kW/m^3·K	h_{AB} = 0.05 m
$y_{O2,IN}$ = 0.027	ha_{ST} = 13.0 kW/m^3·K	h_{ST} = 0.05 m
$y_{H2O,IN}$ = 0.074	UA_{CX1} = 600 MW/K	L_{AB} = 4.72 m
$l_{SU,sp}^{L}$ = 3 m	UA_{CX2} = 300 MW/K	L_{ST} = 2 m
$l_{FT,sp}^{L}$ = 3 m	UA_{CX3} = 4.5 MW/K	Ns_{AB} = 10
		Ns_{ST} = 4
		P_{AB} = 1 bar

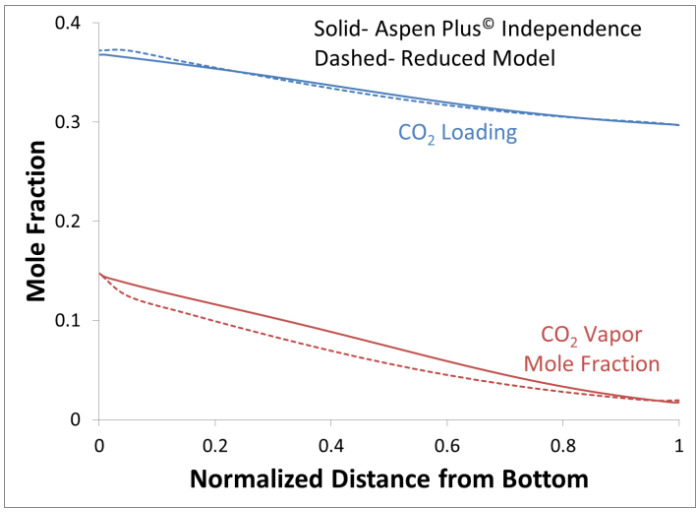

(a)

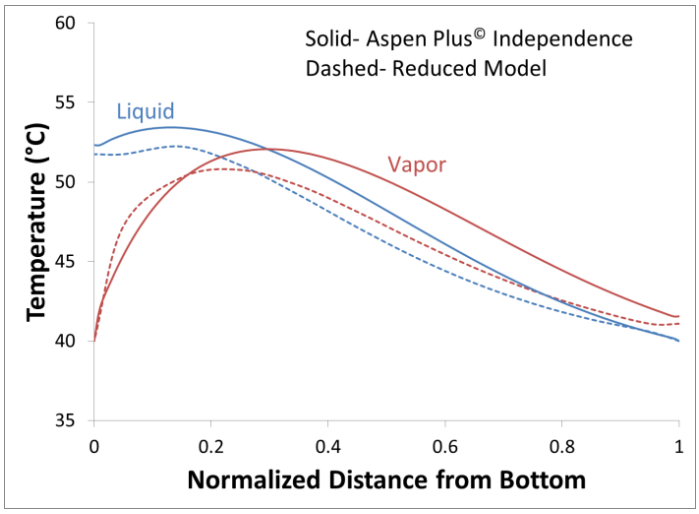

(b)

Figure 4.2: Comparison of absorber (a) mole fraction and (b) temperature profiles for rigorous Aspen Plus® model and low-order model

4.3 Time Scale Analysis

4.3.1 Material Recycle Number

A time scale analysis was performed on the low-order model of the amine process (Chapter 3) based on the work of Baldea and Daoutidis (2012). Figure 4.3 shows a rate-based absorber where CO_2 is transferring into the solvent from the flue gas at all k segments. The recycle flowrate, ${F_{V1}}^s$, is much greater than the amount of CO_2 fluxing into the system. Furthermore, the flowrate of CO_2 in the lean solvent entering the absorber is higher than the flowrate of CO_2 in the flue gas. A material recycle number, Rc, is defined in Equation 4.3 as the ratio of the large recycle flowrate to the small feed flowrate:

$$Rc = \frac{1}{\varepsilon} = \frac{{F_{V1}}^s}{{N^L_{CO2,k=Ns}}^s} \tag{4.3}$$

where superscript s refers to a steady state value. The CO_2 flux is generally expected to be greatest at the bottom of the column, so the flux at the bottom segment is selected for the recycle number definition. An important implication of this selection is that the transfer rates at other segments of the column are of the same order of magnitude or less. The recycle number is substituted into the low-order model described in Chapter 3. Other dimensionless quantities have been defined in Table 4.2.

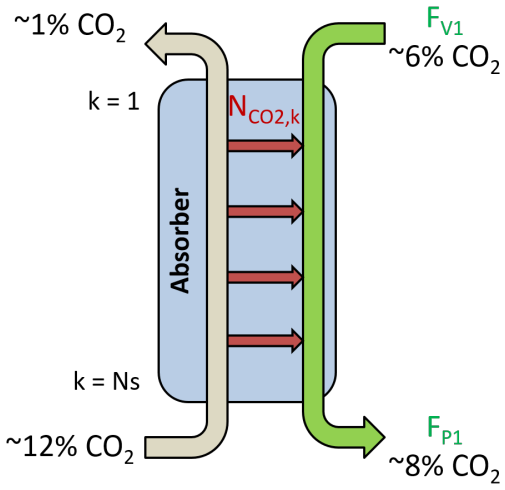

Figure 4.3: CO_2 transfers from the flue gas to the liquid at each k segment of the column, but this flow is relatively small compared to the total liquid flow into the column

Table 4.2: Scaled quantites substituted into low-order model

Manipulated Inputs	Other Parameters
$u_1 = \frac{F_{V1}^L}{F_{V1}^{L\ s}}$	$\omega_2 = \frac{F_{V2}^L}{F_{V1}^{L\ s}}$
$u_2 = \frac{F_{V2}^L}{F_{V2}^{L\ s}}$	$\omega_3 = \frac{F_{V3}^L}{F_{V1}^{L\ s}}$
$u_3 = \frac{F_{V3}^L}{F_{V3}^{L\ s}}$	$\omega_4 = \frac{F_{V4}^L}{F_{V1}^{L\ s}}$
$u_4 = \frac{F_{V4}^L}{F_{V4}^{L\ s}}$	$\omega_{AB,CO2,k} = \frac{N_{AB,CO2,k}{}^s}{N_{AB,CO2,k=Ns}{}^s}$
$u_5 = \frac{F_{V5}^V}{F_{V5}^{V\ s}}$	$\omega_{AB,i,k} = \frac{N_{AB,i,k}}{N_{AB,i,k}{}^s}$
$u_p = \frac{F_{P1}^L}{F_{P1}^{L\ s}}$	

4.3.2 Nonstandard Singularly Perturbed Model

After making the substitutions from Section 4.3.1, the model takes the form of Equation 4.4:

$$\dot{\boldsymbol{x}} = \boldsymbol{f}(\boldsymbol{x}) + \boldsymbol{G}_{sm}(\boldsymbol{x})\boldsymbol{u}_{sm} + \frac{1}{\varepsilon}\boldsymbol{G}_{lg}(\boldsymbol{x})\boldsymbol{u}_{lg} \tag{4.4}$$

where $\boldsymbol{x} \in \Re^n$ is the state vector, $\boldsymbol{u}_{sm} \in \Re^{m_{sm}}$ are the small inlet or outlet flows, $\boldsymbol{u}_{lg} \in \Re^{m_{lg}}$ are the large internal flows, $\boldsymbol{f} \in \Re^n$ is a vector of small flows which are a functions of the states, and $\boldsymbol{G}_{sm}$ and $\boldsymbol{G}_{lg}$ are matrices of appropriate dimensions. Equation 4.4 is referred to as nonstandard singularly perturbed form. Unlike the standard form given in Equations 4.1–4.2, the variables are not explicitly separated into slow and fast time scales in the nonstandard form. Equations 4.5–4.18 show the amine scrubbing low-order model (excluding the energy balances and absorber vapor material balances) in the form of Equation 4.4.

$$\begin{aligned}
\dot{x}_{AB,CO2,k} = \frac{1}{M_{AB}^L}[&N_{AB,CO2,k=Ns}{}^s d_{AB,CO2,k}\omega_{AB,CO2,k} \\
&+ x_{AB,CO2,k-1}\sum_{k=1}^{k-1} N_{AB,k} - x_{AB,CO2,k}\sum_{k=1}^{k} N_{AB,k} \\
&+ \frac{1}{\varepsilon}u_1 N_{AB,CO2,k=Ns}{}^s\left(x_{AB,CO2,k-1} - x_{AB,CO2,k}\right)]
\end{aligned} \tag{4.5}$$

$$\begin{aligned}
\dot{x}_{AB,PZ,k} = \frac{1}{M_{AB}^L}[&x_{AB,PZ,k-1}\sum_{k=1}^{k-1} N_{AB,k} - x_{AB,PZ,k}\sum_{k=1}^{k} N_{AB,k} \\
&+ \frac{1}{\varepsilon}u_1 N_{AB,CO2,k=Ns}{}^s\left(x_{AB,PZ,k-1} - x_{AB,PZ,k}\right)]
\end{aligned} \tag{4.6}$$

$$\begin{aligned}
\dot{x}_{ST,CO2,k} = \frac{1}{M_{ST}^L}[&N_{ST,CO2,k} + x_{ST,CO2,k-1}\sum_{k=1}^{k-1} N_{ST,k} - x_{ST,CO2,k}\sum_{k=1}^{k} N_{ST,k} \\
&+ \frac{1}{\varepsilon}N_{AB,CO2,k=1}{}^s\left(x_{ST,CO2,k-1} - x_{ST,CO2,k}\right)\left(u_2\omega_2 + u_3\omega_3\right)]
\end{aligned} \tag{4.7}$$

$$\dot{x}_{ST,PZ,k} = \frac{1}{M^L_{ST}}[x_{ST,PZ,k-1}\sum_{k=1}^{k-1} N_{ST,k} - x_{ST,PZ,k}\sum_{k=1}^{k} N_{ST,k} + \frac{1}{\varepsilon}{N_{AB,CO2,k=1}}^s\left(x_{ST,PZ,k-1} - x_{ST,PZ,k}\right)\left(u_2\omega_2 + u_3\omega_3\right)] \tag{4.8}$$

$$\dot{y}_{ST,CO2,k} = \frac{1}{M^V_{ST,k}}[\left(y_{ST,CO2,k+1} - y_{ST,CO2,k}\right)\left(u_5{F^V_{V5}}^s + \sum_{k=1}^{k-1} N_{ST,k}\right) + y_{ST,CO2,k+1}N_{ST,k} - N_{ST,CO2,k}] \tag{4.9}$$

$$l^L_{SU} = \frac{4}{\pi {D_{SU}}^2 C^L}\left[\sum_{k=1}^{N_s} N_{AB,k} + \frac{1}{\varepsilon}{N_{AB,CO2,k=Ns}}^s\left(u_1 - \omega_p u_P\right)\right] \tag{4.10}$$

$$\dot{x}_{SU,CO2} = \frac{4}{\pi {D_{SU}}^2 C^L l^L_{SU}}[\sum_{k=1}^{N_s} N_{AB,k}\left(x_{AB,CO2,k=N_s} - x_{SU,CO2}\right) + \frac{1}{\varepsilon}{N_{AB,CO2,k=Ns}}^s u_1\left(x_{AB,CO2,k=N_s} - x_{SU,CO2}\right)] \tag{4.11}$$

$$\dot{x}_{SU,PZ} = \frac{4}{\pi {D_{SU}}^2 C^L l^L_{SU}}[\sum_{k=1}^{N_s} N_{AB,k}\left(x_{AB,PZ,k=N_s} - x_{SU,PZ}\right) + \frac{1}{\varepsilon}{N_{AB,CO2,k=Ns}}^s u_1\left(x_{AB,PZ,k=N_s} - x_{SU,PZ}\right)] \tag{4.12}$$

$$l^L_{FT} = \frac{4}{\pi {D_{FT}}^2 C^L}[-u_5{F^V_{V5}}^s + \frac{1}{\varepsilon}{N_{AB,CO2,k=1}}^s\left(\omega_p u_p - \omega_4 u_4\right)] \tag{4.13}$$

$$\dot{x}_{FT,CO2} = \frac{4}{\pi {D_{FT}}^2 C^L l^L_{FT}}[\left(x_{ST,CO2,k=Ns} - y_{FT,CO2}\right)\sum_{k=1}^{N_s} N_{ST,k} + \left(x_{FT,CO2} - y_{FT,CO2}\right)u_5{F^V_{V5}}^s + \frac{1}{\varepsilon}{N_{AB,CO2,k=1}}^s(\left(x_{SU,CO2} - x_{FT,CO2}\right)u_p\omega_p + \left(x_{ST,CO2,k=Ns} - x_{SU,CO2}\right)\left(u_2\omega_2 + u_3\omega_3\right))] \tag{4.14}$$

$$\dot{x}_{FT,PZ} = \frac{4}{\pi {D_{FT}}^2 C^L l^L_{FT}}[x_{ST,PZ,k=Ns}\sum_{k=1}^{N_s} N_{ST,k} + x_{FT,PZ}u_5{F^V_{V5}}^s + \frac{1}{\varepsilon}{N_{AB,CO2,k=1}}^s(\left(x_{SU,PZ} - x_{FT,PZ}\right)u_p\omega_p + \left(x_{ST,PZ,k=Ns} - x_{SU,PZ}\right)\left(u_2\omega_2 + u_3\omega_3\right))] \tag{4.15}$$

$$\dot{l}^L_{LS} = \frac{4}{\pi {D_{LS}}^2 C^L}[F^L_{H2O} + \frac{1}{\varepsilon}{N_{AB,CO2,k=1}}^s\left(\omega_4 u_4 - u_1\right)] \tag{4.16}$$

$$\dot{x}_{LS,CO2} = \frac{4}{\pi {D_{LS}}^2 C^L l_{LS}^L}\left[-x_{LS,CO2} F_{H2O}^L + \frac{1}{\varepsilon} {N_{AB,CO2,k=1}}^s \omega_4 u_4 \left(x_{FT,CO2} - x_{LS,CO2}\right)\right] \tag{4.17}$$

$$\dot{x}_{LS,PZ} = \frac{4}{\pi {D_{LS}}^2 C^L l_{LS}^L}\left[-x_{LS,PZ} F_{H2O}^L + \frac{1}{\varepsilon} {N_{AB,CO2,k=1}}^s \omega_4 u_4 \left(x_{FT,PZ} - x_{LS,PZ}\right)\right] \tag{4.18}$$

In the context of Equation 4.4, $\boldsymbol{u}_{sm} = u_5$ and $\boldsymbol{u}_{lg} = \left[u_1\, u_2\, u_3\, u_4\, u_p\right]^T$. The only states that are exclusively slow ($\boldsymbol{G}_{lg} = 0$) are the stripper vapor mole fractions in Equation 4.9. All other state variables have both slow and fast components. Figure 4.4 demonstrates the pseudo-open loop response of the process to a 10% step reduction in flue gas rate after one hour of steady state operation. The total material balances (Equations 4.10, 4.13, and 4.16) render the system open loop unstable, so perfect level control is assumed in the sump and flash tank during the simulation. It is also assumed that the water makeup rate is perfectly controlled so the lean storage tank concentration is always 8 m PZ. The absorber liquid mole fractions (Figure 4.4a) have an initial fast response at the unit level as the amount of CO_2 entering the system is decreased. The fast response is followed by a slow transient period as the system approaches a new steady state. The stripper vapor mole fractions (Figure 4.4b) are only affected by the small outlet flowrate and therefore only demonstrate a slow response to the step change.

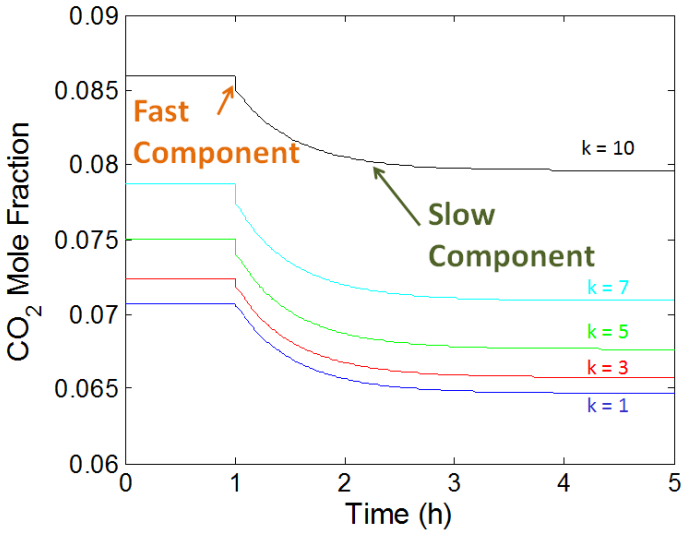

(a)

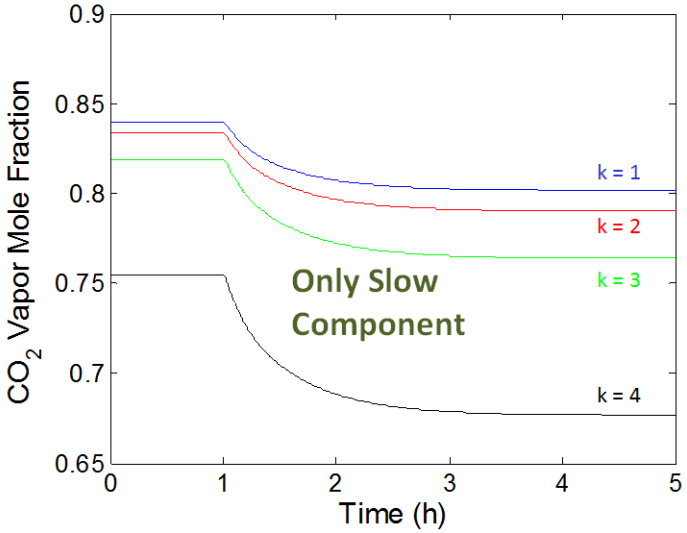

(b)

Figure 4.4: Pseudo-open loop response to a 10% decrease in flue gas flow after one hour for (a) the absorber liquid mole fractions and (b) the stripper vapor mole fractions at segment k of the column

4.3.3 Standard Singularly Perturbed Model

In this section, the process model is explicitly separated into fast and slow variables (Chen et al., 2012). The sump and flash tank inventories must be stabilized based on the fast time scale, so it is assumed that there is a linear state feedback controller for the tank levels that manipulates the tank effluent flow. It is also assumed that there is a state feedback law for the exiting cross exchange temperatures ($T_{CX1,h}$ and $T_{CX3,h}$) that manipulates the bypass flowrates. The feedback control laws are given in Equations 4.19–4.22, which show that the large flowrates are now a function of the states.

$$u_2 = 1 - K_2^p \left(T_{CX3,h}^L - T_{CX3,h,sp}^L\right) \tag{4.19}$$

$$u_3 = 1 - K_3^p \left(T_{CX3,h}^L - T_{CX3,h,sp}^L\right) \tag{4.20}$$

$$u_4 = 1 - K_4^p \left(l_{FT} - l_{FT,sp}\right) \tag{4.21}$$

$$u_p = 1 - K_p^p \left(l_{SU} - l_{SU,sp}\right) \tag{4.22}$$

It is assumed that the matrix $\boldsymbol{G}_{lg}(\boldsymbol{x})$ can be decomposed according to Equation 4.23:

$$\boldsymbol{G}_{lg}(\boldsymbol{x}) = \boldsymbol{B}(\boldsymbol{x})\,\tilde{\boldsymbol{G}}_{lg}(\boldsymbol{x}) \tag{4.23}$$

where $\boldsymbol{B} \in \mathbb{R}^{n\times(n-3-Ns_{ST})}$ is a full column rank matrix and $\tilde{\boldsymbol{G}}_{lg} \in \mathbb{R}^{(n-3-Ns_{ST})\times m_{lg}}$ is a matrix with linearly independent rows (Baldea and Daoutidis, 2014). The variable transformation $\boldsymbol{T}(\boldsymbol{x})$ in Equation 4.24 is applied to explicitly separate the low-order model into

slow and fast states:

$$\begin{bmatrix} \boldsymbol{\zeta} \\ \boldsymbol{\eta} \end{bmatrix} = \boldsymbol{T}(\boldsymbol{x}) = \begin{bmatrix} M_{total} \\ M_{total,CO2} \\ M_{total,PZ} \\ y_{ST,CO2,k=1} \\ \vdots \\ y_{ST,CO2,k} \\ \vdots \\ y_{ST,CO2,k=Ns} \\ \tilde{\boldsymbol{G}}_{lg}(\boldsymbol{x})\,\boldsymbol{u}_{lg}(\boldsymbol{x}) \end{bmatrix} \tag{4.24}$$

where $\boldsymbol{\zeta} \in \mathbb{R}^{3+Ns_{ST}}$ are the slow states, $\boldsymbol{\eta} \in \mathbb{R}^{n-3-Ns_{ST}}$ are the fast states, and the subscript $total$ denotes the total system molar hold-up. This transformation allows the low-order model to be arranged in the form of Equations 4.1–4.2, and shows that the total molar hold-ups also evolve on the slow time scale in addition to the stripper vapor mole fractions. Figure 4.4 demonstrates the step response of the total system CO_2 hold-up has only a slow component. The steady state liquid residence times in the absorber, sump, flash tank, stripper, and lean storage tank are 0.3, 3.2, 1.1, 0.02, and 0.9 minutes, respectively, while Figure 4.5 shows that the time constant of total CO_2 inventory is ˜32 minutes. The total plant inventory time constant is an order of magnitude higher than the individual unit operation residence times because of the material recycle occurring in the process.

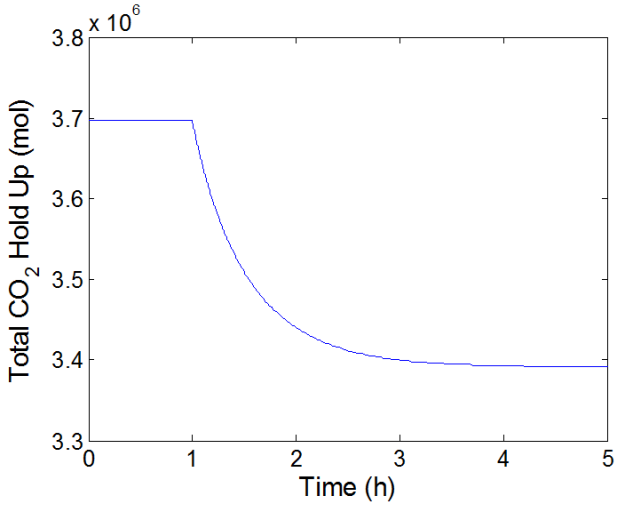

Figure 4.5: Pseudo-open loop response to a 10% decrease in flue gas flow after one hour for the total CO_2 inventory

The low-order model was linearized around the design point to perform an eigenvalue (λ) analysis. Figure 4.6 plots the system λ's, which represent the reciprocals of the process time constants. The figure shows that the real part spans several orders of magnitude. The condition number, defined as $\frac{|\lambda_{max}|}{|\lambda_{min}|}$, is 10^{11}, clearly demonstrating that the process model contains multiple time scales.

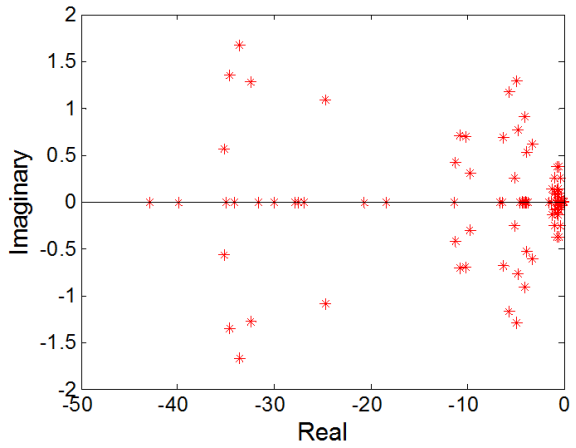

Figure 4.6: Eigenvalues of the linearized system

4.4 Proposed Control Structure

The overall control objective of the amine scrubbing process will likely be related to maintaining a desired CO_2 removal rate that minimizes energy use. Based on the singularly perturbed model form, this control objective is related to the slow time scale. In the previous section, state feedback control laws were proposed for the large internal solvent flows in order to stabilize the system on the fast time scale. The only remaining manipulated variable for the slow time scale objectives is the stripper overhead flowrate (F^V_{V5}). F^V_{V5} is closely tied to the flowrate of CO_2 out of the process, so it should be used to control the removal rate. Previous work has proposed controlling the removal rate with the large internal recycle flow Panahi and Skogestad (2011, 2012); Ziaii-Fashami (2012); Lawal et al. (2010); Nittaya et al. (2014). However, this strategy will likely lead to an ill-conditioned controller based on the time scale analysis since the slow time scale has not been addressed. Oscillations in stripper pressure were observed by Ziaii-Fashami (2012) when the removal

rate was controlled using the solvent flowrate. The control structure proposed in this work is summarized in Table 4.3.

Table 4.3: Proposed Control Structure

Time Scale	Output Variable	Input Variable	Proposed Controller
Fast	Sump Level	Sump Effluent Flowrate	Proportional
	Flash Tank Level	Solvent Recycle Flowrate	Proportional
	Lean Storage Tank Level	–	Uncontrolled
Slow	CO_2 Removal Rate	Stripper Overhead Flowrate	Model-Based

4.5 Conclusions

Two time scales exist in the amine scrubbing process dynamics as a result of material recycling. The time scale decomposition shows that the stripper vapor mole fractions and total system inventories evolve on the slow time scale only. Therefore the CO_2 removal rate should be controlled using the small stripper overhead flow. Controlling CO_2 removal with the large solvent recycle flowrate will likely lead to oscillations in process variables.

4.6 Notation

Greek

ΔH_{CO2} heat of desorption (kJ/mol CO_2)

ΔH_{H2O}	heat of vaporization (kJ/mol H_2O)
$\boldsymbol{\eta}$	vector of fast variables (varies)
ω	$\mathcal{O}(1)$ quantity (varies)
$\boldsymbol{\xi}$	vector of slow variables (varies)

Roman

a	wetted area (m^2/m^3)
C	molar concentration (mol/m^3)
Cp	specific heat capacity (kJ/mol·K)
D	diameter (m)
d	disturbance (–)
F	molar flowrate (mol/s)
h	liquid hold-up in packing (m^3/m^3)
$\hat{H}$	specific enthalpy (kJ/mol)
K	overall mass transfer coefficient ($mol/Pa{\cdot}m^2{\cdot}s$)
K^p	proportional gain (varies)
L	length (m)
l	level (m)
M	molar amount (mol)
N	transfer rate (amount/s)

Ns	number of well-mixed stages (–)
P	pressure (Pa)
P^*	equilibrium pressure of the liquid (Pa)
Q_s	steam heat duty (kW)
Rc	recycle number (–)
T	temperature (K)
u	normalized manipulated input (–)
UA	overall heat transfer coefficient (kW/K)
vf	vapor fraction (mol/mol)
$\boldsymbol{x}$	state vector (varies)
x	liquid apparent mole fraction (mol/mol)
y	vapor mole fraction (mol/mol)

Subscripts

H	enthalpy
i	component (CO_2, PZ, H_2O, N_2, or O_2)
k	stage number (top stage is k = 1)
sp	setpoint

Superscripts

L	liquid

s	steady state
V	vapor

Chapter 5

Regulatory Control

5.1 Introduction

Amine scrubbing is highly integrated with the upstream power plant and downstream enhanced oil recovery (EOR) facility, as shown in Figure 5.1. The power plant consists of a coal-fired boiler and high-, intermediate-, and low-pressure steam turbines (HP, IP, and LP, respectively). Flue gas from the boiler passes through pollution control equipment, including selective catalytic reduction (SCR), electrostatic precipitation (ESP), and flue gas desulfurization (FGD), before it is sent to a direct contact cooler (DCC) to cool the gas to 40 °C. The cooled flue gas enters the bottom of the absorber, where it is countercurrently contacted with amine solvent to remove CO_2. Steam from the IP/LP crossover point of the power cycle is then used to regenerate the solvent in a stripper. The stripped CO_2 is compressed in a multi-stage compressor and injected into a reservoir for EOR, creating a customer demand for the CO_2 product. The power plant, capture plant, and EOR facility can be considered three separate entities with competing operational and economic objectives. The goal of this Chapter is to develop regulatory control strategies using a system-wide approach, taking into account these competing objectives.

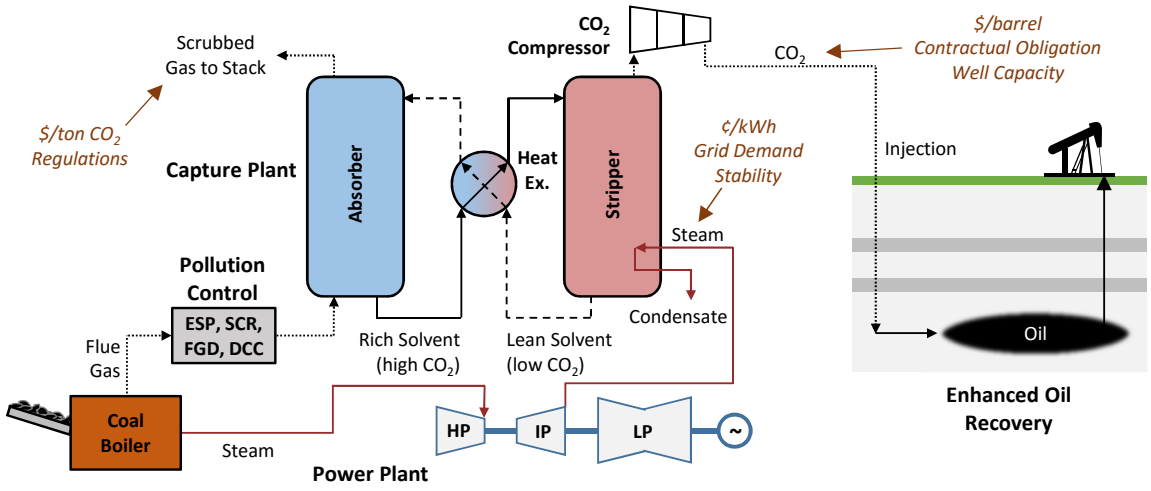

Figure 5.1: The amine scrubbing capture plant is highly integrated with the upstream power plant and downstream EOR facility

5.1.1 Scope

A holistic approach is used to develop regulatory control strategies for a range of system objectives. The control strategies were assessed using a dynamic model of an amine scrubbing process with an optimized flowsheet and an advanced solvent, in contrast to previous works which have generally modeled a simple absorber and reboiled stripper with MEA. An explicit representation of a 550 MWe coal-fired power plant was included to fully capture the dependence of the amine plant operation on power plant conditions. Four mutually exclusive system objectives were addressed: (1) satisfying the CO_2 demand for EOR, (2) satisfying the steam demand for electricity generation, (3) maintaining a CO_2 removal rate target, and (4) minimizing deviations from steady state. The trade-offs associated with the regulatory control strategies necessary to satisfy each of these objectives are described in detail in the subsequent sections. The implications of the various control

strategies for equipment design were explored, including the stripper column, steam extraction valve, and compressor configuration. The significance of the solvent surge tank location on controller performance was also considered.

5.2 Process Model

A dynamic process model was used as a tool to tune PID controllers, test the system response to various disturbances and set point changes, and evaluate the performance of various controller configurations. The process model was designed to capture 90% of CO_2 from the flue gas of a 550 MWe coal-fired power plant operating at 100% load (Trimeric Corporation, 2015). The model was simulated in Simulink® using ODE15s. The following sections describe the components of the model used in this work.

5.2.1 Capture Plant

A control relevant low-order model of an intercooled absorber and advanced flash stripper (AFS) with aqueous piperazine (PZ) solvent was previously developed and validated in Chapter 3. The flowsheet for this process is given in Figure 1.4. The flowsheet shows that both lean and rich surge tanks have been considered as process alternatives. Liquid residence times for the major unit operations are listed in Table 5.1. More detailed information about equipment sizes can be found in Chapter 3. Individual capture plant unit operations were included in the Simulink® flowsheet using S-function implementation.

Table 5.1: Liquid residence times

Unit	Min
Total Absorber	7.2
Sump	5.0
Chimney Tray	2.0
Distributor	0.1
Packing	< 0.1
Flash Tank	5.0
Total Exchangers	3.0
CX1	1.8
CX2	1.0
CX3	< 0.1
Steam Heater	0.2
Surge Tank	2.5
Stripper	< 0.1
Total	17.7

5.2.2 Power Plant

The temperature and pressure of steam at the IP/LP crossover point depend on the boiler load and the flowrate of steam extracted to the steam heater of the AFS. This section develops a steady state coal-fired power plant model based on Case 11 of NETL (2010) to predict the steam conditions for off-design turbine operation. A detailed flowsheet of a supercritical coal-fired power plant is given in Figure 5.2, along with typical operating conditions. It is assumed that the boiler is regulated by an adiabatic throttle valve to produce steam at 24.1 MPa and 593 °C. The steam flowrate through the throttle valve is calculated

according to Equation 5.1, given the boiler load:

$$w_{boiler} = \frac{Q_{boiler}}{\hat{H}^V_{boiler} - \hat{H}^L_{feedwater}} \tag{5.1}$$

where $\hat{H}$ is mass specific enthalpy, Q is duty, w is mass flowrate, subscripts $boiler$ and $feedwater$ refer to conditions of steam exiting the boiler and feedwater entering the boiler, respectively, and superscripts L and V refer to liquid and vapor phases, respectively. $\hat{H}^V_{boiler}$ and $\hat{H}^L_{feedwater}$ are both assumed to be constant for all loads.

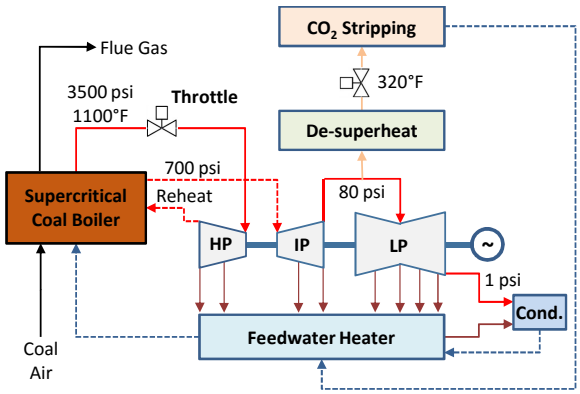

Figure 5.2: Detailed flowsheet of a supercritical coal-fired power plant with steam extraction for CO_2 regeneration

The HP steam from the throttle valve is expanded through n turbine stages, shown in Figure 5.3. Each stage i consists of two uncontrolled steam extractions: (1) steam extracted to the next stage (w_i) and (2) steam extracted to the feedwater heater system (w_{xi}). Other minor steam extractions, for example to the steam seal regulator, have been ignored in this work. Equation 5.2 represents each stage, including a mass balance (Equation 5.2a), a steam table lookup (Equation 5.2b), and Stodola's Ellipse Law for calculating uncontrolled

extractions (Cooke, 1983) (Equations 5.2c–5.2d):

$$w_{i-1} = w_i + w_{xi} \tag{5.2a}$$

$$T_i = f(P_i, S_i) \tag{5.2b}$$

$$P_i = \sqrt{w_i^2 T_i \phi_{Di} + P_{i+1}^2} \tag{5.2c}$$

$$P_i = \sqrt{w_{xi}^2 T_i \phi_{Dxi} + P_{i+1}^2} \tag{5.2d}$$

where S is entropy and ϕ_D is a flow constant calculated from design conditions. Values for ϕ_D, which were set to match the flowrates from the NETL case, are given in Table 5.2.

Table 5.2: Flow constants ($Pa^2 \cdot s^2/K \cdot kg^2$) for uncontrolled extractions to the next turbine stage (ϕ_{Di}) and to the feedwater heater (ϕ_{Dxi})

Turbine	Stage (i)	ϕ_{Di}	ϕ_{Dxi}
HP	1	1.71 X 10^6	4.86 X 10^8
	2	1.98 X 10^5	8.03 X 10^6
IP	3	1.06 X 10^5	1.89 X 10^7
	4	3.82 X 10^5	2.66 X 10^7
LP	5	8.52 X 10^3	4.24 X 10^6
	6	1.55 X 10^3	9.68 X 10^5
	7	295	3.93 X 10^5
	8	44.8	9.51 X 10^4
	9	13.4	–

Isentropic expansion has been assumed at each turbine stage; therefore, $S_i = S_{In}$ in the HP turbine and $S_i = S_{RH}$ after the HP/IP steam has been reheated in the boiler,

according to Equation 5.3.

$$S_{In} = f(P_{i=1}, \hat{H}^V_{boiler}) \tag{5.3a}$$

$$S_{RH} = f(P_{i=RH}, \hat{H}^V_{RH}) \tag{5.3b}$$

$\hat{H}^V_{RH}$ is calculated by assuming the reheating duty (Q_{RH}) is directly proportional to Q_{boiler}.

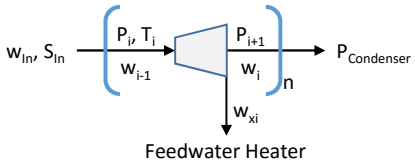

Figure 5.3: Power plant turbine stage showing two uncontrolled extractions

When the power plant steam cycle is integrated with the capture plant, a controlled extraction to the stripper is added at the IP/LP crossover point. This controlled extraction is assumed to occur through an equal percentage valve, according to Equation 5.4:

$$w_{SH} = C_v R^{q_v - 1} \sqrt{(P_{IP/LP} - P_{SH})\rho_{IP/LP}} \tag{5.4}$$

where C_v is the valve coefficient, q_v is the valve stem position, R is a constant (set at a typical value of 50), ρ is mass density, and the subscripts IP/LP and SH refer to conditions at the IP/LP crossover point and the steam heater of the AFS, respectively. P_{SH} was determined by assuming the saturated steam on the shell side of the steam heater is always 5 °C greater than the process fluid. C_v was calculated so that w_{SH} is the design flowrate when $q_v = 1$. In other words, the steam extraction valve is 100% open at design conditions to minimize the steam pressure drop between the power plant and capture plant. This design limits steam availability in upset conditions.

The power plant turbines consist of nine stages: two in the HP turbine, two in the IP turbine, and five in the LP turbine. The design conditions for the power plant model are given in Table 5.3. The power plant algebraic equations were solved for a range of values for Q_{boiler} and q_v. The resulting values for temperature, pressure, and flowrate of the extracted steam were implemented as an n-D Lookup Table in Simulink®. The flue gas flowrate was assumed to be directly proportional to Q_{boiler} and flue gas composition was assumed to be constant for all power plant loads.

Table 5.3: Power plant operating conditions

	Value
P_{boiler}	24.1 MPa
T_{boiler}	593°C
Q_{boiler} (full-load)	1410 MW
Q_{RH} (full-load)	357 MW
$\hat{H}_{feedwater}$	1250 kJ/kg
$P_{condenser}$	6.89 kPa
C_v (extraction valve)	0.248 m^2

5.2.3 CO_2 Compression and EOR Facility

The compressor discharge pressure was always regulated at 150 bar, so that manipulating the compressor operation effectively changed the suction pressure and volumetric flow. Pressure changes in the CO_2 injection well were ignored. The compressor was assumed to be at steady state, and no restrictions were placed on achievable CO_2 flowrates.

The implications of ignoring compressor operating constraints are described in the Discussion.

5.3 Plantwide Control Strategy

A regulatory control strategy consists of feedback and feedforward controllers that regulate a process to its steady state in the presence of disturbances and set point changes. In this work, the Simulink® discrete-time PID Controller function block in parallel form was used for feedback control. Level controllers were configured to be P-only and all other feedback controllers were PI. The controllers were tuned using the Tyreus-Luyben continuous cycling method (Seborg et al., 2011). Controller outputs were limited to physically significant values (for example $0 \leq q_v \leq 1$) and the upper limit for flows was set at 150% of the design value. The anti-windup method was activated to discharge the integrator if a controller became saturated. Perfect flow control was assumed everywhere except for the steam extraction valve. The controllers proposed here would, in practice, be the master loop of a cascaded controller where the output is the set point for a nested flow controller. Condensers and coolers were assumed to have perfect temperature control; dynamics and constraints associated with cooling water were not considered.

This section describes the plantwide control strategy for the integrated amine plant, including inventory stabilization and higher level control objectives. The higher level objectives are related to energy performance, stability, and satisfying demand requirements. Table 5.4 lists the step changes used to test the plantwide control strategy for the four case studies considered in this work.

Table 5.4: Step changes examined in this case study

Case	Step Change
1	5% decrease in CO_2 delivery rate
2	5% decrease in steam extraction rate
3	5% decrease in power plant load
4	5% decrease in power plant load

5.3.1 Inventory Stabilization

Inventory stabilization was a primary objective for the design of a regulatory control strategy for the capture plant. There are five levels that must be controlled: absorber sump, absorber chimney tray, flash tank, stripper overhead condensate tank, and water recycle tank. The pump or valve immediately downstream of the controlled inventory served as the MV for these level CVs. Additionally, there is a surge tank (either rich or lean) where the level was allowed to fluctuate. The pump immediately following the surge tank set the solvent circulation rate for the process through a flow controller. A comparatively small surge tank inventory was examined in this work. In practice, a small surge inventory may limit the maximum allowable ramp rate of the solvent circulation pump to prevent cavitation.

In addition to level control, the regulatory control strategy must maintain the process water balance to stabilize the inventory. While the main purpose of the water wash section of the absorber column is to remove volatile amine emissions, it also plays a key role in the overall water balance. To avoid a net condensation or evaporation of water in to or out of the solvent, the flowrate of water exiting with the scrubbed flue gas to the atmo-

sphere must match the flowrate of water to the absorber column from the DCC. The water recycle flowrate around the water wash was used as the MV to control the temperature of the scrubbed gas exiting to the atmosphere. By selecting the correct set point for this temperature, the amount of water in the outlet gas matches that of the inlet gas and the water balance is maintained. At steady state, the water overflowing from the water wash to the absorber distributor is equal to the water condensed from the stripper overhead minus (or plus) the water condensed (or evaporated) in the absorber column.

In the event of process disturbances, the water wash temperature set point may not be achieved at all times or may not be correct to maintain zero water accumulation at the current set of conditions. A makeup or bleed water flowrate from the water recycle tank was included to account for mismatch in the absorber inlet and outlet water content. If the amine concentration is deviating from its desired set point, water can be added to or removed from the tank to compensate. In the simulation used here, the water makeup/bleed flowrate was calculated analytically so the water balance was always perfectly maintained. In a true plant, the amine concentration will likely be measured periodically in an offline titration, and operators will manually add or remove water from the system based on the titration results. Alternatively, the set point for the absorber outlet gas temperature could be adjusted to ensure the proper amine concentration is achieved.

Over time, the amine will degrade and makeup amine will be required (Mazari et al., 2014). The degradation process occurs at a much slower time scale than the process disturbances considered in this work and does not significantly affect the results. In practice, fresh amine will likely be added to the surge tank if the level in the tank begins to decrease. When the amine concentration is at its desired value, the drop in level indicates that amine

has been lost due to degradation and the degraded product has been removed through a reclaiming operation. The model assumes no amine was lost through any mechanism, and therefore amine makeup was not required in this simulation.

5.3.2 Higher Level Control Objectives

The AFS has five remaining MVs which have not yet been assigned to a specific control objective: the multi-stage compressor (which sets the flowrate of stripped CO_2), the steam valve position (which sets the amount of steam extracted from the IP/LP crossover), the solvent circulation rate, and the two bypass flows. Previous work has demonstrated that maintaining L/G in the absorber at a constant value maintains stable operation in the absorber column (Lawal et al., 2010; Ceccarelli et al., 2014). Additionally, large fluctuations in the solvent flowrate, which may occur if F_s is assigned as a MV, will require longer residence times to assure stable level control and a larger inventory in the surge tank to prevent pump cavitation. Constant L/G should result in manageable changes in F_s that are proportional to power plant load.

The bypass flows of the AFS are responsible for recovering energy from steam stripped along with the CO_2 from the aqueous solvent, thereby increasing the reversibility of the process (Lin and Rochelle, 2016). In order to simplify the control strategy and avoid generating convoluted results, the bypass flows were controlled to maintain their respective bypass ratio at a constant value of 9% for the cold bypass and 35% for the warm bypass. While the bypass flows are important for system energy performance, they do not play a large role in the interconnection of the capture plant with the power plant or EOR facility. Maintaining these flows at their design conditions in the presence of the small process

changes investigated here should not significantly impact the overall energy performance of the system. Developing a control strategy that optimizes these bypass flows in the presence of a disturbance will be considered in future work.

Amine scrubbing is a thermal swing process, and operating the stripper at higher temperature leads to more efficient energy performance (Lin and Rochelle, 2016). The system in this work was designed so the flash tank operates at 150 °C, which represents a reasonable compromise between efficiency and thermal degradation of PZ (Freeman, 2011). The hottest point in the system, the temperature of the steam heater (T_{SH}), was selected as a CV for all cases examined here. If the steam valve was an available DOF, it was assigned as the MV to control T_{SH}. Otherwise, the multi-stage compressor was used as the MV. T_{FT} was not selected as the CV because it is directly influenced by the stripper liquid temperature and responds more slowly to the steam valve than T_{SH} as a result of its larger liquid hold-up.

The control strategy for the capture plant described in this section is given in Figure 5.4. The controllers shown were responsible for inventory stabilization, as well as the higher level objectives of constant L/G ratio in the absorber and constant bypass ratios in the AFS. The two available DOFs, the steam valve and multi-stage compressor, are outlined in the figure because they have not yet been assigned to a higher-level process objective.

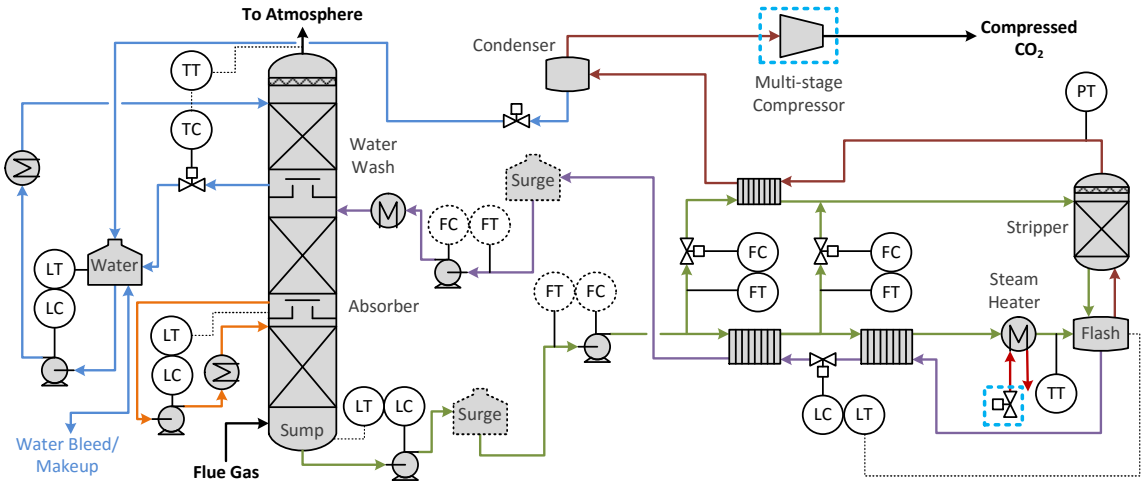

Figure 5.4: The capture plant P&ID shows controllers (C) and transmitters (T) for flow (F), level (L), pressure (P), and temperature (T). There is an option for a lean surge tank or a rich surge tank, along with the corresponding solvent circulation pump. The available DOFs (steam valve and multi-stage compressor) are outlined.

5.4 Simulation Results

There are two remaining DOFs available to assign to CVs: the multi-stage compressor operation and the steam extraction valve. Four different control configurations have been considered, summarized in Table 5.5. These configurations, described in the following sections, represent bounding cases where economic and operational objectives of one system component (EOR facility, power plant, or capture plant) dominate the process control strategy.

Table 5.5: CVs for the multistage compressor and steam extraction valve MVs

Case	Compressor	Steam Valve
1	F_{CO2}	T_{SH}
2	T_{SH}	F_{steam}
3	Rem	T_{SH}
4	P_{ST}	T_{SH}

The discrete-time PI control law is given in Equation 5.5:

$$u = \overline{u} + K_P(x_{SP} - x_k) + K_I t_s \sum_{k=-\infty}^{n} (x_{SP} - x_k) \tag{5.5}$$

where K_P is proportional gain, K_I is integral gain, u is the MV, $\overline{u}$, is the controller bias, x is the CV, and x_{SP} is the CV set point. A one second sampling time (t_s) was assumed. The parameters for the controllers used in this work are listed in Table 5.6.

Table 5.6: P and PI controller parameters

u	$\overline{u}$	x	x_{SP}	K_P	K_I
F_{FT}	99.3 kmol/s	l_{FT}	9.8 m	-540 kmol/m·s	–
F_{IC}	102 kmol/s	l_{CT}	1.0 m	-1950 kmol/m·s	–
F_{SU}	103 kmol/s	l_{SU}	2.6 m	-1950 kmol/m·s	–
F_{WW1}	32.1 kmol/s	l_{WT}	1.0 m	-590 kmol/m·s	–
F_{WW2}	30.9 kmol/s	T^V_{WW}	315.2 K	65 kmol/K·s	0.477 kmol/K·s^2
q_v	1	T_{SH}	426.0 K	0.0500 1/K	0.0220 1/K·s
F_{CO2}	2.50 kmol/s	T_{SH}	426.0 K	-2.00 kmol/K·s	-0.0733 kmol/K·s^2
		Rem	90%	0.0160 kmol/s	4.88 X 10^{-5} kmol/s^2
		P_{ST}	6.01 bar	-0.0120 kmol/bar·s	-5.30 X 10^{-3} kmol/bar·s^2

5.4.1 Case 1: Control CO_2 Delivery

The CO_2 delivery rate to the EOR facility is important for stable operation of the CO_2 injection well. Additionally, there may be contractual obligations, well capacity constraints, and economic objectives from oil production that are associated with the CO_2 delivery rate. If F_{CO2} is set external to the capture plant to satisfy EOR requirements, the DOF from the multi-stage compressor is lost. In Case 1, F_{CO2} was controlled by the compressor, and a 5% step change decrease in F_{CO2} was examined. The remaining DOF, the steam draw-off valve, was assigned to control T_{SH} at its design set point. The results from Case 1 are shown in Figure 5.5. This strategy resulted in a fast change in EOR operation, a slow approach to a new steady state in the capture plant (including the multi-stage compressor), and a fast initial response followed by a slow approach to new operating conditions in the power plant.

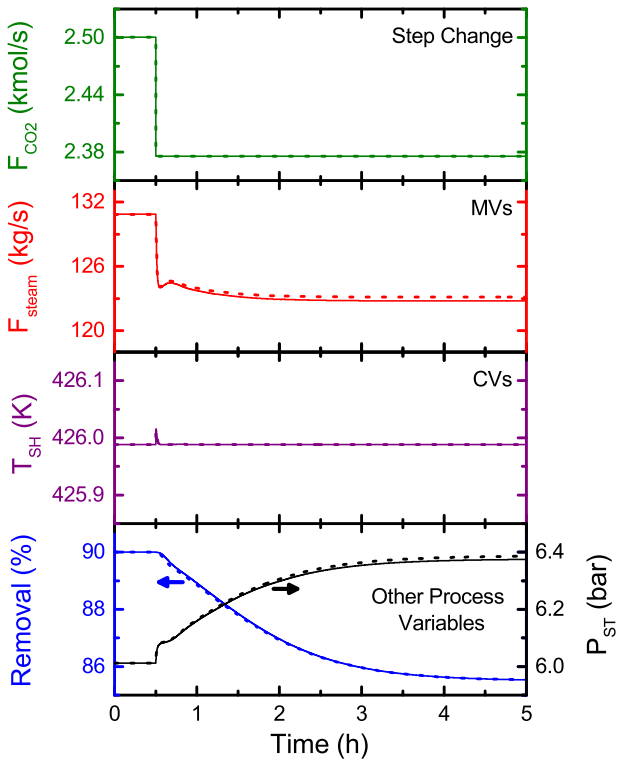

Figure 5.5: Case 1 results in response to a 5% set change in CO_2 delivery rate with a 2.5 min lean (solid) or rich (dashed) surge tank inventory out of a 17.7 min total system residence time

5.4.2 Case 2: Control Steam Flowrate from IP/LP Crossover

Varying the rate of steam extraction from the IP/LP crossover affects the stability of the coal-fired power plant operation, analogous to the CO_2 delivery rate affecting the stability of the EOR facility. The steam rate also plays an important role in flexible capture. Flexible capture refers to manipulating the steam extraction rate in order to change the rate of electricity production. In flexible capture, the capture plant is used as either an ancillary service to respond to peak demand or a quasi-producer that can bid in to electricity markets

during high-price periods (Cohen et al., 2012a,b; Khalilpour, 2014; Zaman and Lee, 2015). In Case 2, F_{steam} was set by the power plant, which resulted in the loss of the DOF from the steam extraction valve. The multi-stage compressor was used to control T_{SH} in this scenario. A 5% step change decrease in the set point for F_{steam} was introduced, shown in Figure 5.6. This strategy resulted in a fast change in power plant operation, a slow approach to steady state in the capture plant, and an initial large change followed by a slow approach to a new steady state in the CO_2 delivery rate. T_{SH} was tightly controlled to its set point by making aggressive moves in the compressor operation; constraints on the compressor ramp rate may make less aggressive tuning of the temperature controller necessary for practical implementation.

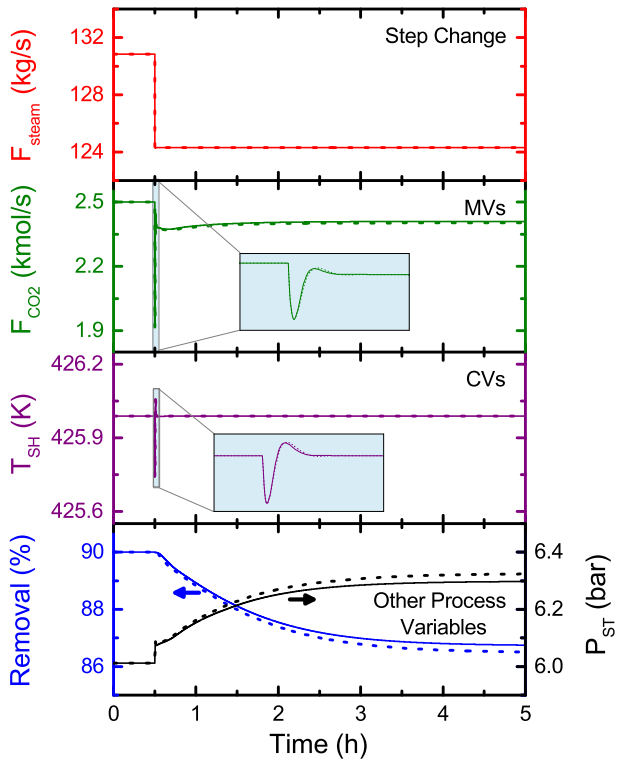

Figure 5.6: Case 2 results in response to a 5% step change in steam extraction rate with a 2.5 min lean (solid) or rich (dashed) surge tank inventory out of a 17.7 min total system residence time. The highlighted portion of the MV and CV graphs has been expanded to show the fast control action.

5.4.3 Case 3: Control Capture Rate

Controlling the CO_2 removal rate from the flue gas may be economically important in the case of a high carbon tax or obligatory in the case of strict regulatory requirements. Case 3 controls Rem to 90% with F_{CO2} as the MV. This is in contrast to previous work that attempted to control Rem using F_s (Panahi and Skogestad, 2011, 2012; Ziaii-Fashami, 2012; Lawal et al., 2010; Nittaya et al., 2014). Figure 5.7 gives the results of this strategy

in response to a 5% decrease in power plant load. A prolonged, damped oscillation was observed in the process variables, largely because of feedback created by the solvent circulation loop. Less aggressive tuning could eliminate the oscillatory behavior, but will not improve the response time.

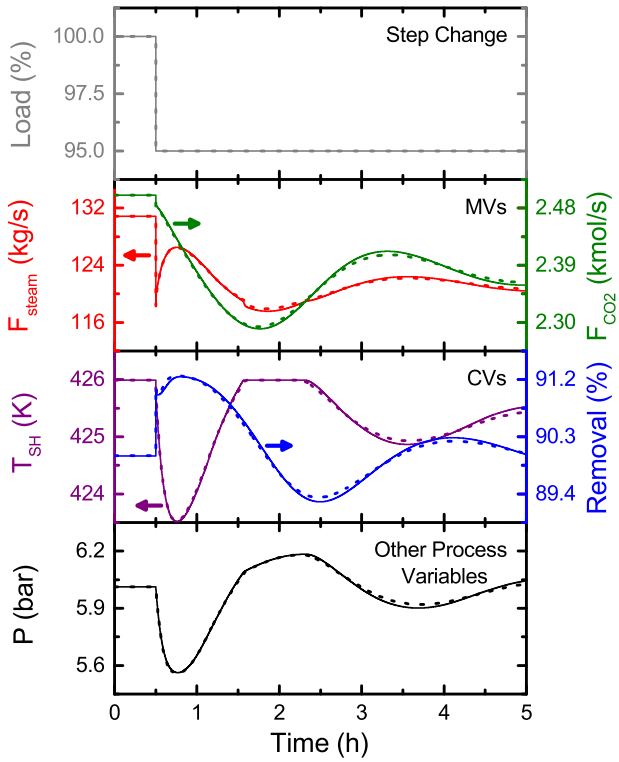

Figure 5.7: Case 3 results in response to a 5% step change in boiler load with a 2.5 min lean (solid) or rich (dashed) surge tank inventory out of a 17.7 min total system residence time and maintaining a constant L/G ratio in the absorber

5.4.4 Case 4: Control Stripper Conditions

While Cases 1–3 have controlled a specific flowrate (F_{CO2} in Case 1, F_{steam} in Case 2, and CO_2 flowrate in the flue gas out of the absorber in Case 3), the primary objective of

Case 4 is to maintain the stability of the overall system. This was achieved by controlling T_{SH} and P_{ST}, which effectively sets a constant lean loading. The same 5% load disturbance in Case 3 was introduced, and the results are plotted in Figure 5.8. Initially, there was a fast increase in Rem as the absorber sees a smaller flue gas flowrate and a fast decrease in F_{steam} as Q_{boiler} is dropped by 5%. Following this initial disturbance, the variables quickly approached a new steady state. It was not possible to control T_{SH} to its set point because the steam availability was limited by the steam valve design.

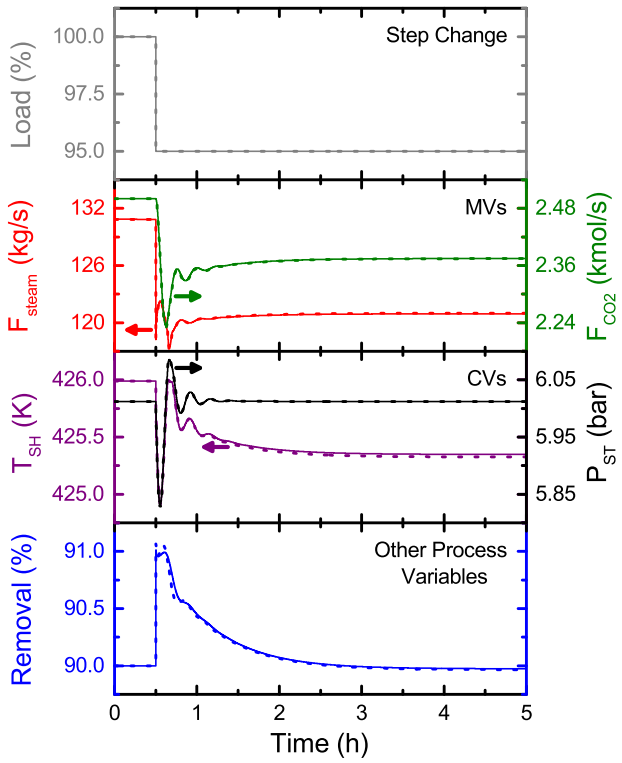

Figure 5.8: Case 4 results in response to a 5% step change in boiler load with a 2.5 min lean (solid) or rich (dashed) surge tank inventory out of a 17.7 min total system residence time and maintaining a constant L/G ratio in the absorber

5.5 Discussion

Figures 5.5–5.8 show that trade-offs clearly exist when satisfying the objectives of one system component. Controlling either F_{steam} or F_{CO2} eliminated a DOF in the capture plant, and resulted in a slow approach to steady state for Rem in response to process changes. Controlling T_{SH} and P_{ST} brought all system components to a new steady state the fastest, but did not take into consideration system economics. Tightly controlling Rem in the absorber was not possible with feedback control only. Rem control is complicated by the significant solvent recycling and energy recovery in amine scrubbing, which is utilized to reduce capital and operating costs in the plant. The high amount of recycling leads to control loop interactions and time scale multiplicity in the process variables (Walters et al., 2014). Advanced process control will be considered in future work to address removal control.

5.5.1 Process Design Implications

Depending on the selected control strategy, the process equipment requires different designs to achieve the desired control action without violating equipment constraints. The design implications for the stripper column and steam extraction valve are examined here.

5.5.1.1 Stripper Column

The stripper column is susceptible to flooding because changes in T_{ST}, P_{ST}, and gas molar flowrate (F_{ST}^{V}) are expected during upset conditions. The gas volumetric flowrate through the column is directly proportional to T_{ST} and F_{ST}^{V}, and inversely proportional to P_{ST}. The stripper diameter should be designed so that the column does not flood as a

result of the necessary control action taken to respond to process disturbances. Figure 5.9 shows the gas volumetric flowrate through the stripper for Cases 1–4. When the volumetric flowrate is increased from its design value, the stripper column is approaching its flooding limit.

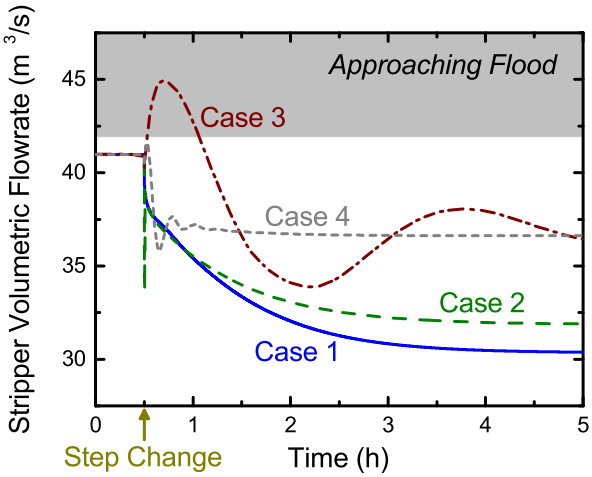

Figure 5.9: Stripper gas volumetric flowrate

The control strategies from Cases 2 and 4 will not result in flooding with well-tuned controllers. For Case 2, a decrease in steam extraction valve position from 100% open with temperature control resulted in less stripped CO_2 and therefore a lower total volumetric flowrate. For Case 4, a decrease from 100% boiler load with temperature and pressure control also decreased F_{ST}^{V}. Case 1 resulted in a monotonic decrease in volumetric flow as a result of a decrease in the set point for F_{CO2}. If the F_{CO2} set point had been increased instead of decreased, a monotonic increase in volumetric flow would have been observed. Unlike Case 4 where P_{ST} is controlled by manipulating F_{CO2}, P_{ST} is an uncontrolled process variable in Case 3 and an initial increase in volumetric flow was observed. The

initial decrease in P_{ST} for Case 3 that resulted from the power plant load drop caused a significant increase in gas density. Based on these observations, over-designing the stripper column may be necessary if a removal rate more than 90% is required at 100% boiler load or if P_{ST} is not a CV.

5.5.1.2 Steam Extraction Valve

A trade-off exists with the steam extraction valve between the energy performance at the design operating conditions and the ability to maintain temperature control in response to disturbances. The valve was designed to be 100% open at full load conditions to minimize the steam pressure drop between the IP/LP crossover and the capture plant. However, Figure 5.10 shows that the valve was saturated and unable to achieve the T_{SH} set point when the power plant was operating at part load (Cases 3 and 4). If temperature control of the AFS is an important objective, a larger valve is required.

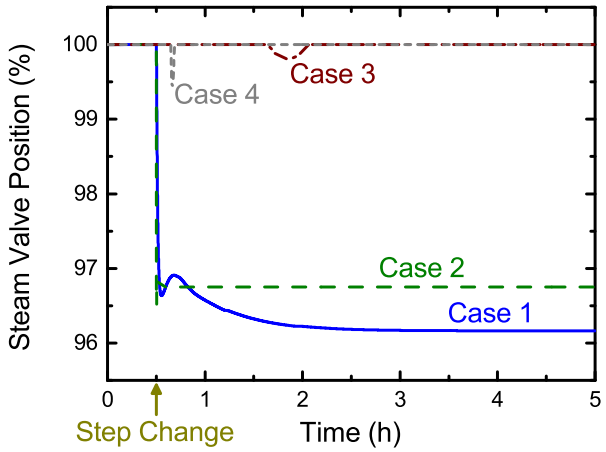

Figure 5.10: Steam valve stem position

5.5.2 Multi-stage Compressor Configurations

The results reported in the previous section assumed that the desired value for F_{CO2} was always achievable. The compressor action that would have been required to produce the values of F_{CO2} from Figures 5.5–5.8 is explored in more detail here. Two types of off-design compressor flow regulation were considered: (1) variable speed and (2) adjustable inlet guide vanes (IGVs). Lüdtke (2004) provides typical compressor performance maps for different flow regulation methods, using a 7-stage acid gas compressor as a case study. The reported performance maps were normalized by the design conditions and are shown in the first column of Figure 5.11. It was assumed that these maps are representative of the 5-stage CO_2 compressor that would be required in this work to compress the gas from P_{ST} to 150 bar with a design compression ratio per stage of less than 2.0. The design point, as well as the final steady state conditions of each case study, are labeled on the performance maps.

The right column of Figure 5.11 describes the path the compressor would have taken to get from the design point to the final steady state for each case. Flow regulation with a variable speed compressor resulted in speed variations between 96–103% of the design speed for all cases, which are readily achievable off-design compressor operating conditions. With the exception of Case 3, flow regulation through adjustable IGVs adequately handled the step changes investigated in this work. Adjustable IGVs have limited ability to operate at over-design conditions and therefore have a lower capacity limit than speed regulation. By extrapolating the performance map, Case 3 required a vane angle that was well beyond the capacity limit for the compressor. Adjustable IGVs may also be problematic for Case 1 in a scenario where greater than 90% capture was required.

Reaching the compressor surge limit is undesirable because activating anti-surge control decreases the compressor efficiency. When the steam flowrate was decreased in Case 2, the compressor decreased the volumetric flowrate in order to control T_{SH}. This control action caused the compressor to approach its surge limit for both variable speed and adjustable IGVs methods. Less aggressive temperature control tuning may be advantageous in Case 2 to prevent the use of anti-surge control. The modest step changes considered in this work resulted in steady state volumetric flowrates that were within 89% of the design flowrate, well beyond the compressor surge limit. Reaching the surge line becomes unavoidable with larger changes in process conditions that result in small volumetric flowrates. The performance map for the adjustable IGVs compressor has a surge line with a less steep slope than the variable speed compressor, so it can operate at lower volumetric flows before activating anti-surge control.

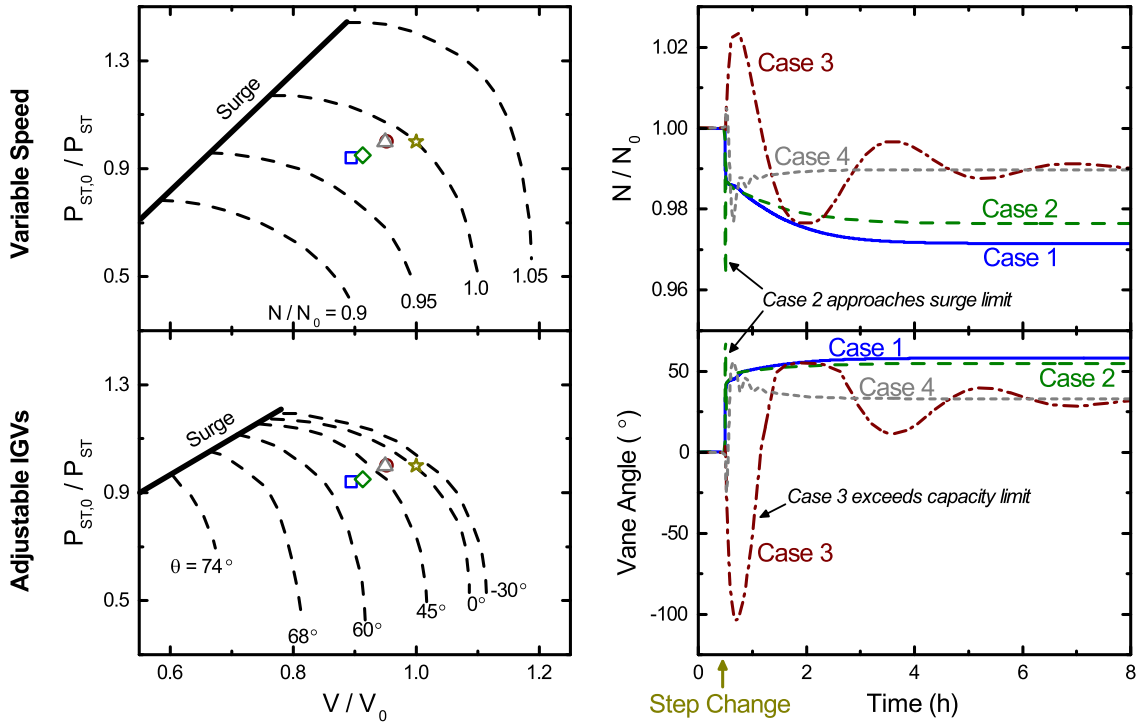

Figure 5.11: The top and bottom rows show the performance of a variable speed compressor and a compressor with adjustable IGVs, respectively, for this case study. The left column contains typical compressor performance maps adapted from a 7-stage acid gas compressor given in Lüdtke (2004). The steady state operating points from each case is denoted on the map (Design Case: ☆, Case 1: □, Case 2: ◇, Case 3: ○, and Case 4: △). The right column reports the compressor speed (N) or vane angle (θ) that would have been required based on the performance maps to achieve the desired control action from each case.

5.5.3 Rich versus Lean Surge Tank

A surge tank with uncontrolled level containing 14% of the total steady state liquid inventory was included for all cases. The surge tank allowed F_s to be set by the pump at the tank effluent, as well as dampened disturbances that propagate between the absorber and AFS. A short residence time of 2.5 min was arbitrarily selected to demonstrate the

performance of a system with a small solvent hold-up. A small amine inventory is desirable because it mitigates safety risks from a process failure, avoids operational challenges for solvents operating near their solid solubility limit, and is economically favorable by decreasing amine makeup costs. Negligible differences in the system performance were observed in Figures 5.5–5.8 between a rich surge tank and a lean surge tank for any of the cases examined. This is consistent with the results from Chapter 3, which showed that the characteristic time of the total CO_2 inventory for processes with rich or lean surge tanks converged as the surge tank inventory was decreased.

In order to more clearly understand the control implications of the surge tank location, Case 3 was repeated with a surge tank residence time of 15 min so that approximately half of the system inventory was in the surge tank. The controller tuning was not changed from the previous conditions. Chapter 3 showed that a rich surge tank allows for a faster initial change in Rem compared to a lean surge tank in response to an open-loop step change in the stripper. Figure 5.12 shows that the rich surge tank with a 15 min inventory allowed for more effective control of Rem than a lean surge tank. In other words, the more lean inventory in the process, the less aggressive the control action can be in the stripper. A rich surge tank may present other operational benefits not captured in this analysis. The rich tank will dampen disturbances from the absorber to the AFS, which operates at high temperature and high pressure with multiple bypass flows and is therefore sensitive to changes in process conditions. The rich tank will also decrease flowrate disturbances to the AFS since the rich flowrate is controlled, which is important for heat exchanger performance. There is the option to strip dissolved oxygen from the rich tank by N_2 sparging to pre-

vent oxidative degradation of the amine (Voice and Rochelle, 2013). Therefore the system should be designed with a rich surge tank.

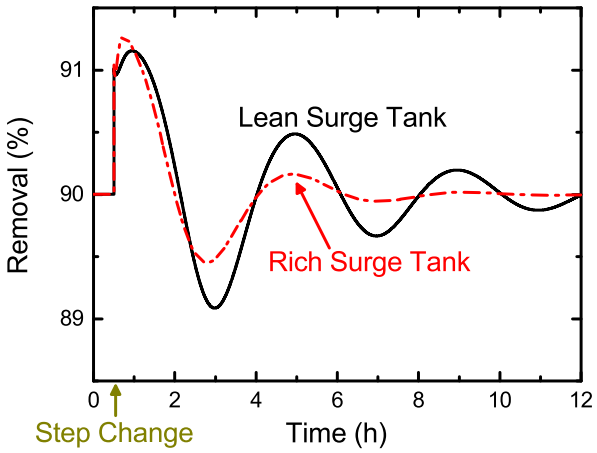

Figure 5.12: Case 3 repeated with a 15 min residence time in the lean (solid) or rich (dashed) surge tank

5.6 Conclusions

The recommended plantwide regulatory control strategy for the amine scrubbing process described in this work is summarized as follows:

- Control the absorber sump, absorber chimney tray, flash tank, overhead condensate tank, and water recycle tank levels using the valve or pump at the inventory effluent.
- Control the vapor outlet temperature of the water wash using the water wash recycle flowrate in order to maintain the water balance.
- Control the absorber L/G ratio using the solvent circulation flowrate for absorber performance.

- Control the steam heater outlet temperature using either the steam extraction valve (preferred) or multi-stage compressor (if steam valve not available) for the AFS energy performance.
- Control the CO_2 delivery rate, CO_2 removal rate, or stripper pressure using the multi-stage compressor to achieve higher level control objectives.

In order to satisfy the objectives of one system component (either the oil produced by the EOR facility, the electricity generated by the power plant, or the CO_2 captured by the amine scrubbing plant), the performance of the other system components suffers. When the CO_2 delivery rate was decreased by 5%, 3.1 and 0.9 hours were required for the CO_2 removal rate and steam extraction rate to come within 5% of their new steady state values, respectively. The removal rate did not reach 95% of its response for 3.0 hours and the delivery rate had an initial decrease of 23% in response to a 5% decrease in steam extraction rate. Tightly controlling CO_2 removal using only feedback control was not feasible because of the positive feedback from the recycle of lean amine back to the absorber column. When controlling the stripper temperature and pressure, 1.9 hours were required to bring the MVs to within 5% of their new steady state values in response to a 5% decrease in boiler load.

The design of process equipment depends on the process control strategy. The stripper column diameter must be over-designed if stripper pressure is not controlled or removal rates greater than the design conditions are required. In order to ensure stripper temperature control by manipulating the steam extraction valve, the valve must be sized to be less than 100% open at design conditions at the expense of the energy performance of the design case.

A rich surge tank is more advantageous than a lean surge tank for controlling the CO_2 removal because changes in lean loading are propagated more quickly to the absorber without the dampening effects caused by a large lean inventory. More aggressive controller tuning can be used as a result. However, the difference in performance between rich and lean surge tanks is negligible with a small surge tank inventory.

5.7 Notation

Greek

ϕ_{Di}	flow constant for uncontrolled steam extraction to next stage
ϕ_{Dxi}	flow constant for uncontrolled steam extraction to feedwater heater

Roman

C_v	steam extraction valve flow coefficient
F_{CO2}	CO_2 flowrate through multi-stage compressor
F_{FT}	flash tank effluent flowrate
F_{IC}	absorber chimney tray effluent flowrate
F_{SU}	absorber sump effluent flowrate
F_{WW1}	water tank effluent flowrate
F_{WW2}	water wash chimney tray effluent flowrate

$\hat{H}_{feedwater}$	specific enthalpy of boiler feedwater
K_I	integral gain
K_P	proportional gain
l_{CT}	absorber chimney tray level
l_{FT}	flash tank level
l_{SU}	absorber sump level
l_{WT}	water tank level
P_{boiler}	supercritical boiler pressure
$P_{condenser}$	LP steam condenser
P_{ST}	stripper pressure
Q_{boiler}	duty applied to boiler feedwater
Q_{RH}	reheating duty applied to steam exiting HP turbine
q_V	steam extraction valve stem position
Rem	CO_2 removal rate from the flue gas
T_{boiler}	supercritical boiler temperature
t_s	sampling time
T_{SH}	steam heater outlet temperature
T_{WW}^V	water wash outlet vapor temperature
$\overline{u}$	nominal value for manipulated variable

u	manipulated variable
x	controlled variable
x_{SP}	set point for controlled variable

Chapter 6

Process Control of the Advanced Flash Stripper

6.1 Introduction

To minimize the parasitic load of the amine scrubbing plant, the advanced flash stripper (AFS) using aqueous piperazine (PZ) has been proposed (Rochelle et al., 2011; Lin et al., 2014) and demonstrated at the pilot scale (Chen et al., 2014). The process flow diagram is shown in Figure 6.1. This intensified process contains two rich amine bypass flows for energy recovery, increasing the degrees of freedom compared to the basic process where all rich solvent enters the top of a reboiled stripper. The AFS also has two points with high-temperature amine: the steam heater effluent and the flash tank hold-up. A conventional reboiled stripper only contains one high-temperature location in the reboiler sump. It is not obvious a priori which process variables should be controlled using the bypass flowrates or the steam extraction flowrate from the power plant for the AFS configuration.

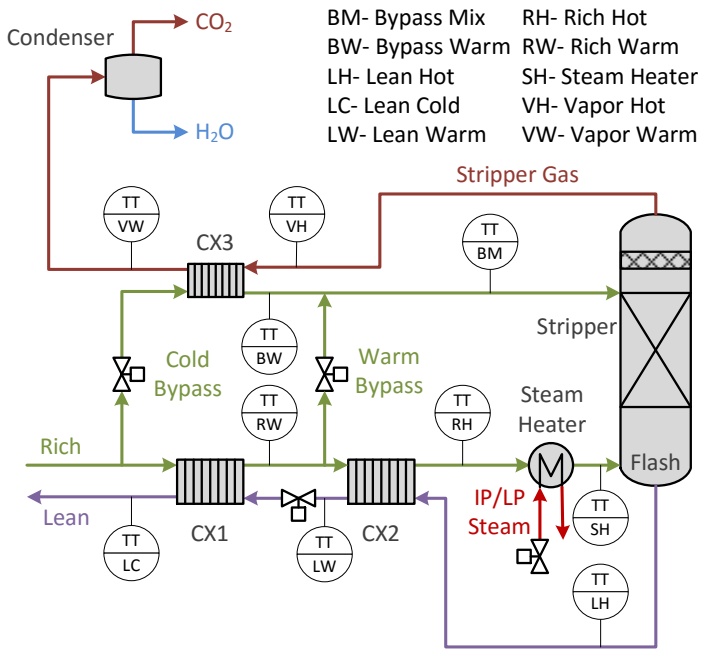

Figure 6.1: Advanced flash stripper flowsheet showing possible temperature transmitter (TT) locations with unique steady state values

6.1.1 Literature Review

Previous work on the dynamics and control of post-combustion amine scrubbing has mostly considered processes with a conventional reboiled stripper using the first generation solvent monoethanolamine (MEA). The maximum stripper temperature and pressure are limited by solvent degradation, which in this configuration are approximately 120 °C and 2 bar, respectively (Davis, 2009). Using a heuristic approach, the most obvious controller configuration for the reboiled stripper system is to control the reboiler temperature by manipulating the steam extraction rate and the stripper pressure by manipulating the multi-stage compressor (or a suction throttle valve). This strategy was examined by Ziaii-

Fashami (2012) and found to result in a stable response to disturbances. However, there is no guarantee that the final steady state will have optimal energy performance or satisfy process objectives such as maintaining a desired CO_2 capture rate. Lawal et al. (2010) and Nittaya et al. (2014) effectively used this strategy by controlling the reboiler temperature and assuming a constant stripper pressure. Walters et al. (2016b) developed a plantwide regulatory control strategy for a process using PZ with the AFS for CO_2 regeneration. In this study, which primarily focused on the interaction between the amine scrubbing plant, power plant, and enhanced oil recovery facility, the steam heater effluent temperature was controlled and constant cold and warm rich bypass flowrate ratios were maintained in the presence of a disturbance. This strategy was found to be effective when stripper pressure control was active, but again there is no guarantee of achieving optimal conditions in off-design operation.

Since previous research has not provided guidance on a control strategy that will optimize the performance of the AFS, this work evaluates "self-optimizing" control as a method to minimize the system energy demand. Self-optimizing control refers to a control strategy where near-optimal operation is achieved by maintaining constant controller set points, without needing to re-optimize in the presence of a disturbance (Morari et al., 1980; Skogestad, 2000). Figure 6.2 provides a graphical representation of this concept. A self-optimizing control strategy was employed by Panahi and Skogestad (2011, 2012) to identify controlled variables (CVs) for the reboiled stripper with MEA. Their analysis showed that the best self-optimizing CV for the steam valve manipulated variable (MV) was the temperature of tray 16 of a 20 tray stripper column. Pressure was controlled by a

suction throttling valve. A similar strategy was used in this work to assign self-optimizing CVs to the bypass flowrate MVs of the AFS.

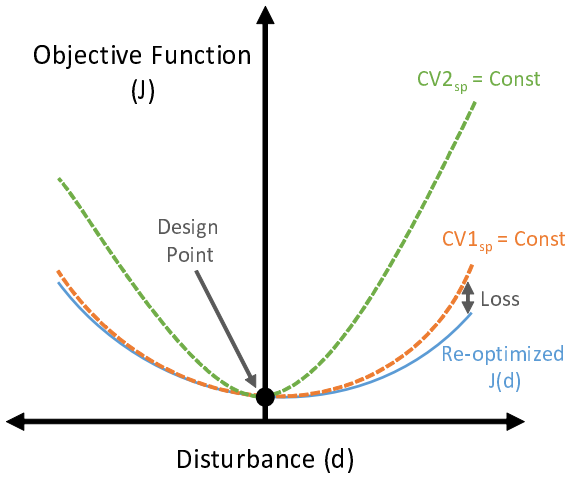

Figure 6.2: Two CV candidates (CV1 and CV2) are compared to demonstrate the idea of self-optimizing control. CV1 is a better self-optimizing variable than CV2 because only a marginal loss in steady state system performance is observed when the set point for CV1 remains constant in the presence of a disturbance (Skogestad, 2000).

6.1.2 Motivation and Scope

The Separations Research Program at the University of Texas at Austin tested the AFS configuration and PZ solvent in a 0.1 MWe equivalent amine scrubbing pilot plant in March 2015 (Chen, 2015; Sachde, 2016; Lin et al., 2016). The temperature set point for the flash inventory was varied between 140–150 °C, and this set point was achieved by manipulating the steam flowrate to the steam heater with a PID controller. The cold and warm bypass flowrates were set by flow controllers. During the initial phase of pilot plant operation, the set points for the flow controllers for a given set of conditions were

determined through an offline optimization using an Aspen Plus® simulation. After gaining operational experience, the plant operators manually adjusted the flowrate set point for the cold bypass to maintain the vapor outlet temperature of the vapor/liquid cross exchanger (T_{VW}) and the flowrate set point for the warm bypass to maintain the temperature difference at the top of the stripper ($T_{VH} - T_{BM}$). These temperatures have physical significance in the energy performance of the system. T_{VW} represents energy that is ultimately lost to the overhead condenser, which operated at 40 °C in the pilot plant. Heat exchange within the stripper packing is related to $T_{VH} - T_{BM}$. However, there was no attempt to systematically identify the best CVs for the AFS system in pilot plant operation.

The goal of this work was to develop a feedback process control strategy that maintains stable and near-optimal operation of the AFS in response to disturbances and off-design operating conditions. Three main objectives were considered: (1) identify self-optimizing CVs to assign to the rich bypass flowrate MVs, (2) determine an appropriate CV for the steam extraction rate MV, and (3) demonstrate the performance of the selected process control configuration. The results generated here will provide guidance for future pilot plant activity, as well as commercial scale implementation of the AFS.

6.2 Process Simulation

6.2.1 High-Fidelity Steady State Model

A high-fidelity steady state Aspen Plus® model for the PZ/H_2O/CO_2 system was previously developed using hundreds of laboratory data points to regress 43 thermodynamic parameters (Frailie, 2014), and the model has been extensively validated with pilot plant results (Chen et al., 2013, 2014). The stripper is modeled with rate-based heat and

mass transfer and equilibrium reactions. The high-fidelity model was used in this work to simulate off-design steady state conditions of the AFS and evaluate the energy performance of the system.

Case 11 of NETL (2010) provides specifications for a 550 MWe coal-fired power plant to be used when evaluating post-combustion CO_2 capture technologies. Trimeric Corporation (2015) reported a base case design for the AFS in an amine plant that removes 90% of CO_2 from the flue gas of the NETL case study, which was developed using the high-fidelity Aspen Plus® simulation. The specifications of the AFS from the Trimeric design were used for the design case in this work. All equipment dimensions remained constant from the values reported by Trimeric.

Rich amine from an absorber enters the system with a given temperature (T_{abs}), loading (α_{rich}, mol CO_2/mol alkalinity), and flowrate (F_{abs}), and a constant amine concentration (C_{rich}) of 5 molal PZ for all cases. The steady state pressure of the flash (P_{flash}) was also kept constant at its design point, implying that the lean loading (α_{lean}) remained constant for a given operating temperature of the flash tank. The performance of the main cross exchangers (CX1 and CX2) were predicted by the power law expression in Equation 6.1:

$$UA = c_{CX} F_{avg}^{0.7} \tag{6.1}$$

where UA is the overall heat transfer coefficient (MW/K), F_{avg} is the average flowrate through the exchanger (mol/s), and c_{CX} is a constant fit for both exchangers to give the correct $LMTD$ at the design point. The UA of the vapor/liquid exchanger (CX3) was assumed to be constant. The constant values used in all off-design cases are listed in Table 6.1.

Table 6.1: Constant Parameters in the High-Order Model

Parameter	Value
C_{rich}	5 molal PZ
P_{flash}	5.93 bar
c_{CX1}	0.328 MW/K·(mol/s)$^{0.7}$
c_{CX2}	0.187 MW/K·(mol/s)$^{0.7}$
UA_{CX3}	2.6 MW/K

6.2.2 Low-Order Dynamic Model

Walters et al. (2016c) previously developed and validated a low-order dynamic model in MATLAB® for an amine scrubbing process containing the AFS, and the low-order model was used in this work to evaluate the closed-loop performance of the proposed control structure. This first principles model contains a semi-empirical relation for vapor-liquid equilibrium and rate-based heat and mass transfer with adjustable transfer coefficients. The model parameters for the AFS system designed for the NETL 550 MWe power plant are given in Walters et al. (2016c). The steady state muti-stage compressor in this work was assumed to be able to achieve any specified CO_2 flowrate. The model was incorporated into a Simulink® flowsheet using S-function implementation.

A steady state representation of the power plant reported by Walters et al. (2016b) to predict off-design turbine operation was also included as part of the low-order dynamic model. This turbine model uses Stodola's Ellipse Law for calculating uncontrolled steam extractions between turbine stages (Cooke, 1983). The steam extraction valve at the intermediate pressure (IP)/low pressure (LP) turbine crossover of the steam cycle was designed

to be 100% open at design conditions to minimize the steam pressure drop between the power plant and capture plant. This design limits steam availability in upset conditions. The wide-open valve design is unique to advanced solvents with relatively high degradation temperatures, because the steam heater of the AFS is able to take advantage of using steam at the pressure of the IP/LP crossover. The steady state power plant model was included in the Simulink® flowsheet as an n-D lookup table, where the steam extraction flowrate and IP/LP crossover pressure are a function of the boiler load (Q_{boiler}), extraction valve stem position, and steam temperature at the steam heater.

6.3 CV Selection for Bypass Flowrate MVs

An ideal self-optimizing CV should be sensitive to changes in the corresponding MV, while the optimum value of the CV should be insensitive to process disturbances. The following sections describe how these two steady state criteria of sensitivity to the MV and optimum value insensitivity were evaluated using the high-fidelity Aspen Plus® model to select a self-optimizing CV candidate to assign to each bypass flowrate MV. Disturbances in absorber operation, including changes in F_{abs}, α_{rich}, and T_{abs}, were examined in this work. A disturbance in steam availability, which was assumed to result in a lower operating temperature of the flash tank (T_{LH}), was also explored. Since temperature is a measurable quantity that is related to the system energy balance, the unique system temperatures shown in Figure 6.1 were considered for possible CV candidates. The standard deviation (σ) of temperatures predicted by the model for a range of specified conditions was used as a metric to quantify sensitivity.

6.3.1 Temperature Sensitivity to Bypass Flowrates

A CV candidate must be responsive to changes in the MV for a feedback controller to be effective (Seborg et al., 2011). This section examines the sensitivity of the unique AFS temperatures to changes in the cold bypass (CBP) and warm bypass (WBP) flowrates. The range of values considered for the CBP and WBP flowrates are listed in Table 6.2, and the resulting process temperature sensitivities are plotted in Figure 6.3. The standard deviations were normalized by the total flowrate range for each bypass (ΔF) so that a direct comparison could be made. The figure shows that the system temperatures were more sensitive to changes in the CBP than the WBP, but there is not an obvious trend between the two sensitivities.

Table 6.2: Design values and tested ranges for bypass flowrates

	Design	Range
F_{CBP} $\left(\begin{smallmatrix}\text{kg/s}\\(\%\text{ of total flow})\end{smallmatrix}\right)$	212 (8.4%)	0–454 (0–18%)
F_{WBP} $\left(\begin{smallmatrix}\text{kg/s}\\(\%\text{ of total flow})\end{smallmatrix}\right)$	832 (35%)	238–998 (10–42%)

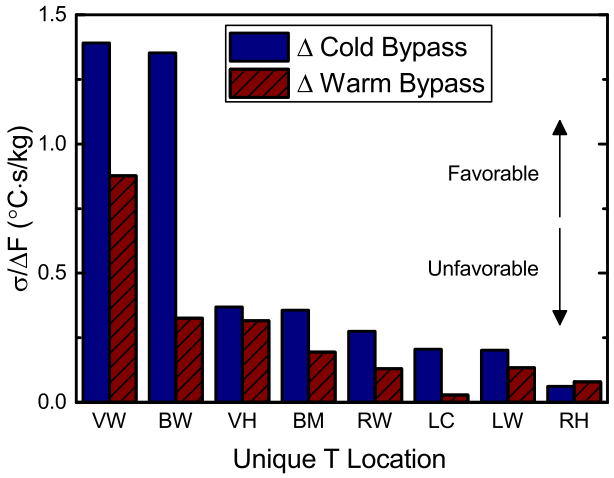

Figure 6.3: Temperature sensitivity to changes in the bypass flowrates predicted by the high-fidelity Aspen Plus® model

6.3.2 Optimum Off-design Temperature Values

The optimum off-design values of the CV candidates were examined to determine variables with insensitive optimums. The ranges of off-design values listed in Table 6.3 were considered. For each off-design case, the bypass flowrates were determined according to the optimization problem in Equation 6.2:

$$\begin{aligned} &\underset{F_{CBP},\, F_{WBP}}{\text{minimize}} && Q_{SH} \\ &\text{subject to:} && T_{LH} = T_{LH,sp} \\ &&& P_{ST} = 5.93\ bar \end{aligned} \tag{6.2}$$

where Q_{SH} is the heat duty of the steam heater. Because the stripper was maintained at a constant pressure, compression work was not included in the objective function.

Table 6.3: Design values and tested ranges for disturbance variables

	Design	Range
F_{abs} (kg/s)	2524	-10%–+10%
α_{rich} (mol CO_2/mol alkalinity)	0.378	0.341–0.416
T_{abs} (°C)	48	38–58
T_{LH} (°C)	150	140–155

Figure 6.4 plots the sensitivity of the optimum values for the unique AFS temperatures to the range of off-design conditions from Table 6.3. Variables with low sensitivities are favorable because controlling them at their design set point will lead to near-optimal operation (see Figure 6.2). While there are some process temperatures that had insensitive optimum values for certain off-design conditions, there was no temperature that had an insensitive optimum across all off-design scenarios evaluated. The optimum value of TT-LC, for example, had the lowest sensitivity to variations in T_{LH} and α_{rich}, but there was a significant change to the optimum in response to deviations in T_{abs}. It was also observed that the optimums of all AFS temperatures were generally insensitive to a disturbance in F_{abs}, leading to the conclusion that variations in flowrate will not significantly impact system energy performance for any selected self-optimizing CV.

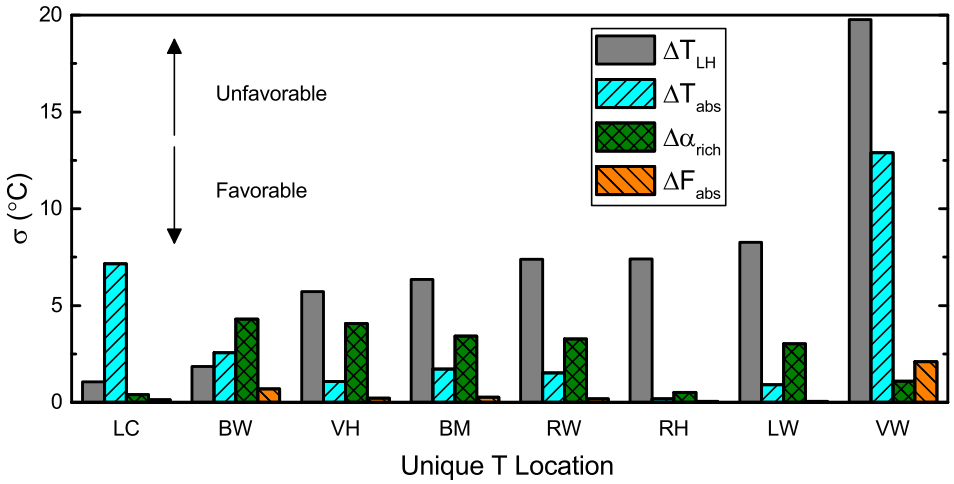

Figure 6.4: Sensitivity of optimum off-design temperature values predicted by the high-fidelity Aspen Plus® model in response to changes in F_{abs}, α_{rich}, T_{abs}, and T_{LH}

6.3.3 Self-optimizing CV Candidate Identification

Figure 6.4 showed that there was not an obvious choice for a self-optimizing CV from the unique process temperature measurements. To potentially identify a more favorable CV candidate, temperature differences (ΔT's) were considered instead of direct temperature measurements. ΔT's have been previously used to design a non-interacting control system for a distillation process (Bequette and Edgar, 1989). With eight distinct process temperatures in combinations of two, there are $\frac{8!}{2!(8-2)!}$ = 28 possible steady state ΔT's that can be measured for the AFS. The following criteria were used to select a ΔT CV candidate for each bypass flowrate:

1. ΔT must be more sensitive to changes in the corresponding bypass MV than the other bypass flowrate

2. ΔT sensitivity must be greater than the median sensitivity to the bypass MV

3. Sensitivity of the optimum off-design ΔT must be within the lower quartile of optimum value sensitivities to changes in α_{rich}, T_{abs}, F_{abs}, and T_{LH}

Only one ΔT for each flowrate met these three criteria for the CBP and WBP: $T_{VH} - T_{BW}$ and $T_{VH} - T_{BM}$, respectively. The optimum value sensitivity analysis is plotted in Figure 6.5. To confirm that a reasonable MV-CV pairing was made, a relative gain array (RGA) was calculated from the steady state process model in Equation 6.3. Values close to unity on the diagonal indicate that there should be minimal loop interaction in this multiloop control structure.

$$\begin{array}{cc} & \begin{array}{cc} CBP & WBP \end{array} \\ \begin{array}{c} T_{VH} - T_{BW} \\ T_{VH} - T_{BM} \end{array} & \begin{bmatrix} 0.998 & 0.002 \\ 0.002 & 0.998 \end{bmatrix} \end{array} \tag{6.3}$$

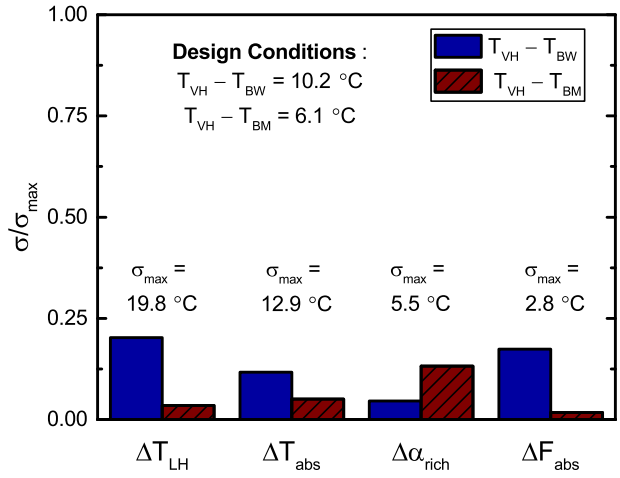

Figure 6.5: Sensitivity of optimum off-design values for $T_{VH} - T_{BW}$ and $T_{VH} - T_{BM}$ predicted by the high-fidelity Aspen Plus® model in response to changes in F_{abs}, α_{rich}, T_{abs}, and T_{LH}

Since $T_{VH} - T_{BW}$ and $T_{VH} - T_{BM}$ were both sensitive to changes in their corresponding bypass flowrate MV and have insensitive optimum values to all off-design conditions examined, they were selected as self-optimizing CV candidates for evaluation in the dynamic model. The proposed self-optimizing control structure is shown in Figure 6.6.

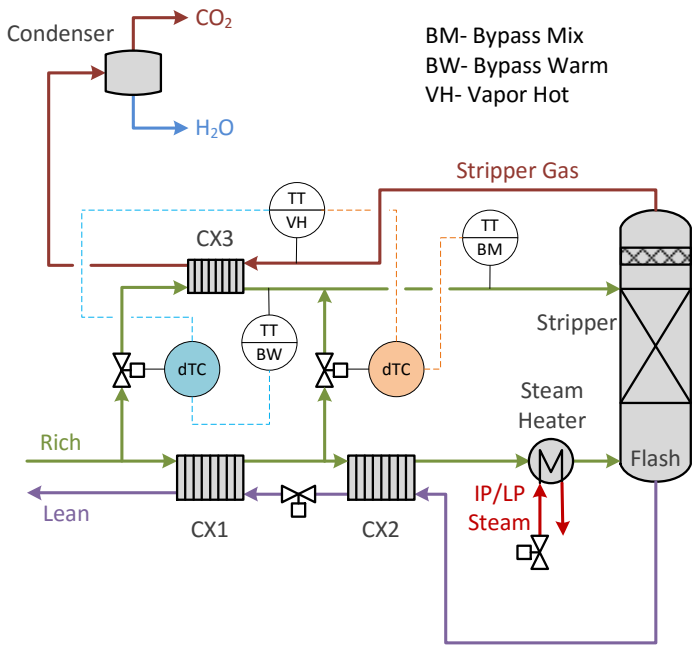

Figure 6.6: Proposed self-optimizing control structure for the rich bypass flowrates

6.4 CV Selection for Steam Flowrate MV

Steam is extracted from the IP/LP crossover of the power plant steam cycle to the convective heater of the AFS to regenerate the amine solvent. The steam extraction valve is an available MV to control the stripping temperature. As stated in the Introduction, there are two high-temperature amine locations in the AFS system: the steam heater effluent

(T_{SH}) and the flash tank (T_{LH}). In the Trimeric design, the flash tank operates at 150 °C, which is a reasonable compromise between efficiency and thermal degradation of PZ (Freeman, 2011). Because liquid from the stripper packing is also flowing into the flash tank, T_{SH} is operated slightly hotter than T_{LH} at 152.4 °C.

T_{SH} has a much quicker response to changes in steam flowrate than T_{LH} as a result of the small residence time of the convective heater compared to the flash tank. Additionally, T_{SH} is not directly influenced by the stripper temperature. Therefore, T_{SH} was selected as the CV to assign to the steam flowrate MV. This configuration has the advantage of being able to include meaningful temperature constraints in the controller to avoid exceeding solvent degradation limits in the convective heater.

T_{LH} is an important process variable for the AFS. α_{lean} is a function of flash tank temperature and pressure, and flash tank temperature also strongly influences heat exchange in all three cross heat exchangers as well as the stripper packing. As a result, controlling T_{SH} and allowing T_{LH} to float could negatively impact system performance. Two high-temperature control options were considered, shown in Figure 6.7. In Option 1, only T_{SH} was controlled using the steam extraction valve. Option 2 used a cascade control structure, where the inner loop was the T_{SH} controller and the outer loop provided the steam heater effluent temperature set point ($T_{SH,sp}$) to control T_{LH}. The closed-loop response of these two options is presented in the Dynamic Results section.

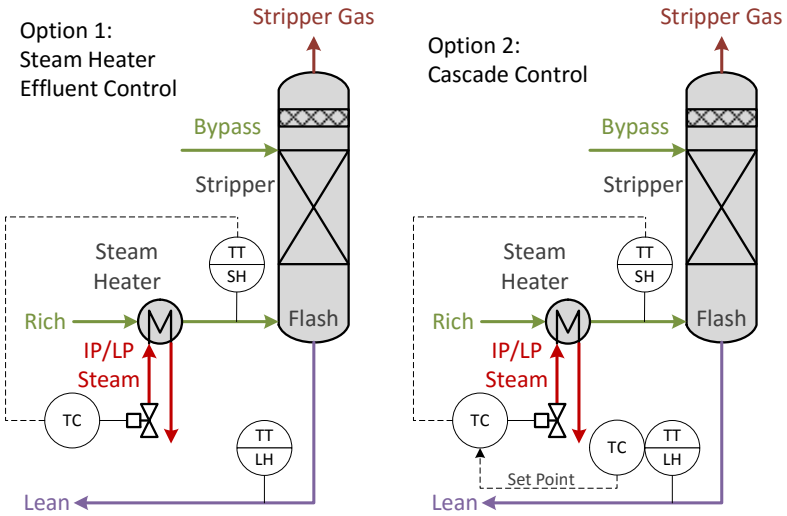

Figure 6.7: Control options for high-temperature stripping

6.5 Dynamic Results

The low-order model was used to evaluate the dynamic performance of the self-optimizing control strategy for the bypass flowrates (Figure 6.6) and the high temperature control options for the steam extraction rate (Figure 6.7). The controller tuning provided by Walters et al. (2016b) was used for the T_{SH}, stripper pressure, and flash tank level controllers. The stripper pressure set point was kept constant in this work. The Tyreus-Luyben continuous cycling method (Seborg et al., 2011) was used to tune the self-optimizing controllers and the outer loop of the cascade controller. Four disturbance cases were considered, as summarized in Table 6.4. The dynamic results for each case are described in the following subsections.

Table 6.4: Disturbances considered for evaluating closed-loop performance of the AFS

Case	Disturbance
1	Q_{boiler} (90–100%)
2	α_{rich} (0.360–0.398)
3	T_{abs} (43.7–53.7 °C)
4	$T_{SH,sp}$ or $T_{FT,sp}$ (140–150 °C)

6.5.1 Case 1: Power Plant Load Disturbance

The capture plant in this work was designed to treat all flue gas from a 550 MWe power plant operating at full load. In Case 1, part-load operation of the power plant boiler was examined. The power plant model assumes the flue gas flowrate is proportional to Q_{boiler}. If the CO_2 absorber column operates at a constant liquid to gas ratio, F_{abs} will be proportional to Q_{boiler} as well. A typical ramp rate for a supercritical coal-fired power plant is 2%/min (Peltier, 2005). Case 1 tested the proposed control strategy with a ramp disturbance in Q_{boiler} between 100–90% load, and the results are presented in Figure 6.8. The Case 1 results show that the bypass flowrates exhibited an inverse response during the ramping period, followed by a fast approach to a new steady state. When Q_{boiler} was ramped down and steam availability was limited, there was no difference between the cascaded and non-cascaded options because the steam extraction valve was saturated. In the ramp up period, however, the cascaded strategy showed better performance because deviations in the flash tank temperature were minimized.

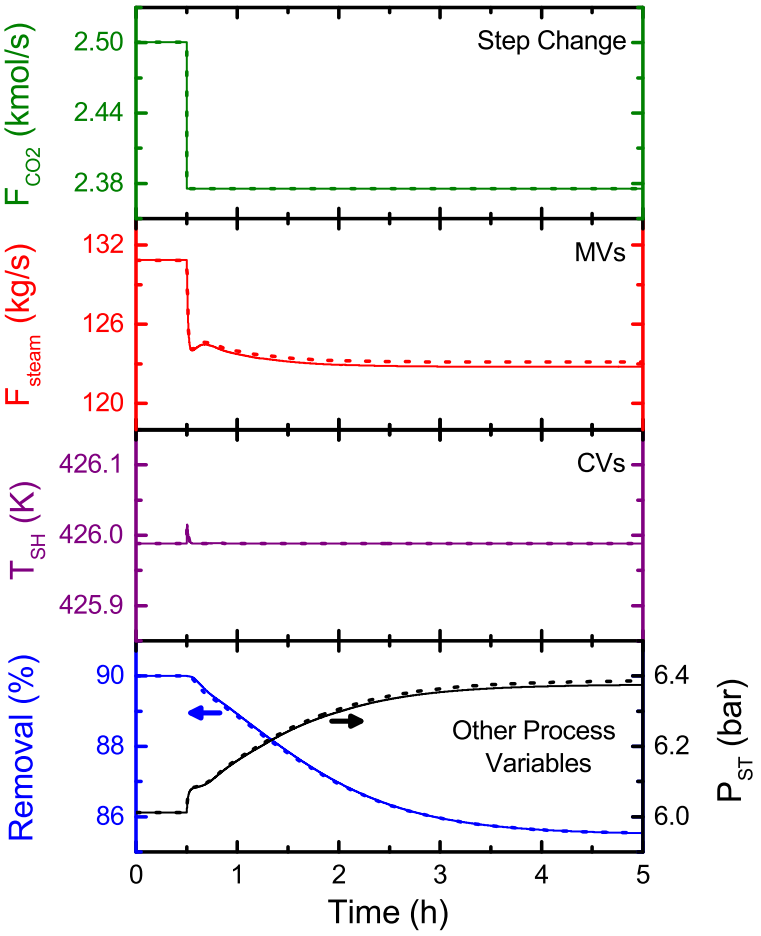

Figure 6.8: Case 1 closed-loop response with steam heater effluent control only (solid) and cascade control (dashed)

6.5.2 Case 2: α_{rich} Disturbance

Case 2 investigated a step change disturbance in α_{rich}, which could result from a change in the inlet flue gas CO_2 concentration to the absorber. If the AFS is operated at a constant temperature and pressure (and hence α_{lean}) with constant F_{abs}, an increase in α_{rich} corresponds to stripping more CO_2 and a decrease in α_{rich} corresponds to stripping

less CO_2. Figure 6.9 gives the Case 2 results. Similar to Case 1, an inverse response was observed in the bypass flowrates before reaching steady state. There was not a clear benefit for the cascade option in this case.

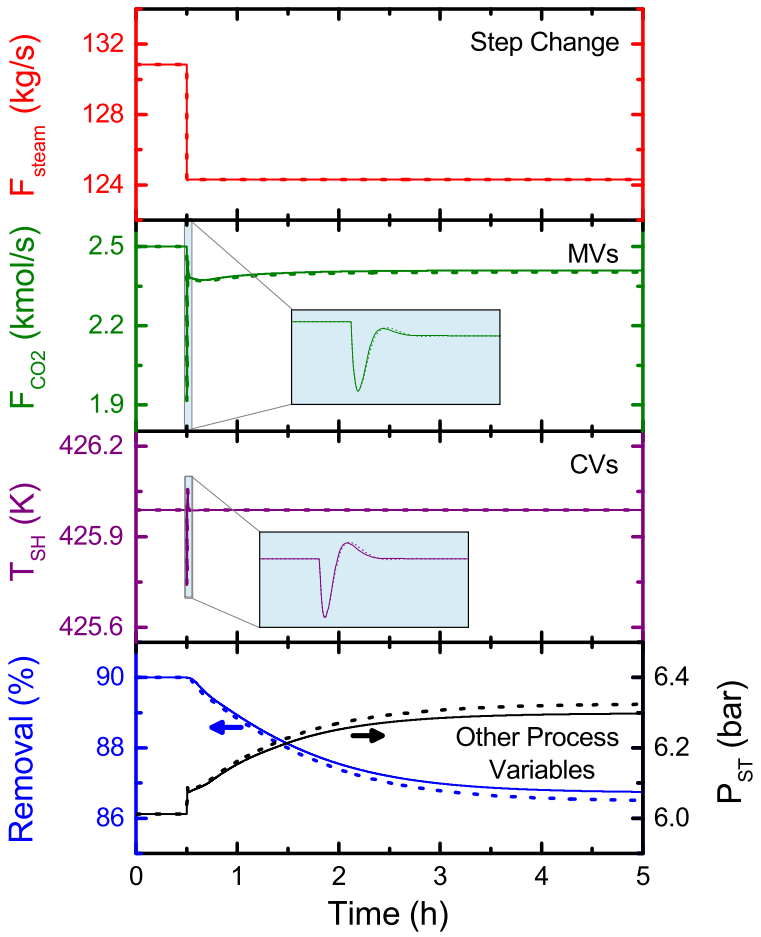

Figure 6.9: Case 2 closed-loop response with steam heater effluent control only (solid) and cascade control (dashed)

6.5.3 Case 3: T_{abs} Disturbance

Depending on the operation of absorber intercooling or the direct contact cooler for flue gas pre-treating, temperature variations may occur in the inlet solvent to the AFS. Step change disturbances in T_{abs} were considered for Case 3, and the closed-loop system response is plotted in Figure 6.10. The self-optimizing strategy resulted in smooth transitions for the bypass flowrates, compared to the previous two cases where an inverse response was observed. Cascade control maintained a more consistent α_{lean} than the non-cascaded option, which will in turn lead to more consistent operation of the absorber when the lean solvent is recycled.

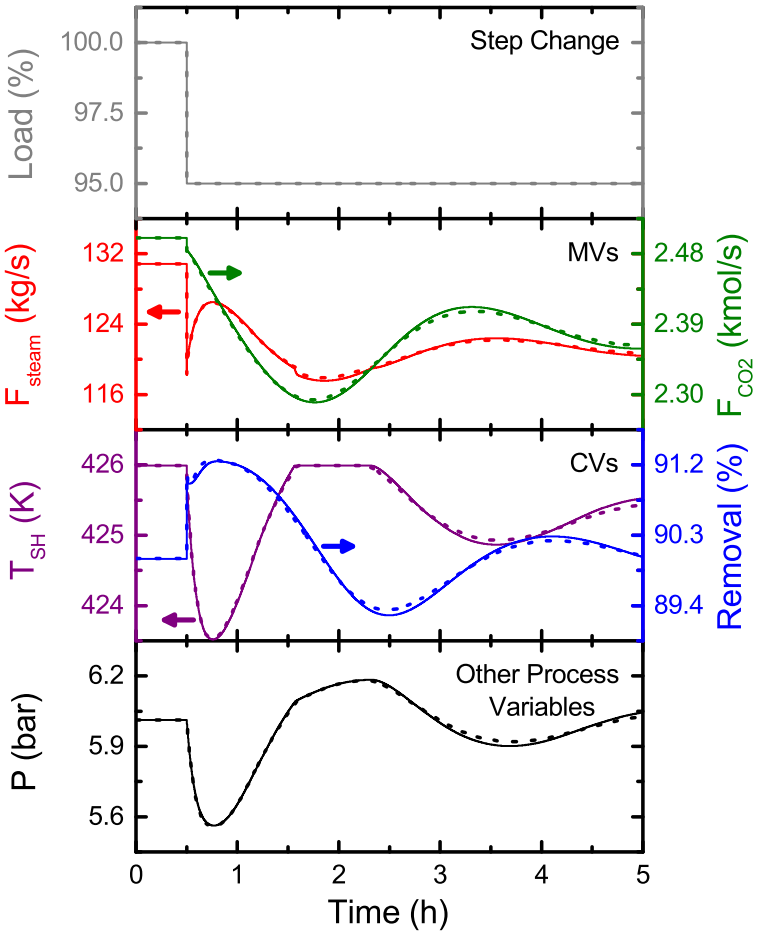

Figure 6.10: Case 3 closed-loop response with steam heater effluent control only (solid) and cascade control (dashed)

6.5.4 Case 4: $T_{LH,sp}$ Disturbance

Flexible capture has been proposed as an operational strategy to maximize revenue from the CO_2 capture plant. Flexible capture refers to manipulating the steam extraction flowrate in order to change the rate of electricity production. With this strategy, the capture plant is used as either an ancillary service to respond to peak demand or a quasi-producer

that can bid in to electricity markets during high-price periods (Cohen, 2012; Cohen et al., 2012b; Khalilpour, 2014; Zaman and Lee, 2015). In Case 4, a flexible capture scenario was examined where the high-temperature amine set point (either $T_{SH,sp}$ for Option 1 or $T_{LH,sp}$ for Option 2) was decreased in steps over time. Case 4 results are given in Figure 6.11. The cascaded structure led to aggressive action in the steam extraction valve to quickly change the flash tank temperature, which is undesirable from the perspective of the power plant steam turbines. In a flexible capture scenario where the objective is high-temperature set point tracking (as opposed to a high-temperature regulation problem like the previous three cases), less aggressive tuning in the outer loop of the cascade controller may be required. While the magnitude of change for the bypass flowrates was much larger in Case 4 than the other cases, the manipulated flows were still able to quickly reach a new steady state with the self-optimizing strategy.

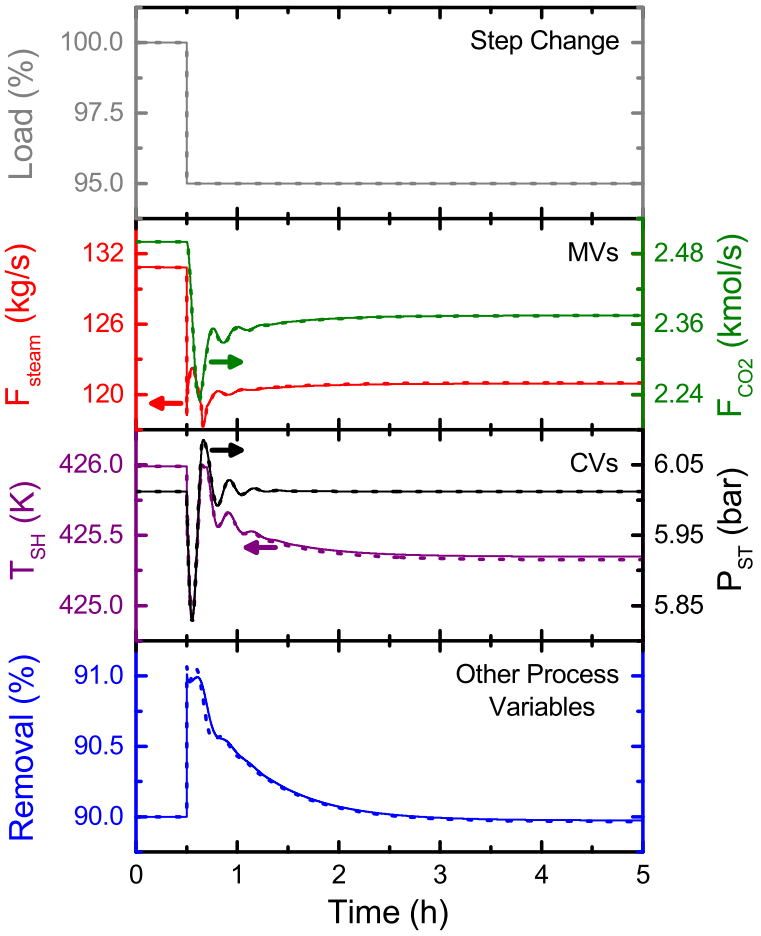

Figure 6.11: Case 4 closed-loop response with steam heater effluent control only (solid) and cascade control (dashed)

6.6 Discussion

Figures 6.8–6.11 showed that the proposed self-optimizing control strategy from Figure 6.6 resulted in a satisfactory closed-loop response for the bypass flowrates. By selecting ΔT's that were sensitive to changes in the corresponding bypass MV, loop in-

teractions were minimized despite the large amount of energy integration in the AFS system. RGA further confirmed that the two bypass control loops should have minimal loop interaction. The high-order model was used to quantify the energy performance of the self-optimizing strategy by comparing the steam heater duty requirement with constant self-optimizing variables to the true system optimum. Table 6.5 demonstrates that this straightforward feedback control strategy will bring the plant to within 1% of the true steady state optimum for a wide range of off-design conditions.

Table 6.5: Energy performance of self-optimizing strategy

Disturbance		Optimum Duty (MW)	Self-Optimizing Duty (MW)	Q_{loss} (%)
ΔF_{abs}	+10%	301.77	304.74	0.99
	-10%	242.37	242.50	0.05
$\Delta \alpha_{rich}$	+10%	295.67	295.74	0.02
	-10%	237.79	238.23	0.19
ΔT_{abs}	+10 °C	264.06	265.00	0.36
	-10 °C	275.61	276.56	0.35
ΔT_{LH}	+5 °C	374.60	375.83	0.33
	-10 °C	160.50	161.49	0.62

Cascade control was generally advantageous when steam availability was not limited. Additionally, maintaining a constant α_{lean} in the cascaded option will prevent disturbances from propagating back to the absorber. This phenomena, which results from the heavy material recycle in amine scrubbing, was not captured in the results presented here because the absorber model was not included. The Case 4 results clearly demonstrated that

the controller tuning for the outer loop of the cascaded controller should depend on whether the control objective is regulation or set point tracking.

6.7 Conclusions

A self-optimizing control strategy for the rich bypass flowrates of the advanced flash stripper was proposed, where the cold bypass flow is manipulated to control the temperature difference on the hot end of the vapor/liquid cross exchanger and the warm bypass flow is manipulated to control the temperature difference at the top of the stripper packing. A dynamic model was used to show that this strategy has a fast and stable closed-loop response to process disturbances. A high-fidelity steady state model was used to calculate energy performance, and less than 1% energy loss compared to the true optimum was observed for the range of disturbances examined. Cascade control, where the inner loop controls the steam heater effluent temperature and the outer loop controls the flash tank temperature, resulted in a more favorable dynamic response than temperature control of the steam heater effluent alone. However, there was no advantage to cascade control when the steam extraction valve was saturated. Cascade control also resulted in aggressive control moves in the steam extraction flowrate for a temperature tracking objective. The self-optimizing strategy with high-temperature cascade control will be implemented in future scheduled pilot plant tests of the advanced flash stripper configuration.

Chapter 7

Dynamic Modeling and Control of an Intercooled Absorber

7.1 Introduction

Absorber intercooling has been proposed to reduce the temperature bulge that occurs as a result of the exothermic absorption of CO_2. Operating the absorber at a lower temperature increases both the maximum solvent capacity and driving force within the column, resulting in better energy performance of CO_2 regeneration and decreased packing requirements (Sachde and Rochelle, 2014). Figure 7.1 shows an absorber column with in-and-out intercooling (where solvent leaving the top bed of packing is cooled and returned to the same point within the column) and a water wash section for removing volatile amine emissions. In this chapter, a dynamic model of the intercooled absorber is developed, validated, and used to address process control of absorber operation.

7.1.1 Literature Review of Absorber Modeling

Several equation-based dynamic models have been presented for post-combustion CO_2 capture with a simple absorber. The complexity of these dynamic models can be roughly grouped into two categories as described by Walters et al. (2016c): medium-order or low-order. In a medium-order dynamic model, rate-based mass transfer is modeled with apparent species mass transfer coefficients (k_g and k_l for the gas and liquid, respec-

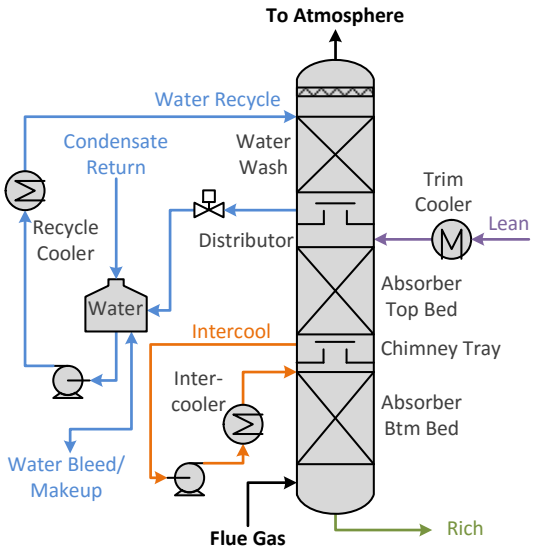

Figure 7.1: In-and-out intercooled absorber and water wash

tively) and reaction kinetics are embedded in an enhancement factor (E_{CO2}) or liquid film mass transfer coefficient ($k'_{g,CO2}$). Examples of medium-order dynamic absorber models include Kvamsdal et al. (2009), Ziaii-Fashami (2012), Harun et al. (2012), Enaasen Flø et al. (2015). While these medium-order models have generally addressed CO_2 kinetics, they contain an approximate semi-empirical thermodynamic model to predict the equilibrium partial pressure of the liquid.

Low-order dynamic absorber models further approximate reaction kinetics by assuming an instantaneous reaction at the gas/liquid interface (Lawal et al. (2009)) or a constant overall mass transfer coefficient (Walters et al. (2016c)). Interestingly, the model by Lawal et al. (2009) assuming instantaneous reaction included a rigorous equation of state for the electrolyte system. There are no examples of high-order dynamic absorber models in the literature, where true component Maxwell-Stefan diffusion is used for rate-

Table 7.1: Summary of mass transfer and kinetic model complexity for CO_2 absorption

	High-Order	Medium-Order	Low-Order
Transport	Rate-Based (Maxwell-Stefan Diffusion)	Rate-Based (Variable Apparent k_g and k_l)	Rate-Based (Const. Apparent K_g)
Kinetics	Arrhenius Eq. in Discretized Liquid Film	Embedded in $k'_{g,CO2}$ or E_{CO2}	Instantaneous or Embedded in Const. K_g

Table 7.2: Previously published dynamic absorber models

	Type	Thermo	Transport	Kinetics
Ziaii-Fashami	Simple	Semi-Empirical	Rate-Based	$k'_{g,CO2}$
Kvamsdal et al.	Simple	Semi-Empirical	Rate-Based	E_{CO2}
Harun et al.	Simple	Semi-Empirical	Rate-Based	E_{CO2}
Enaasen Flø et al.	Simple	Semi-Empirical	Rate-Based	E_{CO2}
Lawal et al.	Simple	eNRTL	Rate-Based	Instantaneous
Walters et al.	Intercooled	Semi-Empirical	Rate-Based	Constant
This Chapter	Intercooled	eNRTL	Rate-Based	$k'_{g,CO2}$

based mass transfer and reaction kinetics are explicitly represented in a discretized liquid film with the Arrhenius equation. Table 7.1 describes the transport and kinetic methods for high-, medium-, and low-order absorption models, and Table 7.2 summarizes the thermodynamic, transport, and kinetic methods used in previous dynamic absorber modeling work. With the exception of Walters et al. (2016c), all previous dynamic models have been developed for the first generation solvent monoethanolamine (MEA).

7.1.2 Motivation and Scope

Dynamic models are useful for understanding the effects of disturbances on process operation, but there are no published medium-order dynamic models that have included absorber intercooling, as discussed in the literature review. Intercooling significantly changes the column temperature profile compared to a non-intercooled simple absorber (Sachde and Rochelle, 2014), and at least a medium-order model is likely required to accurately capture the behavior of the temperatures in dynamic and off-design conditions. The goals of this study are to: (1) develop a medium-order dynamic model for an intercooled absorber, (2) perform a steady state model validation through comparison with a high-order model, and (3) use the medium-order model to develop a feedback control strategy based on the column temperature profile to maintain consistent absorber operation in the presence of process disturbances.

7.2 Dynamic Model Development

An equation-based dynamic model of the intercooled absorber configuration in Figure 7.1 was developed and implemented in gPROMS®, an advanced process modeling platform. The following subsections describe the components of the medium-order model, including the absorber packing, water wash, and other auxiliary equipment. The complete model formulation is provided in the Supporting Information. 5 molal piperazine (PZ) was used as the solvent in this work because of its superior properties to MEA (Rochelle et al., 2011).

7.2.1 Absorber Packing

The absorber consists of two packed sections, with one above and one below the in-and-out intercooler. Mellapak 250X (MP250X) structured packing was modeled in this work, but any packing type could in principle be simulated by substituting the appropriate parameters. The equations representing a rate-based, nonequilibrium model for a packed section are described here.

7.2.1.1 Heat and Material Balances

In each bed of packing, the vapor enters at $z = 0$ and the liquid enters at $z = 1$, where z is the normalized axial domain. The component mass balances and the energy balance for the liquid phase are given in Equations 7.1–7.2, assuming plug flow. The liquid phase, which is flowing down the column, was discretized using a first order forward finite difference method. As the concentrations evolve over time, the component mole fractions must sum to unity (Equation 7.3).

$$\frac{\partial}{\partial t}\left(\varepsilon^L C_i^L\right) + \frac{1}{L \cdot S}\frac{\partial F_i^L}{\partial z} = N_i^L \qquad i = \text{CO}_2, \text{H}_2\text{O}, \text{PZ};\ 0 \le z < 1 \qquad (7.1)$$

$$\frac{\partial}{\partial t}\left(\varepsilon^L U^L\right) + \frac{1}{L \cdot S}\frac{\partial F_H^L}{\partial z} = N_H^L \qquad 0 \le z < 1 \qquad (7.2)$$

$$\sum x_i = 1 \qquad 0 \le z < 1 \qquad (7.3)$$

Liquid hold-up (ε^L), which determines the amount of liquid at each finite volume of packing, was not assumed to be constant in this work and was included as part of the time derivative term in the continuity equations. This is consistent with Ziaii-Fashami (2012) and in contrast to Kvamsdal et al. (2009) and Enaasen Flø et al. (2015) where ε^L was not included as part of the time derivative and Harun et al. (2012) where ε^L was incorrectly

omitted from the balance equations. Lawal et al. (2009) did not describe how mass hold-up on a stage was determined. If ε^L is calculated as a function of liquid flowrate but not included as part of the time derivative, this implicitly assumes that there are no dynamics associated with the total material balance. Treating ε^L as a constant assumes constant liquid molar (or mass) overflow in the packing.

Because the molar hold-up of the vapor is much smaller than that of the liquid, the vapor phase dynamics were ignored. This is a common assumption when modeling rate-based distillation (Taylor et al., 2003) and is consistent with Kvamsdal et al. (2009), Enaasen Flø et al. (2015), Lawal et al. (2009). PZ was assumed to be nonvolatile in the absorber ($y_{PZ} = 0$). Equations 7.4–7.6 show the vapor phase balances and the mole fraction summation requirement. The vapor phase, which is flowing up the column, was discretized using a first order backward finite difference method.

$$\frac{1}{L \cdot S}\frac{\partial F_i^V}{\partial z} = -N_i^V \qquad i = \mathrm{CO_2, H_2O, N_2, O_2};\ 0 < z \leq 1 \tag{7.4}$$

$$\frac{1}{L \cdot S}\frac{\partial F_H^V}{\partial z} = -N_H^V \qquad 0 < z \leq 1 \tag{7.5}$$

$$\sum y_i = 1 \qquad 0 < z \leq 1 \tag{7.6}$$

7.2.1.2 CAPE-OPEN Thermodynamic Package

An electrolyte non-random two-liquid (eNRTL) model was previously regressed in Aspen Plus® for a CO_2/PZ/H_2O system using hundreds of laboratory measurements, and the model has been validated extensively with pilot plant data (Frailie, 2014). To take advantage of this high-fidelity thermodynamic model, gPROMS® was interfaced with Aspen Properties® using the CAPE-OPEN standard (Piñol et al., 2011). A disadvantage to this

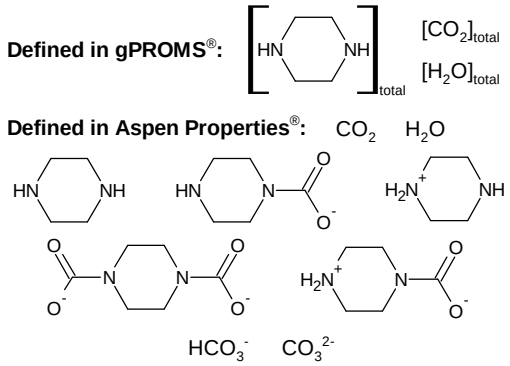

Figure 7.2: Only the total apparent species are defined in the gPROMS® model, while Aspen Properties® uses a true species representation

formulation is that the CAPE-OPEN package is treated as a black box by gPROMS®, and therefore the solver does not have access to the analytical derivatives of the thermodynamic parameters. CAPE-OPEN uses SI units for all parameters, so unit conversions were required for the property calls.

True and apparent species representations for the liquid phase are compared in Figure 7.2. The Aspen Properties® model uses a true species representation; however, the material balances presented in the previous section were only performed on the total apparent species in the liquid. Since the liquid speciation is not known in the dynamic model, a pressure-vapor fraction (P-VF) flash was performed for the liquid phase at all z (Equation 7.7). The pressure in the P-VF flash calculation is the equilibrium pressure of the liquid, not the mechanical pressure of the system.

$$flash = f\left(P^* \cdot 10^5, vf = 0, x_{CO}\right) \tag{7.7}$$

The flash calculation returns values for temperature, true liquid speciation, liquid volume, liquid enthalpy, and equilibrium vapor mole fractions. The values for enthalpy and

volume are per mole of true species, which were converted to apparent species for use in the dynamic model. The conversion was achieved by multiplying by the ratio of apparent molecular weight to true molecular weight. Since the vapor phase is not an electrolyte solution and therefore not speciated, vapor volume and enthalpy were called directly from the CAPE-OPEN package without performing a flash calculation (Equations 7.8–7.9).

$$\hat{H}^V = f(T^V, P \cdot 10^5, y_{CO}) \cdot 10^{-3} \tag{7.8}$$

$$\hat{V}^V = f(T^V, P \cdot 10^5, y_{CO}) \cdot 10^3 \tag{7.9}$$

For any Aspen Properties® calculation that requires mole fraction as an input, a value for all components defined in the Aspen Properties® model must be provided. A vector of mole fractions, x_{CO}, that contains the apparent values for CO_2, H_2O, and PZ and zero for all other components was defined for the liquid phase in Equations 7.10a–7.10b.

$$x_{CO,i} = x_i \qquad i = \text{CO}_2, \text{PZ}, \text{H}_2\text{O} \tag{7.10a}$$

$$x_{CO,i} = 0 \qquad i \neq \text{CO}_2, \text{PZ}, \text{H}_2\text{O} \tag{7.10b}$$

Similarly, a vector of vapor mole fractions, containing the values of CO_2, H_2O, N_2, and O_2 and zero for all other components was defined for the vapor phase in Equations 7.11a–7.11b. No speciation occurs in the vapor phase, so there is no distinction between true and apparent species for the gas side equations.

$$y_{CO,i} = y_i \qquad i = \text{CO}_2, \text{H}_2\text{O}, \text{N}_2, \text{O}_2 \tag{7.11a}$$

$$y_{CO,i} = 0 \qquad i \neq \text{CO}_2, \text{H}_2\text{O}, \text{N}_2, \text{O}_2 \tag{7.11b}$$

7.2.1.3 Interphase Flux

Rate-based material transfer of CO_2 and H_2O occurs between the bulk liquid and bulk gas within the absorber packing. PZ was assumed to be nonvolatile ($N_{PZ}^{L} = 0$) and N_2 and O_2 were assumed to be insoluble ($N_{N2}^{V},\ N_{O2}^{V} = 0$) in this model. The component flux from the bulk vapor to the bulk liquid was calculated using a linear driving force model, according to Equation 7.12. Convective mass transfer was ignored in this analysis because CO_2 and H_2O are relatively dilute in the bulk gas, allowing independent flux equations to be written for both components. Since $z = 0$ and $z = 1$ are boundary conditions for the vapor and liquid, respectively, no flux was allowed at the ends of the column to ensure the total material balance was maintained. A height correction is described in the Supporting Information to account for no flux at the boundaries.

$$N_i^L = N_i^V = K_{g,i} a_e \left(P_i - P_i^*\right) \quad i = \mathrm{CO_2}, \mathrm{H_2O};\ 0 < z < 1 \tag{7.12}$$

H_2O transfer was assumed to only have gas film resistance, while CO_2 flux was limited by diffusion in both phases as well as reaction kinetics occurring in the liquid film. Wang (2015) has measured gas film mass transfer coefficients as a function of gas velocity in MP250X packing for an SO_2/H_2O/air system. The wetted area of the packing, a_e, is included in the experimental data and not explicitly calculated for the gas side mass transfer. This data was fit to a power law expression, shown in Figure 7.3. The power law expression was used to calculate the gas film resistances for the absorber packing in Equation 7.13. Binary gas diffusion coefficients were calculated with the Chapman-Enskog equation (Bird et al., 2002), and a mole-weighted average diffusion coefficient was used to

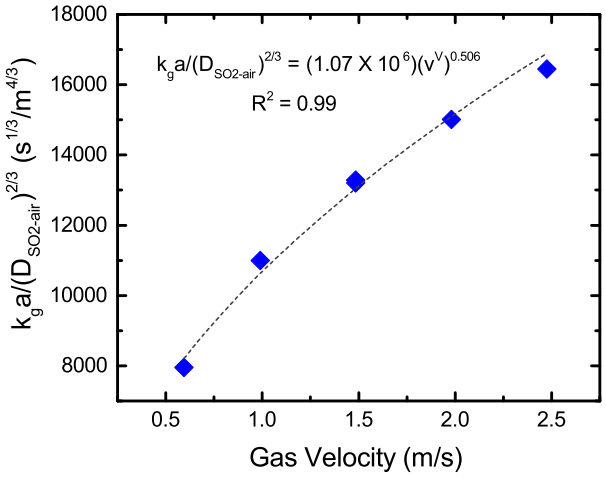

Figure 7.3: Experimentally measured gas film mass transfer coefficients of SO_2/air for MP250X structured packing at 25 °C with a liquid load ranging from 15–20 GPM/ft^2 reported by Wang (2015)

represent the diffusion of H_2O and CO_2 in the flue gas mixture (D_{i-flue}).

$$k_{g,i}a_e = \left(\frac{1.07 \cdot 10^6}{RT^V}\right)(v^V)^{0.506}\left(\frac{D_{i-flue}}{10^4}\right)^{0.667} \qquad i = \mathrm{CO_2}, \mathrm{H_2O} \tag{7.13}$$

The overall mass transfer coefficient for CO_2, $K_{g,CO2}$, was determined through a series resistance model (Equation 7.14). k_g' represents both the kinetic resistance from a finite reaction and the physical resistance from the diffusion of reactants and products to and from the interface. Dugas (2009) has tabulated experimental k_g' data for 5 molal PZ measured in a wetted wall column with laminar flow (Figure 7.4). k_g' in a packed column is expected to follow the same loading (α) dependence, which is related to the kinetics of the solvent. However, an adjustable parameter, c_{k_l}, was included to account for the discrepancy in liquid diffusive resistance (k_l) between the wetted wall column and the actual process (Equation 7.15). Note that there is not an observable temperature dependence on the experimental data. The wetted area of the packing for the liquid side mass transfer was

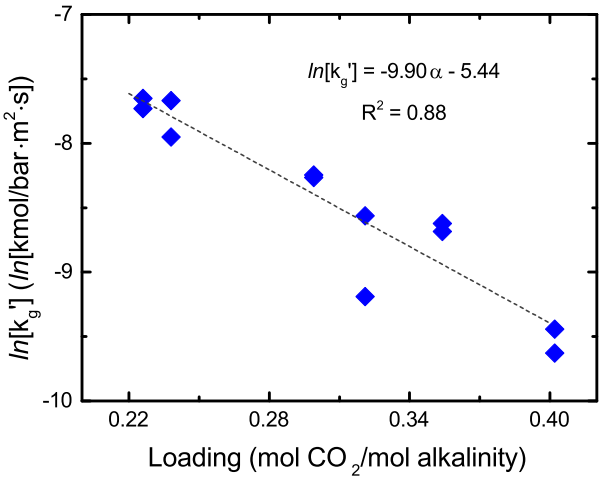

Figure 7.4: Experimentally measured liquid film mass transfer coefficients for 5 molal PZ ranging from 40–100 °C reported by Dugas (2009)

calculated according to Tsai et al. (2011) in Equation 7.16. One value for surface tension (σ) was assumed throughout the column based on the conditions at $z = 1$ to avoid calling a CAPE-OPEN physical property that requires the true liquid speciation.

$$\frac{1}{K_{g,CO2}a_e} = \frac{1}{k_{g,CO2}a_e} + \frac{1}{k'_{g,CO2}a_e} \tag{7.14}$$

$$\ln\left(k'_{g,CO2}\right) = c_{k_l} - 9.90\alpha \tag{7.15}$$

$$\frac{a_e}{a_p} = 1.34\left(\frac{\rho^L g^{1/3}\left|F^L\right|}{\sigma C^L L_p^{4/3}}\right)^{0.116} \tag{7.16}$$

Energy is transferred between the vapor and liquid through both the transfer of material and convection resulting from a temperature driving force, according to Equation 7.17. Like the material flux, no energy flux was allowed at $z = 0$ or $z = 1$. Energy transfer was assumed to have only gas film resistance because of the high thermal conductivity of liquids, so the gas/liquid interface temperature was the same as the bulk liquid

($T^I = T^L$).

$$N_H^L = N_H^V = \sum_i \left(N_i^V \bar{H}_i^V\right) + ha_e(T^V - T^L) \quad 0 < z < 1 \tag{7.17}$$

Partial molar enthalpy ($\bar{H}_i$) is defined in Equation 7.18, where H is an extensive enthalpy value. Aspen Properties® does not report $\bar{H}_i$, so it was calculated numerically by perturbing the value for n_i. In general, $\bar{H}_i^V \neq \bar{H}_i^L$; however, assuming no accumulation at the gas/liquid interface and $T^L = T^I$ forces this relation to be true. Vapor enthalpy is easier to calculate in Aspen Properties® because it does not require a flash calculation; therefore $\bar{H}_i^V$ was used in this work.

$$\bar{H}_i^V \equiv \left(\frac{\partial H^V}{\partial n_i}\right)_{T,P,n_{j\neq i}} \tag{7.18}$$

The convective heat transfer coefficient is related to $k_{g,H2O}$ through the Chilton-Colburn analogy in Equation 7.19. The vapor heat capacity (Cp^V) and thermal conductivity (κ^V) were calculated through the CAPE-OPEN interface.

$$ha_e = k_{g,H2O}a_e \cdot \left(\frac{RT^V}{10^2}\right) \cdot \left(C^V Cp^V\right)^{1/3} \cdot \left(\frac{10^4 \kappa^V}{D_{H2O-flue}}\right)^{2/3} \tag{7.19}$$

7.2.1.4 Packing Hydraulics

Liquid hold-up was predicted using the correlation from Billet and Schultes (1993) (Equation 7.20). To calculate viscosity (μ^L) using CAPE-OPEN, the liquid speciation must first be obtained through a flash calculation. The dependence of μ^L on the flash call created convergence issues, so the modified Weiland viscosity equation (Weiland et al., 1998) from Aspen Properties® was coded directly into the gPROMS® model (Equation 7.21). μ_{H2O}^L

was calculated using the temperature-dependent equation from DIPPR (2016).

$$\varepsilon^L = \left(\frac{12\mu^L a_p^2 |v^L|}{\rho^L g} \right)^{1/3} \tag{7.20}$$

$$\ln\left(\frac{\mu^L}{\mu^L_{H2O}} \right) = \left[w_{PZ} \left((420.5 w_{PZ} + 1349.3) T^L + (1.352 w_{PZ} + 4.224) \right) \right] \left(\frac{\alpha(9.458 w_{PZ} - 0.004515 T^L - 0.1584) + 1}{{T^L}^2} \right) \tag{7.21}$$

Pressure drop was neglected in the absorber column, resulting in a constant vapor velocity in the packing. Kvamsdal et al. (2009) and Enaasen Flø et al. (2015) allowed the vapor velocity to vary independently of the linear pressure drop profile they assumed, creating an inconsistent hydraulic relationship. In general, the gas velocity in the column depends on the pressure drop relation.

7.2.2 Water Wash and Liquid Distributor

While the primary purpose of the water wash is to remove volatile amine emissions, it is important from a process control perspective for maintaining the system water balance (Walters et al., 2016b). The water wash should be designed so that the mass flowrate of water entering the bottom of the absorber with the flue gas is equivalent to the mass flowrate of water exiting the top of the column with the scrubbed gas. PZ was assumed to be nonvolatile in this work, but the water wash was still included to ensure that the correct amount of water was returned to the absorber. Mellapak 350Y structured packing was used for the water wash section.

The water wash was modeled similar to the absorber, except $x_{PZ} = 0$ in the liquid phase and $N_{CO2} = 0$. In the true process, a small amount of PZ will be present in the

liquid from the removal of volatile amine as well as from the PZ in the stripper overhead condensate that is returned to the water wash recycle loop. Additionally, a small amount of CO_2 will transfer into the water as the result of physical solubility.

Walters et al. (2016b) proposed that the level of the water tank from the water recycle loop should be controlled using the circulation pump and the circulation flowrate should be set by the valve that controls the flow of water out of the water wash chimney tray. The water that is not extracted to the recycle loop overflows from the water wash chimney tray into the liquid distributor of the absorber. This overflow flowrate should be equal to the amount of water returned with the stripper condensate plus (or minus) the amount of water condensed (or evaporated) within the water wash packing in order to have no water accumulation or depletion in the system. The water tank and liquid distributor of the absorber were modeled as well-mixed stages, and the recycle cooler was assumed to be a perfect exchanger. The water wash distributor and water wash chimney tray inventories were assumed to be included as part of the water tank inventory.

7.2.3 Chimney Tray and Intercooler

The in-and-out intercooler between the top and bottom beds of packing draws-off solvent from the absorber chimney tray and cools it in a heat exchanger. The chimney tray was modeled as a well-mixed stage with one flow in and one flow out. The outlet flow to the intercooler was set by a level controller for the tray. An alternative configuration not explored here is to design the chimney tray to have a small overflow to the liquid re-distributor for the bottom section of packing, which would eliminate the need for a level controller. The inventory in the liquid re-distributor for the bottom section of packing was

assumed to be included as part of the chimney tray inventory. The intercooler was modeled as a perfect exchanger; dynamics associated with temperature control and cooling water disturbances were ignored.

7.2.4 Flowsheet Connectivity

Every stream within the flowsheet connecting different unit operations contains four pieces of information related to the movement of material and energy: mole flowrate, mole composition, mole specific enthalpy, and pressure. The first three components must be passed in the direction of the flow, while pressure may be passed in either direction. This formulation ensures that consistent information is passed between unit operations and the overall heat and material balance for the system is obeyed. Additionally, every stream carries information for model execution, including the names of the apparent species contained within the stream and the name of the eNRTL physical properties package. Two source blocks are included within the flowsheet for the lean amine entering the absorber distributor and the flue gas entering the bottom of the absorber packing. The species definition for liquid phase source block is different from that of vapor phase source block.

7.2.5 Model Characteristics

There are three distributed packed sections in the model: the absorber top and bottom beds and the water wash. Both absorber sections were discretized into 50 intervals and the water wash was discretized into 30 intervals. This is consistent with the discretization used in the high-order Aspen Plus® model. The open-loop gPROMS® model described here contains 500 differential variables and 21,282 algebraic variables. The large number

of algebraic variables is a result of the requirement by CAPE-OPEN to provide an input for all species defined in the thermodynamic package; many of these algebraic variables have a value of zero according to Equations 7.10b and 7.11b. The system was solved using the build-in gPROMS® differential and algebraic equation solver with a relative error tolerance of 10^{-5}. To aid the initialization calculation, initial guesses were provided for all variables that were determined by calls to the CAPE-OPEN package.

7.3 Model Validation

7.3.1 Design Case

The absorber column was designed to remove 90% of the CO_2 in the flue gas from a 550 MWe coal-fired power plant specified by Case 11 of NETL (2010). Table 7.3 lists the flue gas conditions for the 100% load case, assuming that the flue gas was passed through a direct contact cooler prior to entering the bottom bed of packing. This work assumes no change in flue gas composition for power plant part-load operation.

Table 7.3: Inlet flue gas conditions for 100% power plant load

	Value
F^V	560 kg/s
T^V	40 °C
y_{CO2}	14.78%
y_{N2}	75.42%
y_{O2}	2.66%
y_{H2O}	7.14%

Trimeric Corporation (2015) used the high-order Aspen Plus® model (Frailie, 2014) discussed in the previous section to design an amine scrubbing plant with an intercooled absorber for the NETL case study. The equipment sizes for the absorber design are listed in Table 7.4, and operating conditions are given in Table 7.5. Walters et al. (2016c) provided dimensions for the water tank and absorber distributor, as well as set points for the level (l) in the water tank and absorber chimney tray. These parameters are also listed in Table 7.4. While the medium-order model in this work incorporates the Aspen Properties® thermodynamic model, the high-order Aspen Plus® model simulates rigorous mass transfer with true component Maxwell-Stefan diffusion and explicit kinetic rates in the liquid film. There are no adjusted parameters in the Aspen Plus® model since a user-defined equation for k_l is included. The high-order model is also not restricted by assumptions of negligible bulk convection, infinite thermal conductivity in the liquid phase, and negligible liquid film resistance of H_2O.

Table 7.4: Equipment dimensions and level set points (sp) for the absorber (AB) packing, water wash (WW) packing, absorber chimney tray (CT), absorber distributor (DAB), and water tank (WT)

	Value
d_{AB}	18.5 m
d_{WT}	6.0 m
$L_{AB,btm}$	4.0 m
$L_{AB,top}$	4.0 m
L_{WW}	1.5 m
L_{DAB}	3 in
$l_{CT,sp}$	1.0 m
$l_{WT,sp}$	6.0 m

Table 7.5: Design operating conditions for the lean solvent, absorber (AB), water wash (WW), condensate return (CR), trim cooler (TC), intercooler (IC), and recycle cooler (RC)

	Value
F^L_{lean}	2420 kg/s
α_{lean}	0.22
$C^L_{PZ,lean}$	5 molal
P_{AB}	1.03 bar
F^L_{WW}	558 kg/s
F^L_{CR}	20.5 kg/s
T^L_{TC}	40.0 °C
T^L_{IC}	40.0 °C
T^L_{RC}	43.6 °C

While the high-order Aspen Plus® model is a good representation of the process, it is a two-dimensional spatial problem and requires an expert user for convergence. Additionally, Aspen Dynamics® does not support rate-based distillation simulations. It is therefore desirable to use the medium-order model developed in the previous section to evaluate the dynamics of the absorber temperature profile.

7.3.2 Validation Results

Prior to validating the medium-order gPROMS® model of this work with the high-order Aspen Plus® model, the adjustable parameter in Equation 7.15 must be determined. To do this, $k'_{g,CO2}a_e$ was back-calculated from the design case simulation results of the high-order model given the flux and driving force at each discrete section of the column. Figure 7.5 compares the high-order model value of $k'_{g,CO2}a_e$ to the value calculated using

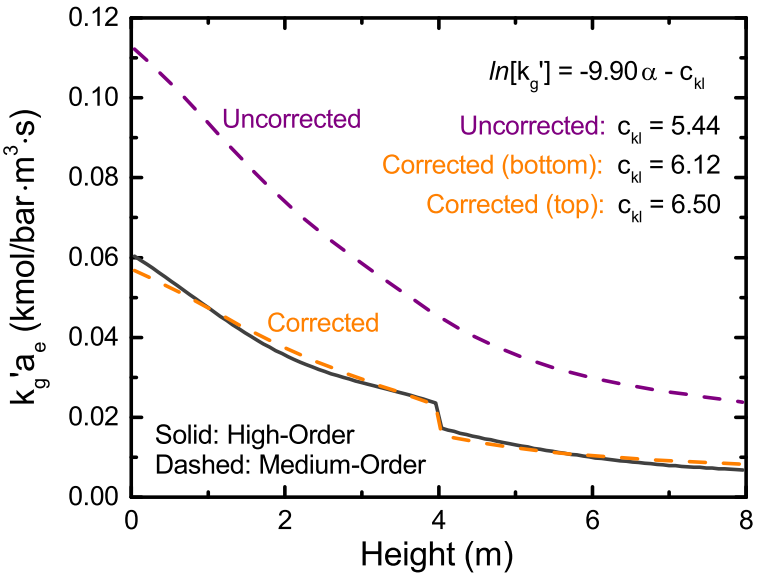

Figure 7.5: Comparison of uncorrected and corrected values of $k'_{g,CO2}$ from Equation 7.15 to values back-calculated from the high-order model results

the uncorrected regression equation from Figure 7.4. The discontinuity in the high-order profile occurs at the location of the solvent intercooler. c_{k_l} was calculated for each bed of packing using least squares error, and the adjusted value is also included in Figure 7.5. If the objective of the medium-order model was to match an existing commercial process, a parameter estimation is required to identify c_{k_l}.

The medium-order model was compared to the high-order Aspen Plus® model for 100–85% flue gas load. In each off-design condition, the lean composition, flue gas composition, and liquid to gas (L/G) ratio were kept constant at the values listed in Tables 7.3 and 7.5. The water wash recycle flowrate was adjusted according to the off-design values reported in Walters et al. (2016c). The validation results are presented in Figure 7.6. The figure shows that the rich and absorber-middle loadings are in good agreement for the high-

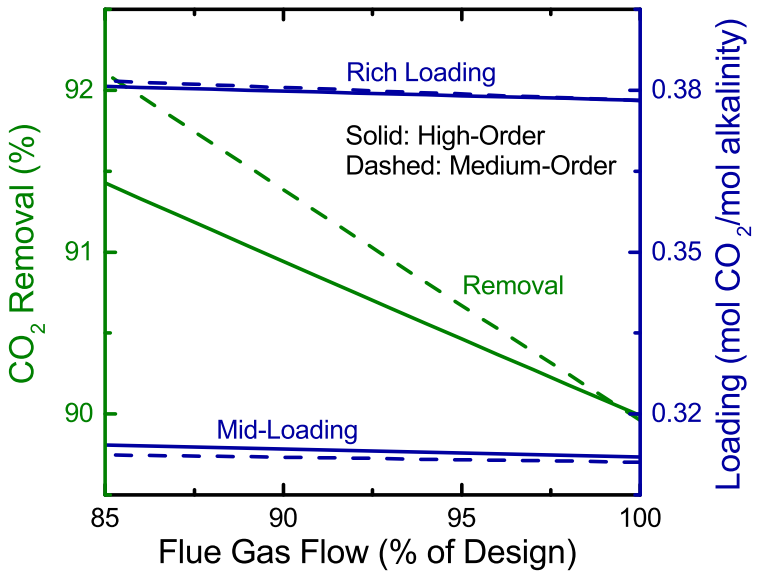

Figure 7.6: Off-design steady state simulation results of the high-order Aspen Plus® model (solid) compared to the medium-order gPROMS® model (dashed) for the Trimeric design, with a constant α_{lean} of 0.22, lean concentration of 5 molal PZ, and L/G ratio of 4.32

and medium-order models. At 85% load, the deviation between the predicted removal rate for the two models is less than 0.7%.

The temperature profile is an important indicator of absorber column performance. The temperature profiles for 100% and 85% flue gas load are given in Figure 7.7. The medium-order model profile is slightly sharper and to the left, meaning that the more mass transfer is occurring at the rich end of each bed in the medium-order model than in the high-order model. However, there is generally good agreement between the temperature profiles of the two models, as summarized in Table 7.6.

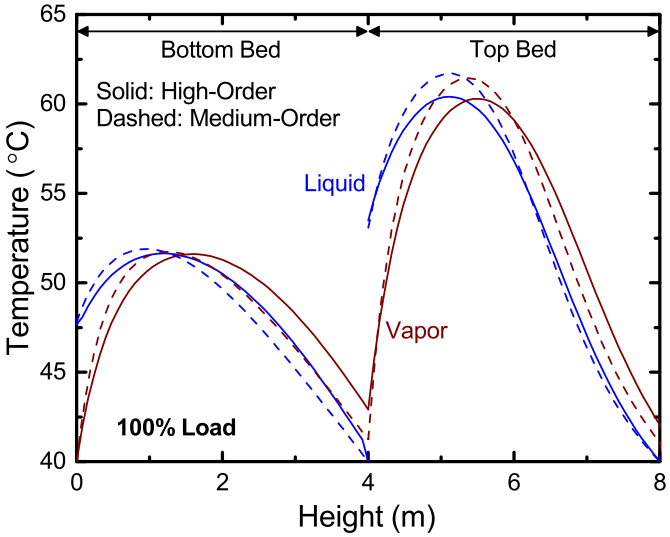

(a)

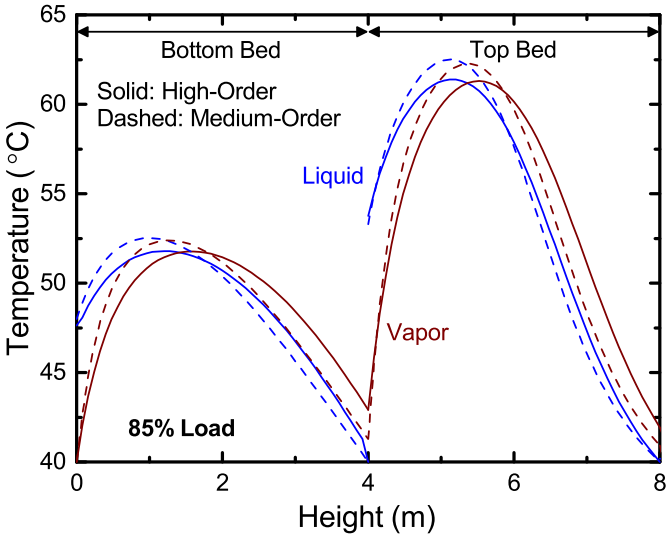

(b)

Figure 7.7: Absorber temperature profile of the liquid (blue) and vapor (red) phases at 100% (a) and 85% (b) flue gas load predicted by the high-order Aspen Plus® model (solid) and medium-order gPROMS® model (dashed) for the Trimeric design, with a constant α_{lean} of 0.22, lean concentration of 5 molal PZ, and L/G ratio of 4.32

Table 7.6: Maximum temperature (T_{max}) and temperature bulge location comparison for high- and medium-order models

		100% Load			85% Load		
		High	Medium	Δ	High	Medium	Δ
Top Bed	T^L_{max} (°C)	60.4	61.7	1.3	61.4	62.5	1.1
	L (m)	5.12	5.14	0.02	5.12	5.14	0.02
	T^V_{max} (°C)	60.3	61.4	1.1	61.3	62.3	1.0
	L (m)	5.52	5.39	0.13	5.52	5.39	0.13
Btm Bed	T^L_{max} (°C)	51.6	51.9	0.3	51.8	52.5	0.7
	L (m)	1.20	0.98	0.22	1.20	0.98	0.22
	T^V_{max} (°C)	51.6	51.7	0.1	51.8	52.4	0.6
	L (m)	1.60	1.22	0.38	1.60	1.22	0.38

7.4 Absorber Column Control

Several works have evaluated process control strategies for the simple absorber column. Ziaii-Fashami (2012) and Nittaya et al. (2014) have attempted to control the CO_2 removal rate with the solvent circulation rate. However, Walters et al. (2014) performed a time scale analysis to show that controlling removal with the large internal flow will likely lead to poor controller performance. Ziaii-Fashami (2012) concluded that this strategy resulted in oscillations of important process variables such as stripper pressure. While Nittaya et al. (2014) showed that this control structure was able to quickly reject disturbances and track set point changes, their model ignored changes in stripper pressure and thus missed important lean loading dynamics that will impact the ability to tightly control removal.

Lawal et al. (2010), Ceccarelli et al. (2014), and Walters et al. (2016b) have recommended maintaining a constant liquid to gas (L/G) ratio in the absorber, defined as the ratio of liquid mass flow entering the top of the column to gas mass flow entering the bottom of the column. This method maintains consistent operation of the absorber column, producing rich solvent at a nearly constant loading with varying flue gas flowrates. While this strategy has been shown to result in favorable process dynamics, it is unlikely that a reliable gas flow measurement will be available online. This section identifies a surrogate process variable that can be used in place of the flue gas flow rate measurement and develops a process control strategy that maintains near-constant L/G ratio.

7.4.1 Controlled Variable Identification

Figure 7.7 and Table 7.6 demonstrate that while the magnitude of the maximum observed temperature in each bed of packing varied slightly as the amount of CO_2 absorbed was decreased, the shape of the temperature profile was nearly identical across a range of flue gas loads when constant L/G was maintained. This shows that the shape of the temperature profile can be an indicator of L/G ratio. By identifying a temperature within the absorber column profile that is sensitive to changes of the profile shape, a feedback controller with the lean solvent flowrate as the manipulated variable (MV) can be used to control this temperature at the desired set point in order to maintain constant L/G ratio. Figure 7.7 shows that the largest continuous, monotonic change in temperature occurs in the liquid phase between a packing height of 5.1–8 m. The midpoint temperature of this range occurs at a packing height of 6.5 m ($T^{L}_{L=6.5}$) and was selected as the controlled variable (CV) in this work. Figure 7.8 plots the off-design steady state value of $T^{L}_{L=6.5}$ when constant L/G

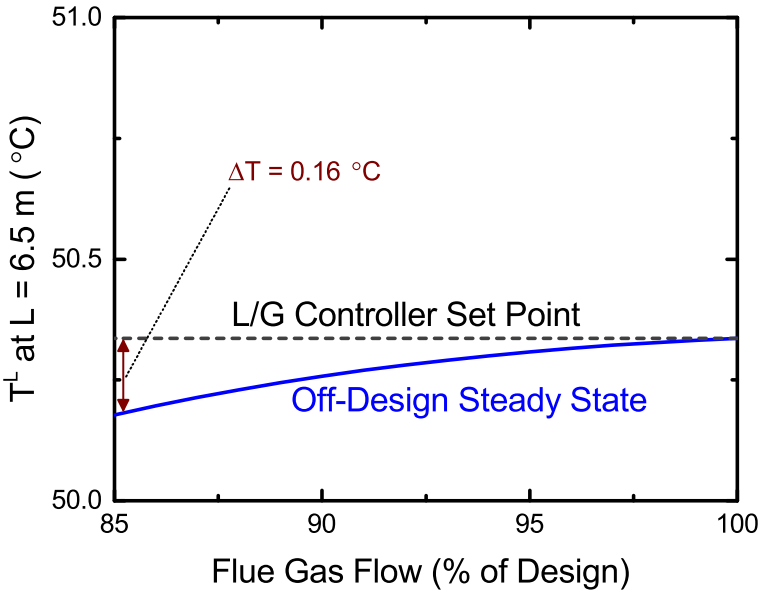

Figure 7.8: Off-design steady state simulation results for $T^{L}_{L=6.5}$ predicted by the medium-order gPROMS® model for the Trimeric design, with a constant α_{lean} of 0.22, lean concentration of 5 molal PZ, and L/G ratio of 4.32

ratio was maintained, showing that it changed by less than 0.2 °C as the flue gas flowrate was decreased from 100% to 85%.

A 5% step change in lean flowrate was introduced at time zero, and the open-loop response of $T^{L}_{L=6.5}$ is plotted in Figure 7.9. The response takes the form of a first-order plus time-delay (FOPTD) model. A temperature change of nearly 8 °C resulted from the 5% change in solvent rate, further demonstrating that $T^{L}_{L=6.5}$ is a good indicator of deviations in L/G ratio.

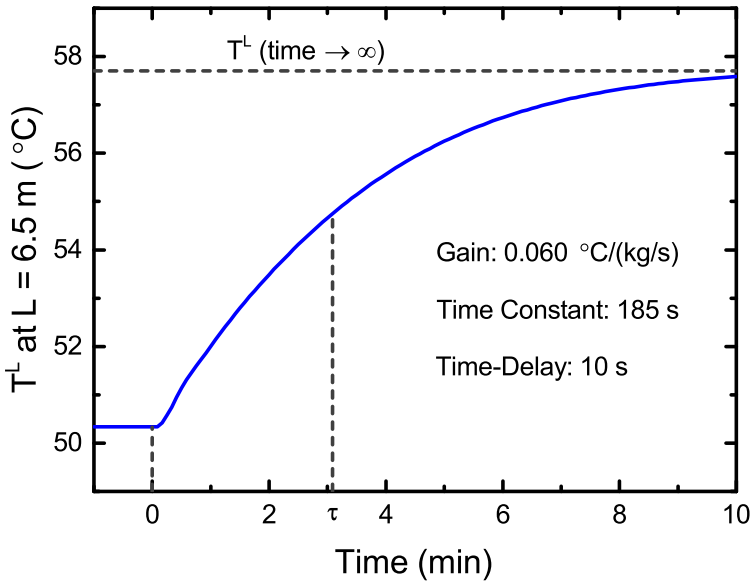

Figure 7.9: Open-loop response of $T^L_{L=6.5}$ to a 5% decrease in F^L_{lean} predicted by the medium-order gPROMS® model for the Trimeric design, with a constant α_{lean} of 0.22, lean concentration of 5 molal PZ, and design flue gas conditions

7.4.2 L/G Control Performance

A PI controller that manipulates the lean solvent flowrate to control $T^L_{L=6.5}$ at its design set point was implemented to maintain constant L/G in the presence of flue gas flowrate disturbances. Standard lambda tuning (Seborg et al., 2011) was used based on the FOPTD parameters from Figure 7.9 with $\lambda = 3\theta_d$, where θ_d is the time delay. Tuning parameters for the water tank and chimney tray level controllers were provided by Walters et al. (2016b) and used in this work. The water wash circulation flowrate remained constant when evaluating L/G control performance.

A typical ramp rate for a supercritical coal-fired power plant is approximately 2% per min (Peltier, 2005). A 2% per min decrease in flue gas flowrate from 100–80% load was selected as the disturbance to test the proposed L/G control strategy. This should be consistent with the typical power plant ramp rate, assuming that the flue gas flowrate is proportional to the load of the coal-fired boiler. Figure 7.10 plots the values for the disturbance, MV, CV, and L/G ratio over time. The results show satisfactory performance with this strategy, with the L/G ratio maintained within 0.9% of the design L/G ratio of 4.32 throughout the duration of the disturbance.

7.4.3 L/G Control with other Process Disturbances

Disturbances in other process variables besides the flue gas flowrate may also affect the absorber temperature profile, including changes in α_{lean}, T^L_{IC}, and y_{CO2} in the flue gas. Figure 7.11 shows that when step changes was made for each of these variables with constant lean flowrate, a FOPTD response of $T^L_{L=6.5}$ was observed. This demonstrates that the desired L/G ratio will not be maintained if temperature control is active in the presence

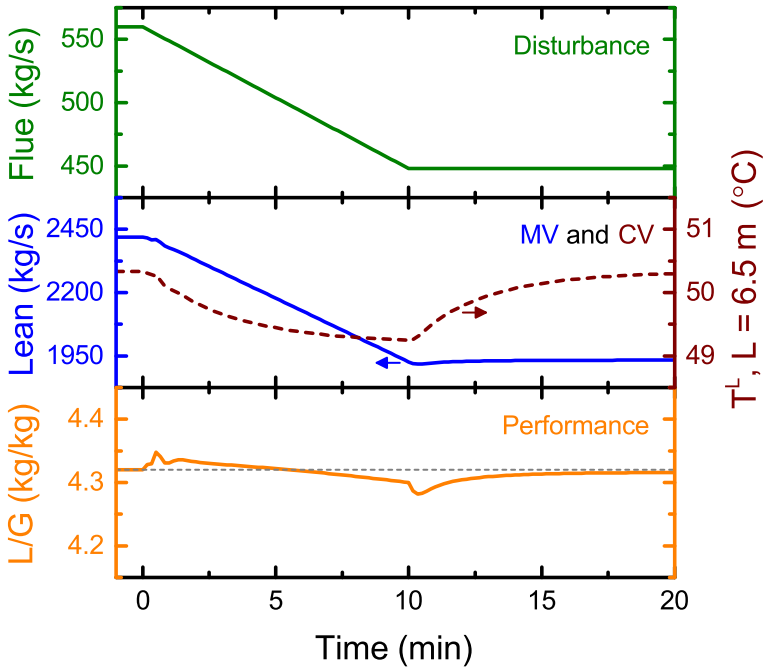

Figure 7.10: Closed-loop results predicted by the medium-order gPROMS® model for the Trimeric design, with a constant α_{lean} of 0.22 and lean concentration of 5 molal PZ

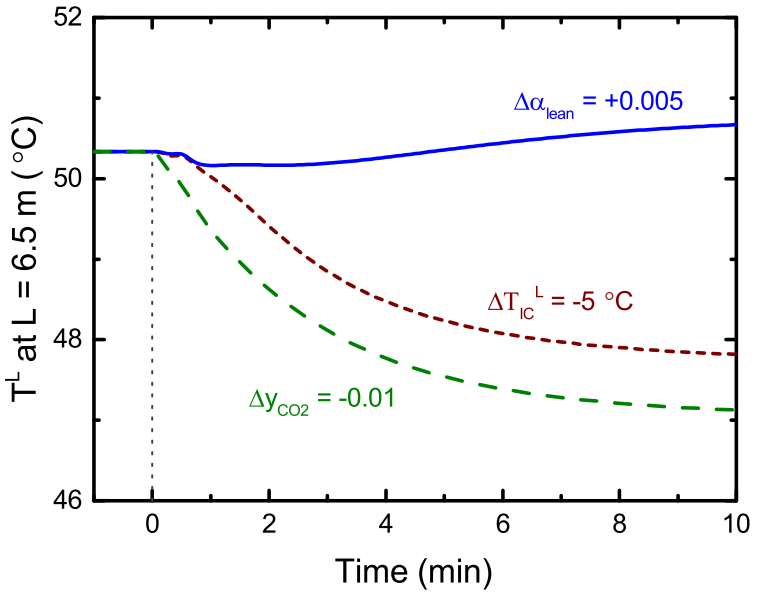

Figure 7.11: Open-loop response of $T^L_{L=6.5}$ to disturbances in α_{lean}, T^L_{IC}, and y_{CO2} predicted by the medium-order gPROMS® model for the Trimeric design, with a constant lean concentration of 5 molal PZ and design flowrates for the flue gas and lean solvent

of disturbances that cause deviations in the shape and location of the column temperature profile.

Feedforward control that adjusts the temperature controller set point was used to compensate for measured disturbances. Figure 7.12 presents a block diagram for the proposed feedforward structure. By determining a FOPTD transfer function model for each measured disturbance (G_d) from the open-loop tests in Figure 7.11, the temperature controller set point can be updated online so the desired L/G ratio will be maintained.

The feedforward scheme was demonstrated for a disturbance in T^L_{IC}. Cooling water temperature or availability will likely vary as a result of changing ambient conditions, and plant operators may want to take advantage of operating the absorber at lower temperatures

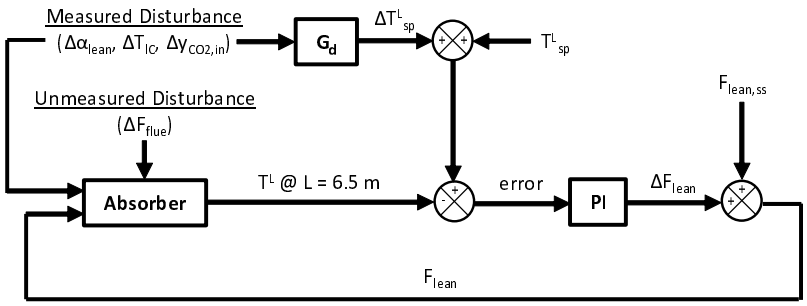

Figure 7.12: Block diagram for absorber temperature control with feedforward action

based on these changes. In Figure 7.13, a step change in T_{IC} was introduced with the feedforward controller active, maintaining a constant flue gas flowrate. To the extent that the true response from Figure 7.11 differs from the FOPTD model, there will be slight variations in the lean flowrate (and hence L/G ratio). However, the deviation in L/G ratio was less than 0.6% in this case, showing that the effects of disturbances can be mitigated through feedforward control assuming that the disturbances are measured online.

7.5 Conclusions

A medium-order dynamic absorber model was developed in gPROMS® and is in good agreement a high-order Aspen Plus® steady state model. The CO_2 removal rate predicted by the two models differed by less than 0.7% at 85% flue gas load and the maximum predicted values of the absorber temperature profile for the design case were within 1.2 °C. Unlike other medium-order models in the literature that model a simple absorber with MEA solvent and use semi-empirical thermodynamics, the work presented here simulated an intercooled absorber with PZ solvent and contained a rigorous eNRTL thermodynamic model. Controlling the L/G ratio in the absorber should result in favorable process dynam-

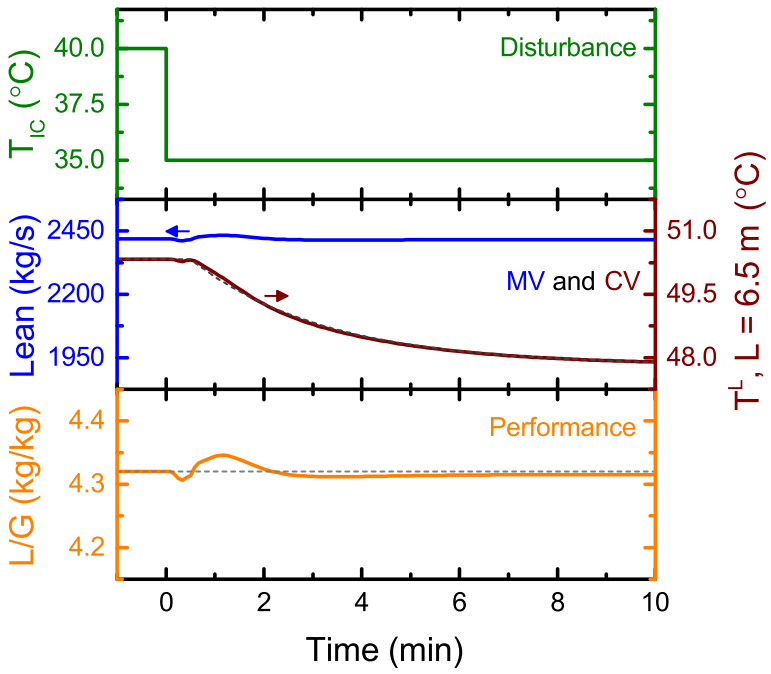

Figure 7.13: Feedforward results with a disturbance in T_{IC}^{L} predicted by the medium-order gPROMS® model for the Trimeric design, with constant lean solvent and flue gas conditions

ics of the amine scrubbing process, but it is unlikely that a reliable flue gas flowrate will be available online. The liquid temperature that occurs at an absorber packing height of 6.5 m was shown to be an effective indicator of the L/G ratio. A controller that manipulated the solvent flowrate to control this temperature resulted in less than a 0.9% change at all times when the flue gas rate was ramped from 100–80%. Incorporating feedforward control can compensate for the effect of measured disturbances on the absorber temperature profile and allow for the desired L/G ratio to be maintained.

7.6 Notation

Greek

α	loading (mol CO_2/mol alkalinity)
ε	liquid hold-up (m^3/m^3)
κ	thermal conductivity (MW/m·K)
μ	viscosity (Pa·s)
ρ	mass density (kg/m^3)
σ	surface tension (N/m)

Roman

a_e	effective wetted area of packing (m^2/m^3)

a_p	specific area of packing (m^2/m^3)
C	concentration ($kmol/m^3$)
Cp	specific heat capacity (MJ/kmol·K)
D	diffusion coefficient (cm^2/s)
d	diameter (m)
F	molar or energy flowrate (kmol/s or MW)
g	acceleration of gravity (m/s^2)
$\hat{H}$	specific enthalpy (MJ/kmol)
H	enthalpy (MJ)
h	convective heat transfer coefficient ($MW/m^2 \cdot K$)
$\bar{H}$	partial molar enthalpy (MJ/kmol)
K_g	overall mass transfer coefficient ($kmol/bar \cdot m^2 \cdot s$)
k_g	gas side mass transfer coefficient ($kmol/bar \cdot m^2 \cdot s$)
k'_g	liquid side mass transfer coefficient ($kmol/bar \cdot m^2 \cdot s$)
L	height (m)
L_p	wetted perimeter (m)
N	material or energy flux ($kmol/m^3 \cdot s$ or MW/m^3)
n	molar amount (kmol)
P	pressure (bar)

P^*	equilibrium pressure (bar)
R	gas constant (J/mol·K)
S	cross sectional area (m^2)
T	temperature (K)
t	time (s)
U	specific internal energy (MJ/m^3)
v	superficial velocity (m/s)
vf	vapor fraction (kmol/kmol)
$\hat{V}$	specific volume (m^3/kmol)
w	mass fraction (kg/kg)
x	liquid mole fraction (kmol/kmol)
y	vapor mole fraction (kmol/kmol)
z	normalized axial domain (m/m)

Subscripts

CO	CAPE-OPEN
H	energy
i	component

Superscripts

I	interface

L	liquid
V	vapor

Chapter 8

Model Predictive Control of CO_2 Removal

8.1 Introduction

This chapter proposes model predictive control (MPC) as the supervisory level controller for the amine scrubbing system. MPC is commonly used in the process industries (Qin and Badgwell, 2003) and takes advantage of an explicit process model to predict future plant behavior. In MPC, an optimal control problem is solved over a finite horizon subject to process constraints, and the controller implements the first move of the optimal control solution (Mayne et al., 2000; Seborg et al., 2011). This process is repeated at every sampling time to account for feedback from the measured output variables. The goal of this chapter is to determine the improvement in closed-loop performance that results from superimposing an MPC controller on the regulatory control layer developed in Chapter 5.

8.1.1 Literature Review of MPC for Amine Scrubbing

Several researchers have demonstrated various MPC strategies for amine scrubbing systems using a simple absorber and reboiled stripper. These works are described in the following paragraphs, and the proposed controlled variables (CVs) and manipulated variables (MVs) are summarized in Table 8.1. Åkesson et al. (2012) used nonlinear MPC (NMPC) as a strategy to track a CO_2 removal (Rem) reference trajectory (where Rem was defined as the flowrate ratio of CO_2 exiting the stripper to CO_2 entering the absorber). Two scenarios

were considered: (1) control Rem by manipulating the reboiler heat duty (Q_{reb}) only and (2) control Rem by manipulating both Q_{reb} and solvent circulation rate (F_s). The stripper pressure controller set point ($P_{ST,sp}$) was constant in both scenarios. The first scenario only contained a model of a reboiled stripper and assumed constant rich conditions from the absorber, which ignores important process dynamics from solvent recycle. The desired set point was not achieved in this scenario because of constraints on the reboiler pressure. A two-stage equilibrium absorber model was included for the second scenario, and the Rem set point was achieved through significant adjustment in F_s.

Arce et al. (2012) examined the control of a detailed thermosiphon reboiler model. Linear MPC was responsible for tracking the set points of the reboiler level (l_{reb}) and CO_2 stripping rate (F_{CO2}) by simultaneously manipulating F_s and Q_{reb}. F_{CO2} was defined as the liquid flowrate of CO_2 in to the reboiler minus the liquid rate out. At steady state, this value is equivalent to the CO_2 delivery rate to the sequestration facility. The reference trajectories were determined through an economic optimization. A separate MPC problem regulated the stripping pressure (P_{ST}) to a constant set point by manipulating the molar flowrate of the stripper gas (F_{ST}^V). While the closed-loop results for this strategy showed good performance with disturbances in rich loading (α_{rich}) and lean flowrate, the simulation did not take into account feedback from the absorber. Additionally, reboiler temperature (T_{reb}) was allowed to fluctuate, which will likely result in decreased energy performance.

Sahraei and Ricardez-Sandoval (2014) implemented linear MPC on an equilibrium-stage Aspen HYSYS® model for a full amine scrubbing plant. He et al. (2016) expanded on this work to include a simultaneous scheduling and control framework. The centralized MPC problem considered the following CVs: Rem, CO_2 product composition ($y_{CO2,ST}$),

T_{reb}, and levels for the absorber sump, reboiler, and condenser (l_{sump}, l_{reb}, and l_{cond}, respectively). The condenser temperature (T_{cond}) is likely a more appropriate CV than $y_{CO2,ST}$, which was used as a CV in that work. The corresponding MVs were: F_s, Q_{reb}, condenser duty (Q_{cond}), and flowrates associated with valves on the lean stream, rich stream, and stripper reflux. The level control objectives and their corresponding flowrates were not listed in Table 8.1 for conciseness, even though they were included in the MPC formulation. It is unclear how P_{ST} and F_{CO2} were determined in this work, although the results suggest that F_{CO2} was calculated by Aspen HYSYS® to maintain P_{ST} at a constant value.

The thermodynamic model for MEA/CO_2/H_2O developed by Plaza (2011) is used here to demonstrate the importance of P_{ST} as a process variable. Figure 8.1 shows the equilibrium dependence of α_{lean} on pressure at the reboiler operating temperature specified by Sahraei and Ricardez-Sandoval. Small deviations in pressure will significantly impact α_{lean}, and deviations in α_{lean} will in turn impose a disturbance on absorber operation by changing the mass transfer driving force within the column. Given that the control of a critical process variable appears to have been ignored in the work of Sahraei and Ricardez-Sandoval, their results showing good closed-loop responses to disturbances and set point tracking may be artificially favorable.

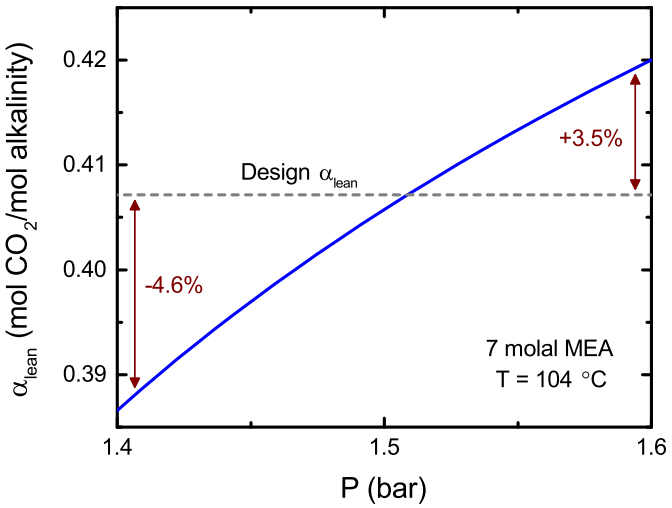

Figure 8.1: VLE curve for 7 m MEA at constant temperature demonstrating the relationship between pressure and α

Luu et al. (2015) fit a linear model to a medium-order model of an amine scrubbing plant. The linear model was then used for both the plant and the MPC problem, so there was no plant-model mismatch. The CVs were identified as Rem, T_{reb}, and energy performance (EP). Energy performance was defined according to Equation 8.1:

$$EP = \frac{100 Q_{reb}}{y_{CO2,in} F_{in} Rem} \tag{8.1}$$

where $y_{CO2,in}$ is the CO_2 composition in the inlet flue gas and F_{in} is the flue gas flowrate. Equation 8.1 is not a good objective function to quantify energy performance because it does not take in to account compression work or the equivalent work of steam (Lin and Rochelle, 2016). F_s and Q_{reb} were selected as the MVs. P_{ST} appears to have been kept constant during the linear model identification by varying F_{CO2}. Similar to Sahraei and Ricardez-Sandoval (2014), this work did not adequately account for stripper operation, and therefore the results showing favorable closed-loop performance are questionable.

Mehleri et al. (2015) identified a linear model from the rigorous gCCS® model created by Process Systems Enterprise and performed a closed-loop MPC simulation with no plant-model mismatch. The CVs were Rem, T_{reb}, T_{cond}, l_{sump}, and l_{reb} and the MVs were F_s, Q_{reb}, and the valve positions for the rich solvent, lean solvent, and condenser cooling water. Variables associated with levels and cooling water were excluded from Table 8.1. Once again, P_{ST} dynamics were ignored, which will result in unrealistic system performance.

Zhang et al. (2016) developed an amine scrubbing model in Aspen Dynamics®, using Murphree efficiency to predict mass transfer in the absorber. Linear models for the CVs Rem and T_{reb} were identified as a function of the MVs F_s and Q_{reb} and the disturbance variables F_{in} and $y_{CO2,in}$ for implementation in MPC. This configuration effectively controls P_{ST} and T_{reb} (and hence α_{lean}) and manipulates F_s to control the capture rate. Because MPC uses the identified linear model to predict future plant behavior, there were no significant oscillations like what was observed by Ziaii-Fashami (2012) when using this strategy with PID control alone. Even with MPC, a large solvent surge tank will be required due to excessive flowrate variations to ensure stable operation when using the solvent circulation rate to respond to disturbances in absorber performance.

Table 8.1: Previously published MPC strategies for amine scrubbing

	CV(s)	MV(s)
Åkesson et al. (2012)	Rem	F_s, Q_{reb}
Arce et al. (2012)	F_{CO2}, l_{reb}, P_{ST}	F_s, Q_{reb}, F_{ST}^V
Sahraei and Ricardez-Sandoval (2014)	Rem, $y_{CO2,ST}$, T_{reb}	F_s, Q_{reb}, Q_{cond}
Luu et al. (2015)	Rem, T_{reb}, EP	F_s, Q_{reb}
Mehleri et al. (2015)	Rem, T_{reb}	F_s, Q_{reb}
Zhang et al. (2016)	Rem, T_{reb}	F_s, Q_{reb}
This Work	Rem	$P_{ST,sp}$

Despite the relatively large body of work on MPC for post-combustion amine scrubbing in the literature, several critical process control issues have not been adequately addressed. Stripper pressure (P_{ST}) is an important process variable because it is related to α_{lean} and F_{CO2}, as demonstrated in Figure 8.1 for an MEA system. However, P_{ST} has been ignored in several previous studies. Only Arce et al. (2012) included P_{ST} in the MPC formulation, and Zhang et al. (2016) and Åkesson et al. (2012) had regulatory PID controllers to maintain $P_{ST,sp}$. The remaining works either arbitrarily set P_{ST} to a constant value (Sahraei and Ricardez-Sandoval, 2014) or identified a linear model that did not include the effects of P_{ST} (Luu et al., 2015; Mehleri et al., 2015). The interaction between solvent regeneration and the power plant turbines has also largely been ignored. Only Zhang et al. (2016) included a steam turbine model when evaluating closed-loop performance. Additionally, none of the previous researchers have considered control of systems with advanced solvents or intensified process configurations.

8.1.2 Motivation and Scope

As shown in Table 8.1, all previous MPC designs had F_s as an MV and Rem (or a surrogate for Rem) as a CV. However, Chapter 4 used a time scale analysis to show that controlling the small deviations in CO_2 flux within the absorber column using the small CO_2 product flow should result in better closed-loop performance than using the large solvent circulation rate as the MV. Furthermore, Chapter 5 discussed the implications of manipulating F_s for the required solvent residence time in the system and Chapter 7 showed that maintaining a constant L/G ratio kept the absorber column profiles approximately constant at off-design conditions. A simplistic view of the strategies from Table 8.1 is that α_{lean} was kept constant and F_s was manipulated to control Rem. This chapter proposes an alternative formulation where L/G in the absorber is kept constant and F_{CO2} is manipulated to control Rem. The objectives of this chapter are to: (1) develop a linear MPC controller to regulate the CO_2 removal set point, (2) compare the performance of MPC to PI control alone, and (3) demonstrate removal control with MPC for a load-following power plant.

8.2 CO_2 Removal Controller Development

Case 3 of Chapter 5 demonstrated that controlling Rem directly with F_{CO2} through regulatory feedback control resulted in undesirable closed-loop dynamics in response to a decrease in boiler load (see Figure 5.7). When P_{ST} was controlled instead of Rem in Case 4 of Chapter 5, a fast and stable response was observed (see Figure 5.8), but there was no guarantee that the desired set point for Rem would be achieved. To maintain the favorable performance of Case 4 but also control the CO_2 removal rate from the flue gas, MPC was superimposed on the Case 4 regulatory control strategy. Rem was the CV and the set point

of the pressure PI controller was the MV for the MPC problem, as shown in Figure 8.2. The P&ID for this configuration is given in Figure 8.3.

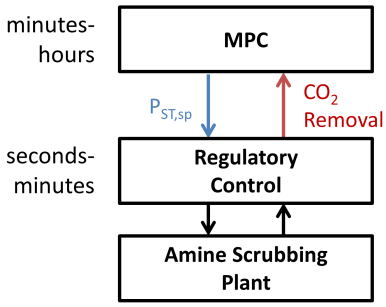

Figure 8.2: Hierarchical strategy for controlling CO_2 removal from flue gas (Seborg et al., 2011)

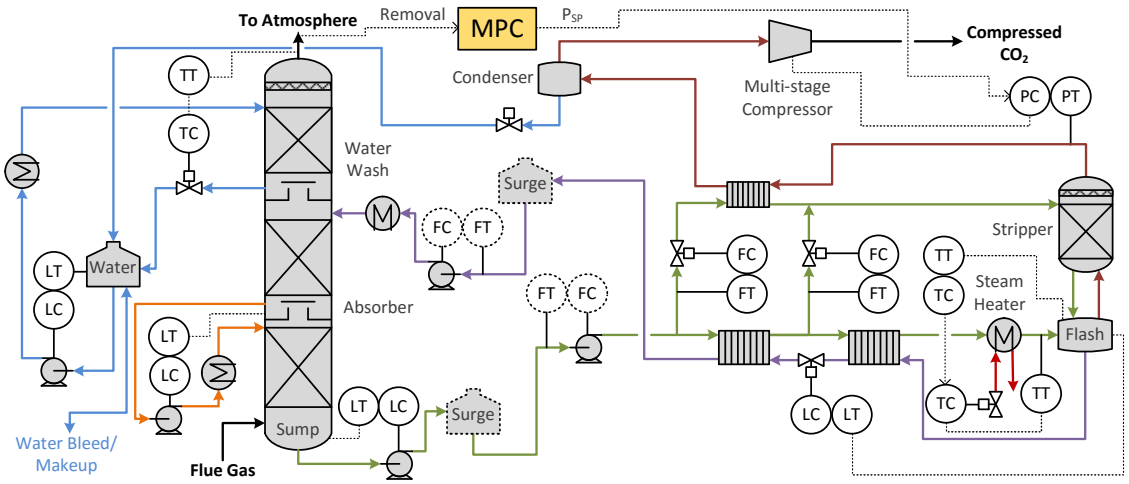

Figure 8.3: Control strategy from Case 4 of Chapter 5 (as well as temperature cascade from Chapter 7) with supervisory MPC controller determining the set point for the pressure control PI loop

8.2.1 System Identification

In this section, a single-input, single-output (SISO) linear transfer function model is identified to predict CO_2 removal in the absorber as a function of the stripper pressure controller set point. Step changes were made in $P_{ST,sp}$ for the low-order model in the configuration of Figure 8.3, using the same P and PI controller tuning as reported in Chapter 5. Figure 8.4 plots the simulation results from this system identification experiment. The Rem gain was asymmetrical for positive and negative step changes because the steam valve was saturated when $P_{ST,sp}$ dropped below its design condition.

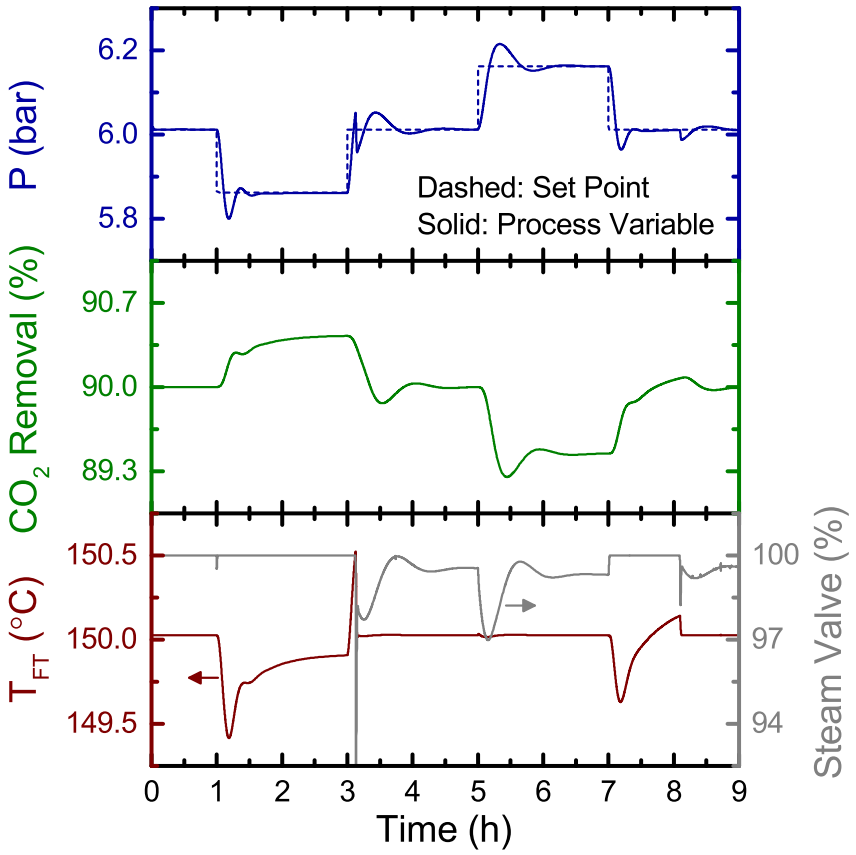

Figure 8.4: Simulation results using the flowsheet from Case 4 of Chapter 5 in response to step changes in $P_{ST,sp}$

The MATLAB® System Identification Toolbox™ was used to identify a first-order transfer function model using the data from Figure 8.4. The transfer function response is compared to the low-order dynamic model in Figure 8.5. While the overshoot from the pressure control action was not captured by the first-order model, the general relation between $P_{ST,sp}$ and Rem was adequately predicted with a 72% fit. The identified transfer

function model used for MPC is given in Equation 8.2.

$$\frac{\Delta Rem}{\Delta P_{ST,sp}} = \frac{-3.3147}{760.5 \cdot s + 1} [\%/bar] \tag{8.2}$$

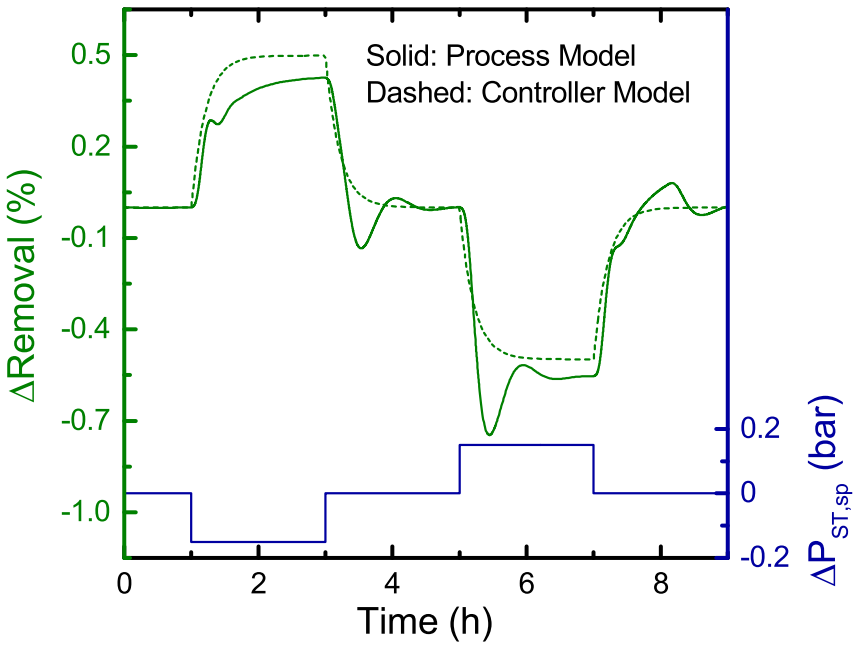

Figure 8.5: Comparison of Rem predicted by the low-order dynamic process model (solid) and first-order transfer function (dashed)

Step response models are commonly used in MPC implementation because they can capture dynamic behavior that is missed by simple transfer function models such as Equation 8.2 (Seborg et al., 2011). A step response model, shown in Equation 8.3, typically contains between 30 and 120 step response coefficients (S_i) depending on the settling time (t_s):

$$y(k+1) = y_0 + \sum_{i=1}^{N} S_i \Delta u(k-i+1) \tag{8.3}$$

where y is the output, u is the input, N is the model horizon, and k is the sampling instant. A step response model was not used in this work because of the asymmetric behavior of CO_2 removal in response to positive and negative changes in the pressure controller set point. Two step response models were fit from the simulation results in Figure 8.4: one using the negative step change at $t = 1h$ and another using the positive step change that occurred at $t = 5h$. The step response models assume a sampling time (Δt) of 1 min and a model horizon of 70 min. To demonstrate the issue with using a step response model, Figure 8.6 expands upon Figure 8.5 by plotting the prediction from the positive and negative step response models. Because the transfer function model represents a reasonable average for both negative and positive step changes in $P_{ST,sp}$, it was used as the model for MPC.

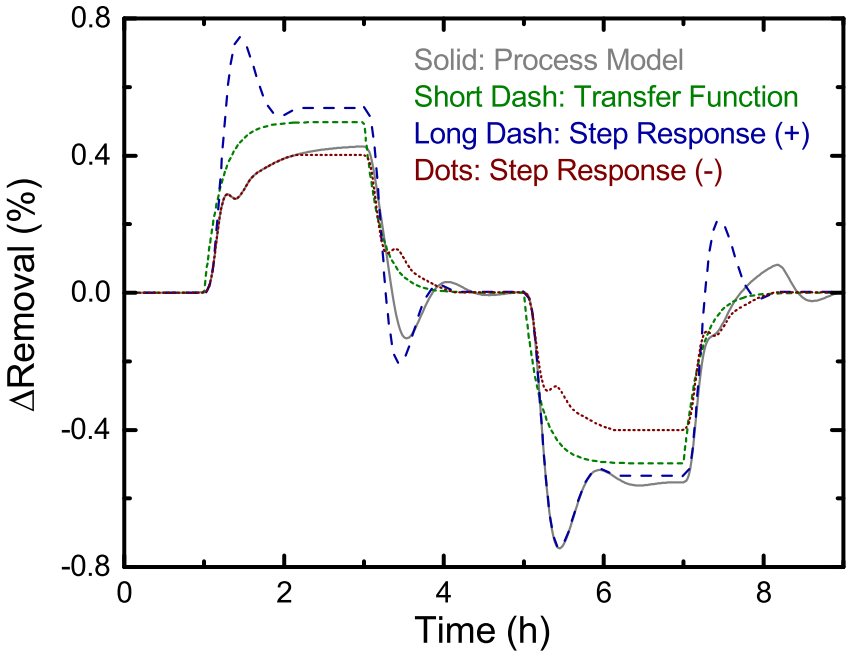

Figure 8.6: The asymmetry of Rem predicted by the low-order dynamic process model (solid) leads to poor performance of step response models identified using a positive step change in $P_{ST,sp}$ (long dash) and a negative step change in $P_{ST,sp}$ (dots), making the first-order transfer function (dashed) a reasonable model to use in the MPC problem

8.2.2 Linear MPC Controller Formulation

The SISO MPC problem takes the form of Equation 8.4 (Seborg et al., 2011):

$$\begin{aligned} \min_{\Delta\hat{\boldsymbol{U}}(k)} \quad & J = \hat{\boldsymbol{E}}(k+1)^T \boldsymbol{Q} \hat{\boldsymbol{E}}(k+1) + \Delta\hat{\boldsymbol{U}}(k)^T \boldsymbol{R} \Delta\hat{\boldsymbol{U}}(k) + Q_p \left(\hat{E}(P)\right)^2 \\ \text{subject to:} \quad & \hat{\boldsymbol{E}}(k+1) = f(E(k), \Delta\hat{\boldsymbol{U}}(k)) \\ & \Delta U_{lb} \leq \Delta\hat{\boldsymbol{U}}(k) \leq \Delta U_{ub} \end{aligned} \tag{8.4}$$

where $E(k)$ is the error at the current sampling time k, $\hat{\boldsymbol{E}}(k+1)$ is the predicted error vector, $\Delta\hat{\boldsymbol{U}}(k)$ is a vector of control moves, $\boldsymbol{Q}$ is a $P \times P$ positive definite diagonal output

weighting matrix, $\boldsymbol{R}$ is an $M \times M$ positive semi-definite diagonal input weighting matrix, Q_p is the terminal penalty, M is the control horizon, P is the prediction horizon, and subscripts lb and ub refer to lower bound and upper bounds. Predicted error between the output variable and set point is calculated by a linear transfer function model, and $\hat{\boldsymbol{E}}(k+1)$ is defined by Equation 8.5.

$$\hat{\boldsymbol{E}}(k+1) \equiv \left[\hat{E}(k+1),\ \hat{E}(k+2), \ldots,\ \hat{E}(k+P)\right]^T \tag{8.5}$$

Similarly, $\Delta\hat{\boldsymbol{U}}(k)$ is defined according to Equation 8.6.

$$\Delta\hat{\boldsymbol{U}}(k) \equiv \left[\hat{U}(k),\ \hat{U}(k+1),\ \ldots, \hat{U}(k+M-1)\right]^T \tag{8.6}$$

In the context of the CO_2 removal rate controller from this chapter, $E \equiv Rem - 90$ and $\Delta U \equiv \Delta P_{ST,sp}$. The MPC tuning parameters are listed in Table 8.2. An MPC sampling period (Δt) of 1 min was arbitrarily chosen. The settling time (t_s) of Equation 8.2 was found to be 38 min, and this value was used to select the control and prediction horizons using the following heuristics (Seborg et al., 2011): $\frac{t_s}{3\Delta t} < M < \frac{t_s}{2\Delta t}$ and $P = M + \frac{t_s}{\Delta t}$. The diagonal elements of the output weighting matrix (q_{ii}) and input weighting matrix (r_{ii}) were determined by taking the reciprocal of the nominal values for the percent removal and pressure. The terminal penalty was set equal to half the weight applied to the prediction error vector. Constraints were applied to the change in the stripper pressure set point to avoid making aggressive moves that could lead to overpressurization or flooding. $P_{ST,sp}$ itself was not constrained in the MPC problem, although the regulatory PI pressure controller did contain upper and lower bounds on F_{CO2}. It may be necessary to add an MV constraint to the MPC formulation to improve the performance if the stripper is operating

near its pressure limit, but the pressure bounds were never violated in the results presented in the next section.

Table 8.2: MPC tuning parameters

Parameter	Value
M	15
P	53
q_{ii}	$(90\%)^{-1}$
r_{ii}	$(6 \text{ bar})^{-1}$
Q_p	$\frac{P}{2} \cdot q_{ii}$
ΔU_{lb}	-1 bar
ΔU_{ub}	+1 bar

8.3 Closed-loop Results and Discussion

The MPC problem described in the previous section was implemented in the Simulink® flowsheet from Case 4 of Chapter 5. The CO_2 removal control results in response to changes in power plant boiler load are presented in the following subsections.

8.3.1 Comparison to PI Control

Case 3 of Chapter 5 used a PI controller to manipulate F_{CO2} in order to maintain the removal set point in response to a 5% step change decrease in boiler load. Because of the positive feedback in the stripper as a result of material recycle, this strategy led to undesirable oscillatory behavior. To determine the performance improvement of the MPC implementation, the same -5% change in boiler load was tested and the results are plotted

in Figure 8.7. The PI control results with lean storage from Figure 5.7 are also replotted in Figure 8.7 for comparison. The results show that the oscillatory behavior was eliminated with the implementation of MPC because the controller now has knowledge of the expected feedback from material recycle. The system reached a new steady state with MPC in less than 1 h, showing a clear benefit to the MPC implementation. Note that initial fast changes in variables such as Rem and F_{steam} are unavoidable with any control strategy as they are a direct result of the step change in power plant load.

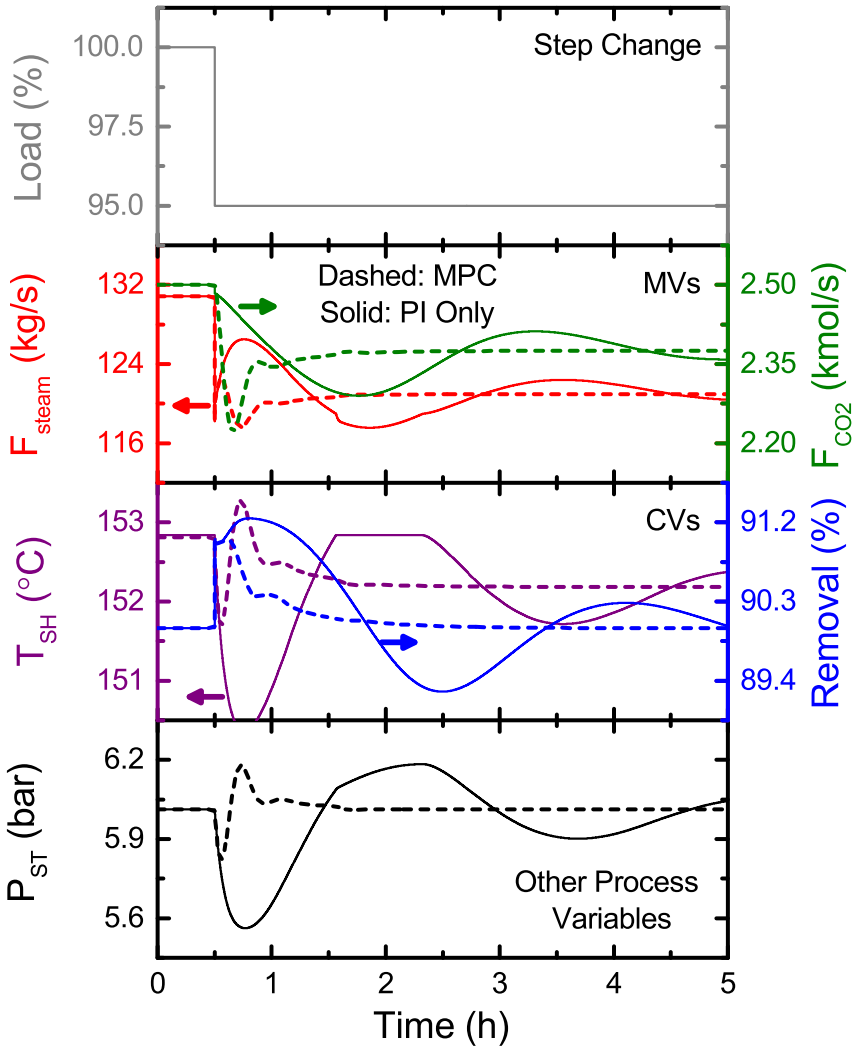

Figure 8.7: Closed-loop performance of the MPC strategy compared to the PI only strategy from Case 3 of Chapter 5

8.3.2 Load-Following Performance

The MPC strategy was also evaluated for a load-following power plant, as shown in Figure 8.8. In this scenario, the boiler load was ramped from 100% to 90% at 2%/min, held

for 1 h, and ramped back up to 100% load (top panel of Figure 8.8). The pressure set point (MV for MPC) and process pressure are plotted in the second panel of the figure. When the ramp down begins, less steam is available for solvent regeneration and P_{ST} quickly drops, despite $P_{ST,sp}$ being increased by the MPC action. After the ramp down is finished, the PI controller for P_{ST} recovers and is able to closely track the set point specified by the supervisory controller. The reverse situation occurs during the ramp up period as excess steam becomes available. The third panel of the figure shows the response of Rem in the absorber. In the ramp down case, the steam extraction valve is saturated, the flash tank temperature is uncontrolled, and α_{lean} fluctuates (bottom two panels). This resulted in a slower response for Rem than would have otherwise been observed with active temperature control. MPC is able to drive Rem to its set point quickly after the ramp up period with active temperature control. These results show that the MPC performance was somewhat diminished as a result of the steam valve design but nevertheless had reasonably good closed-loop performance without oscillation.

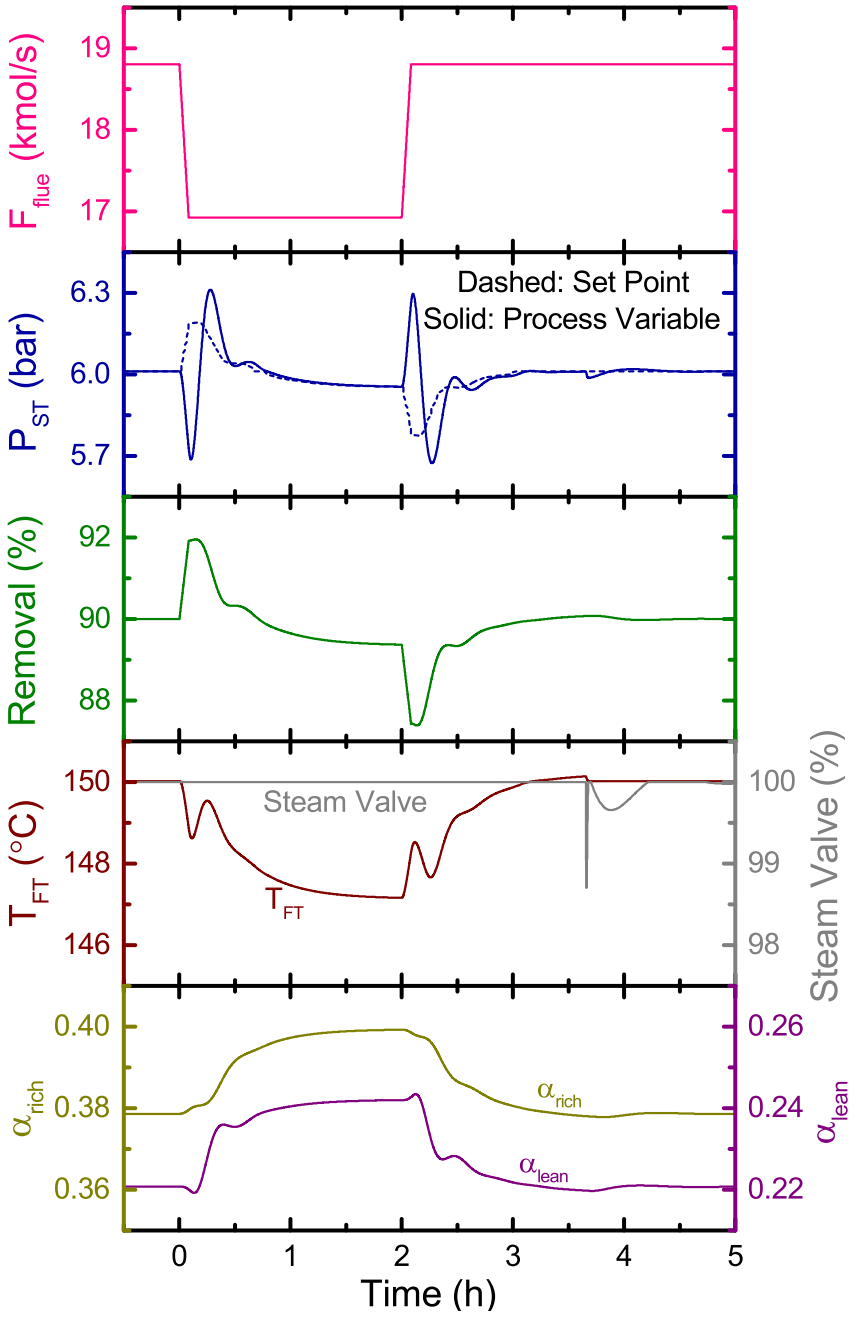

Figure 8.8: Closed-loop MPC performance for removal control with a load-following power plant

8.4 Conclusions

Linear MPC was used in a supervisory controller configuration to regulate the CO_2 removal rate in the presence of disturbances in boiler load. The manipulated variable for the SISO controller was the set point for the stripper pressure controller. Constraints were placed on the magnitude of the control moves to prevent flooding the stripper or exceeding pressure ratings. This strategy resulted in a significant improvement from controlling removal with the CO_2 stripping rate using PI control alone. When the boiler load was decreased by 5%, the MPC strategy brought the plant to steady state in 1 h, compared to over 6 hrs for the PID case. MPC also allowed removal control to be active for a load-following scenario, although the controller performance was diminished when the steam extraction valve was saturated. This SISO strategy provides a straightforward way to control removal that does not involve manipulating the solvent circulation rate, which has been proposed in the literature, and is advantageous for processes operating with small amine inventories and minimal surge capacity. Expanding the MPC problem to a multiple-input, multiple-output controller by including the solvent circulation rate and steam valve position as manipulated variables will likely provide little improvement because of constraints on surge capacity and steam availability.

Chapter 9

Conclusions and Recommendations

9.1 Summary of Work Completed

The key findings from this research on dynamic modeling and process control of post-combustion amine scrubbing are summarized here. The intent of this section is to highlight the major conclusions from the dissertation.

9.1.1 Dynamic Modeling

9.1.1.1 Low-order Model

A low-order amine scrubbing model was developed in Chapter 3 for an intercooled absorber and advanced flash stripper with aqueous piperazine. The low-order lumped parameter model uses semi-empirical thermodynamics and rate-based mass transfer, and embeds reaction kinetics in a constant overall transfer coefficient. The predicted off-design steady state of this model is compared to a high-order Aspen Plus® simulation for 100% to 85% power plant load. The difference in CO_2 removal rate between the two models is less than 1% when power plant load is greater than 94%. The removal rate is systematically over-predicted in the low-order model because a constant CO_2 mass transfer coefficient in the absorber leads to an over-prediction of absorber performance at part-load operation. Compared to pilot plant data, the low-order model captures the dynamic response of a step change in the stripper pressure control valve. The characteristic time of the total CO_2 in-

ventory is found to be 77 minutes, compared to a total liquid residence time of 48 minutes. The low-order model sufficiently represents process behavior and was used in Chapters 4, 5, 6, and 8 for process control strategy development.

9.1.1.2 Medium-order Model

Chapter 7 develops a medium-order dynamic model in gPROMS® for an absorber column with piperazine solvent that contains two packed beds separated by an in-and-out intercooler, as well as a packed water wash section. This model represents an improvement from previously published rate-based dynamic absorber models because it uses a regressed Aspen Properties® eNRTL thermodynamic model and a liquid film mass transfer coefficient correlation with an experimentally measured CO_2 loading dependence. Simulation results for off-design flue gas load were validated against a high-order steady state model, and the maximum predicted column temperature differed by less than 1.2 °C for 100–85% load. This model was used in Chapter 7 to develop a control strategy for absorber operation.

9.1.2 Process Control

9.1.2.1 Time Scale Analysis

Amine scrubbing uses extensive material and energy recycling to reduce costs and increase efficiency. As a result, the process variables exhibit a fast time scale at the unit level associated with the large recycle flows and a slow time scale at the plant level associated with the small feed and product flows. The material balances were demonstrated to be in nonstandard singularly perturbed form. Only the stripper vapor mole fractions evolve exclusively on the slow time scale in this model form; all other model states have both slow

and fast components. By applying a variable transformation, the model is arranged into standard singularly perturbed form. The slow states in this form are the overall process material hold-ups as well as the stripper vapor mole fractions. An effective control strategy for the process should control the CO_2 removal rate on the slow time scale using the small stripper overhead flowrate. Attempting to control CO_2 removal rate with the large solvent recycle rate will likely lead to an ill-conditioned controller.

9.1.2.2 Regulatory Control

Tight integration between the amine scrubbing plant, coal-fired power plant, and enhanced oil recovery (EOR) facility creates process design and control challenges for post-combustion CO_2 capture. The low-order dynamic model of the advanced amine scrubbing process and a steady state model of a 550 MWe power plant were used to examine four bounding cases that represent different system components dominating the regulatory process control strategy. Satisfying the operational and economic objectives of one system component resulted in unfavorable dynamic performance for the remainder of the system. When a step change decrease occurred in either the CO_2 delivery rate from the capture plant to the EOR facility or the steam extraction rate from the power plant to the capture plant, more than three hours were required for the amine plant to reach a new steady state. Attempting to control the CO_2 removal rate from the flue gas cannot be satisfactorily achieved through regulatory control alone. Controlling stripper temperature and pressure brought all manipulated variables to within 5% of their final steady state value in less than two hours in response to a decrease in power plant load. The design of process equipment, specifically the CO_2 stripper and steam extraction valve, depends heavily on the desired process control

strategy. The solvent surge tank should be placed in the flow of the rich solvent to allow for tighter control of absorber removal, although the difference in system performance between rich and lean surge tanks was found to be negligible when the surge tank inventory was small.

9.1.2.3 Controlling Advanced Flash Stripper Operation

The advanced flash stripper (AFS) is an intensified process design for solvent regeneration in amine scrubbing. Self-optimizing control variables were identified for the energy recovery bypass flowrates of the AFS, as well as a controller configuration for the steam extraction flowrate. Two self-optimizing variables were selected using a high-fidelity steady state process model: the temperature difference at the top of the stripper packing and the temperature difference on the hot end of the stripper overhead heat exchanger. Ranges of possible off-design conditions for the rich loading, absorber temperature, rich flowrate, and flash tank operating temperature were evaluated, and the worst case energy performance of the self-optimizing control scheme as a percentage of the true system optimum was found to be less than 1%. A low-order dynamic model was used to test the proposed self-optimizing control strategy and showed no significant control loop interactions in the closed-loop response. Cascade control, where the inner loop controlled the steam heater effluent temperature and the outer loop controlled the flash tank temperature, had favorable dynamic performance compared to a non-cascaded structure with uncontrolled flash tank temperature.

9.1.2.4 Controlling Absorber Operation

Operating the absorber at a constant liquid to gas (L/G) ratio has previously been shown to result in favorable dynamic behavior in the presence of disturbances in flue gas load, but it is unlikely that a commercial system will have a reliable flue gas flow measurement. The shape of the column temperature profile was demonstrated to be a good indicator of L/G ratio in the absence of a flue gas flow measurement, and the medium-order model was used to identify a liquid phase temperature within the top bed of absorber packing as a control variable that is sensitive to changes in L/G ratio. As the flue gas load was ramped from 100–80%, a maximum L/G ratio deviation of 0.9% from the design value was observed when controlling the column temperature with the solvent flowrate. Feedforward control may be necessary to account for other process disturbances that influence the temperature profile and was shown to be effective at counteracting a step change in intercooling temperature.

9.1.2.5 Model Predictive Control of CO_2 Removal

Single-input, single-output linear model predictive control was used as a supervisory controller to regulate the CO_2 removal rate in the presence of disturbances in boiler load. The manipulated variable was the set point for the stripper pressure controller. Constraints were placed on the magnitude of the control moves to prevent flooding the stripper or exceeding pressure ratings. This strategy resulted in a significant improvement from controlling removal with the CO_2 stripping rate using PI control alone. When the boiler load was decreased by 5%, the MPC strategy brought the plant to steady state in 1 h, compared to over 6 hrs for the PID case. MPC also allowed removal control to be active for

a load-following scenario, although the controller performance was diminished when the steam extraction valve was saturated. This SISO strategy provides a straightforward way to control removal that does not involve manipulating the solvent circulation rate, which has been proposed in the literature, and is advantageous for processes operating with small amine inventories and minimal surge capacity.

9.2 Recommendations for Future Work

9.2.1 Pilot Plant Implementation

The control strategies proposed in this work have only been evaluated with deterministic dynamic process models. Prior to commercial scale implementation of the advanced control strategies developed here, including the self-optimizing configuration from Chapter 6, the L/G control using a surrogate temperature measurement from Chapter 7, and the CO_2 removal regulation with MPC from Chapter 8, the control strategies should be tested at the pilot scale. Pilot plant testing will confirm the validity of the proposed controller design and identify areas for improvement in the event that the true process contains important process dynamics not captured by the first principles model or experiences disturbances that were not accounted for in controller design. Pilot plant testing may also expose practical limitations or constraints that were assumed to be achievable in the dynamic model.

9.2.2 Expansion of the Medium-order Model

Chapter 7 developed a medium-order dynamic model for CO_2 absorption in gPROMS®. The primary purpose of this model was to accurately predict the profiles within the absorber

column, which was important for identifying changes in L/G. While the low-order model was assumed to be sufficient to predict general process behavior for the development of regulatory and supervisory control layers, it could be advantageous to develop a plantwide medium-order amine scrubbing model. This would require that the medium-order model be expanded to include the advanced flash stripper.

A rigorous dynamic model is probably not necessary for control studies on a plant where the equipment has already been sized, which was the case for this work. However, a medium-order dynamic model could be useful for dynamic optimization, particularly for CO_2 capture from a load-following plant or for flexible capture that is dictated by electricity market dynamics. Dynamic optimization is able to optimize equipment sizes in situations where plant conditions are regularly changing. The low-order model is not appropriate for design calculations because it contains a simplified mass transfer model and parameters that are adjusted to match already specified design conditions. Developing a medium-order plantwide model in gPROMS® would be desirable to take advantage of the robust dynamic optimization tools available in the software.

9.2.3 Integrated Scheduling and Control

Several previous researchers have considered steady state scheduling problems (for example Cohen (2012)) where amine plant operation was optimized based on electricity price, grid demand, and intermittent generation by renewables. However, there is no guarantee that the control system will be able to achieve the schedule produced by the steady state optimization problem. For example, consider a summer day with rapidly increasing real-time electricity price in the afternoon due to HVAC demand. In this scenario, schedul-

ing decisions regarding the steam extraction rate from the power plant will be made over a time scale that is relevant to the process dynamics and control of the amine plant. Integrating the scheduling and control problems will allow the economic benefit of flexible capture to be realized while obeying process constraints and safety requirements (Baldea and Harjunkoski, 2014). There is potential for the low-order model to be used in future work in conjunction with a scheduling optimization problem.

Appendices

Appendix A

Low-Order Model Equations

A.1 Absorber Packed Sections

The material and energy balances for the absorber top and bottom beds (Equations A.1–A.7) assume constant molar overflow in the liquid phase and negligible total vapor phase hold-up ($\frac{dM_k^V}{dt} = 0$). It is assumed the absorber intercooler is a perfect exchanger so the liquid flow to the bottom bed is maintained at 40°C.

$$\frac{dx_{CO2,k}}{dt} = \frac{1}{M_k^L}(x_{CO2,k-1}F_{k-1}^L - x_{CO2,k}F_k^L + N_{CO2,k}) \tag{A.1}$$

$$\frac{dx_{PZ,k}}{dt} = \frac{1}{M_k^L}(x_{PZ,k-1}F_{k-1}^L - x_{PZ,k}F_k^L) \tag{A.2}$$

$$\frac{dT_k^L}{dt} = \frac{1}{Cp^L M_k^L}(\hat{H}_{k-1}^L F_{k-1}^L - \hat{H}_k^L F_k^L + N_{H,k} + N_{CO2,k}\Delta H_{CO2} + N_{H2O,k}\Delta H_{H2O}) \tag{A.3}$$

$$\frac{dy_{CO2,k}}{dt} = \frac{1}{M_k^V}(y_{CO2,k+1}F_{k+1}^V - y_{CO2,k}F_k^V - N_{CO2,k}) \tag{A.4}$$

$$\frac{dy_{N2,k}}{dt} = \frac{1}{M_k^V}(y_{N2,k+1}F_{k+1}^V - y_{N2,k}F_k^V) \tag{A.5}$$

$$\frac{dy_{O2,k}}{dt} = \frac{1}{M_k^V}(y_{O2,k+1}F_{k+1}^V - y_{O2,k}F_k^V) \tag{A.6}$$

$$\frac{dT_k^V}{dt} = \frac{1}{Cp^V M_k^V}(\hat{H}_{k+1}^V F_{k+1}^V - \hat{H}_k^V F_k^V - N_{H,k}) \tag{A.7}$$

The balance equations for the water wash section of the absorber column (Equations A.8–A.12) assume the liquid phase is pure water, so there is no liquid-side material balance. It is assumed the water recycle loop has perfect temperature control so the water temperature fed to the top of the water wash is maintained at 43.2°C, which corresponds to no accumulation or depletion of water in the system at design conditions.

$$\frac{dT_k^L}{dt} = \frac{1}{Cp^L M_k^L}(\hat{H}_{k-1}^L F_{k-1}^L - \hat{H}_k^L F_k^L + N_{H,k} + N_{H2O,k}\Delta H_{H2O}) \tag{A.8}$$

$$\frac{dy_{CO2,k}}{dt} = \frac{1}{M_k^V}(y_{CO2,k+1}F_{k+1}^V - y_{CO2,k}F_k^V) \tag{A.9}$$

$$\frac{dy_{N2,k}}{dt} = \frac{1}{M_k^V}(y_{N2,k+1}F_{k+1}^V - y_{N2,k}F_k^V) \tag{A.10}$$

$$\frac{dy_{O2,k}}{dt} = \frac{1}{M_k^V}(y_{O2,k+1}F_{k+1}^V - y_{O2,k}F_k^V) \tag{A.11}$$

$$\frac{dT_k^V}{dt} = \frac{1}{Cp^V M_k^V}(\hat{H}_{k+1}^V F_{k+1}^V - \hat{H}_k^V F_k^V - N_{H,k}) \tag{A.12}$$

A set of algebraic equations accompany the differential equations at each stage of the column (Equations A.13–A.23).

$$M_k^L = \frac{\varepsilon^L C^L \pi D^2 L}{4Ns} \tag{A.13}$$

$$M_k^V = \frac{(1-\varepsilon^L) C^V \pi D^2 L}{4Ns} \tag{A.14}$$

$$F_k^L = F_{in}^L + \sum_{K=1}^{k} N_{T,K} \tag{A.15}$$

$$F_k^V = F_{in}^V + \sum_{K=k}^{Ns} N_{T,K} \tag{A.16}$$

$$y_{H2O} = 1 - y_{CO2} - y_{N2} - y_{O2} \tag{A.17}$$

$$N_{CO2,k} = \frac{\pi D^2 L K_{g,CO2} a}{4Ns}(y_{CO2}P - P_{CO2}^*)[N_{CO2,k}^{WaterWash} = 0] \tag{A.18}$$

$$N_{H2O,k} = \frac{\pi D^2 L K_{g,H2O} a}{4Ns}(y_{H2O}P - P_{H2O}^*) \tag{A.19}$$

$$N_{T,k} = N_{CO2,k} + N_{H2O,k} \tag{A.20}$$

$$N_{H,k} = \hat{H}_k^V N_{T,k} + \frac{\pi D^2 Lha}{4Ns}(T_k^V - T_k^L) \tag{A.21}$$

$$\hat{H}_k^L = Cp^L(T_k^L - T^{ref}) \tag{A.22}$$

$$\hat{H}_k^V = Cp^V(T_k^V - T^{ref}) \tag{A.23}$$

The liquid inlet to the top of the absorber is the lean amine from the lean surge tank (set by the lean pump to maintain a constant L/G ratio) mixed with the overflow from the water wash section. The vapor inlet to the bottom section of the absorber is the flue gas after it has passed through a direct contact cooler. For the water wash, the inlet flowrate of water is given by:

$$F_{in}^L = F_{recycle}^L + F_{condensate}^L + F_{H2O} \tag{A.24}$$

where $F_{recycle}^L$ is the flowrate of water recycled from the bottom of the water wash, $F_{condensate}^L$ is the water returned from the stripper overhead condenser, and F_{H2O} is a small makeup or bleed flowrate calculated to maintain the water balance:

$$F_{H2O} = \frac{x_{PZ,lean} F_{lean}^L}{C_{PZ}^L [molality] MW_{H2O}} - x_{H2O,lean} F_{lean}^L \tag{A.25}$$

The amount of water that overflows from the water wash section to the liquid distributor at the top of the absorber section is equal to $F_{in}^L - F_{recycle}^L$.

A.2 Stripper Packing

The stripper differential equations are similar to the differential equations given in the Absorber Packed Sections Section, except there is no gas phase balance on N_2 or O_2

since the stripper gas is assumed to consist of only CO_2 and H_2O. The following two vapor phase algebraic equations are also modified from the absorber formulation:

$$F_k^V = F_{out}^V + \sum_{K=1}^{k-1} N_{T,K} \tag{A.26}$$

$$y_{H2O} = 1 - y_{CO2} \tag{A.27}$$

The outlet vapor flowrate of CO_2 (F_{CO2}) is set by either the multistage compressor (full-scale plant) or the overhead valve position (pilot plant). The total overhead vapor flowrate is calculated according to Equation A.28.

$$F_{out}^V = \frac{F_{CO2}}{y_{CO2,k=1}} \tag{A.28}$$

A.3 Constant Hold-up Liquid Inventories

The absorber sump, absorber liquid distributor, and absorber chimney tray are assumed to have a constant hold-up only in the liquid phase. For simulations that use level controllers, an additional differential equation for level (the total liquid hold-up) is also included.

$$\frac{dx_{CO2}}{dt} = \frac{4F_{in}^L}{\pi D^2 l C^L}(x_{CO2,in} - x_{CO2}) \tag{A.29}$$

$$\frac{dx_{PZ}}{dt} = \frac{4F_{in}^L}{\pi D^2 l C^L}(x_{PZ,in} - x_{PZ}) \tag{A.30}$$

$$\frac{dT^L}{dt} = \frac{4F_{in}^L}{\pi D^2 l C^L}(T_{in}^L - T^L) \tag{A.31}$$

A.4 Cross Exchanger # 1

The balance equations for the cold side (rich solvent) of CX1 are given in Equations A.32–A.34 and for the hot side (lean solvent) in Equations A.35–A.37.

$$\frac{dx_{CO2,c}}{dt} = \frac{F_c}{M_c^L}(x_{CO2,in,c} - x_{CO2,c}) \tag{A.32}$$

$$\frac{dx_{PZ,c}}{dt} = \frac{F_c}{M_c^L}(x_{PZ,in,c} - x_{PZ,c}) \tag{A.33}$$

$$\frac{dT_c^L}{dt} = \frac{1}{Cp^L M_c^L}(F_c Cp^L (T_{in,c}^L - T_c^L) + N_H) \tag{A.34}$$

$$\frac{dx_{CO2,h}}{dt} = \frac{F_h}{M_h^L}(x_{CO2,in,h} - x_{CO2,h}) \tag{A.35}$$

$$\frac{dx_{PZ,h}}{dt} = \frac{F_h}{M_h^L}(x_{PZ,in,h} - x_{PZ,h}) \tag{A.36}$$

$$\frac{dT_h^L}{dt} = \frac{1}{Cp^L M_h^L}(F_h Cp^L (T_{in,h}^L - T_h^L) - N_H) \tag{A.37}$$

The energy transfer rate is calculated in Equation A.38. To improve the numerical properties of the simulation, the Underwood approximation is used to calculate the $LMTD$.

$$N_H = UA\left(\frac{(T_{in,h}^L - T_c^L)^{1/3} + (T_h^L - T_{in,c}^L)^{1/3}}{2}\right)^3 \tag{A.38}$$

A.5 Cross Exchanger # 2

It is assumed that CX1 is operating below the bubble point of the rich amine steam. CX2 accounts for flashing that occurs in the rich stream on the cold side of the exchanger (Equations A.39–A.41). The hot side differential equations as well as the heat transfer

equation are assumed to be identical to those for CX1.

$$\frac{dz_{CO2,c}}{dt} = \frac{F_c}{M_c^L}(x_{CO2,in,c} - z_{CO2,c}) \tag{A.39}$$

$$\frac{dx_{PZ,c}}{dt} = \frac{F_c}{M_c^L}(x_{PZ,in,c} - x_{PZ,c}) \tag{A.40}$$

$$\frac{dT_c^L}{dt} = \frac{1}{Cp^L M_c^L}(F_c Cp^L(T_{in,c}^L - T_c^L) - vf \cdot F_c(y_{CO2}\Delta H_{CO2} + y_{H2O}\Delta H_{H2O}) + N_H) \tag{A.41}$$

The vapor faction (vf) and component vapor fractions (y) are determined by a numerical flash calculation using the semi-empirical thermo model.

A.6 Cross Exchanger # 3

The overhead vapor exchanger contains rich amine on the cold side and stripper gas on the hot side. Flashing from the amine solution is ignored and only sensible heat is considered on the cold side of the exchanger, so these balance equations are identical to those given for CX1. There are two contributions to heat transfer on the hot side: the cooling of the hot stripper gas and the exothermic condensation of water vapor. The hot side balance equations are shown in Equations A.42–A.43.

$$\frac{dy_{CO2,h}}{dt} = \frac{F_h^V}{M_h^V}(y_{CO2,in,h} - y_{CO2,h}) \tag{A.42}$$

$$\frac{dT_h}{dt} = \frac{1}{Cp^V M_h}(F_h^V Cp^L(T_{in,h}^V - T_h) + F_c(1 - vf)\Delta H_{H2O} - N_H) \tag{A.43}$$

The vapor fraction in this case is calculated assuming water is at its saturation pressure at the temperature of the exchanger (Equation A.44).

$$vf = \frac{y_{CO2,in,h}}{1 - P_{H2O}^{sat}/P} \tag{A.44}$$

A.7 Steam Heater

The steam heater is providing primarily latent heat to the system to flash CO_2 out of the solvent. The material and energy balances are given in Equations A.45–A.47. Like CX2, the flash calculation is done numerically with the semi-empirical thermo model.

$$\frac{dz_{CO2}}{dt} = \frac{F}{M}(z_{CO2,in} - z_{CO2}) \tag{A.45}$$

$$\frac{dx_{PZ}}{dt} = \frac{F}{M}(x_{PZ,in} - x_{PZ}) \tag{A.46}$$

$$\begin{aligned}\frac{dT}{dt} = \frac{1}{Cp^L M}(&F(Cp^L(T_{in} - T) - (vf \cdot y_{CO2} - vf_{in} \cdot y_{CO2,in})\Delta H_{CO2} \\ &- (vf \cdot y_{H2O} - vf_{in} \cdot y_{H2O,in})\Delta H_{H2O}) + Q - Q_{loss})\end{aligned} \tag{A.47}$$

A.8 Flash Tank

The flash tank has two inlets (the two-phase flow from the steam heater and the liquid exiting stage $k = Ns$ of the stripper) and two outlets (lean liquid and vapor product). Like the Constant Hold-up Liquid Inventories Section, level (total moles) is assumed to be constant for the flash tank, and the equations shown here must be modified if a level controller is included in the simulation.

$$\frac{dx_{CO2}}{dt} = \frac{4}{\pi D^2 l C^L}(F^V_{out}(x_{CO2} - y_{CO2}) + F_{in}(x_{CO2,in} - x_{CO2}) + F^L_{k=Ns}(x_{CO2,k=Ns} - x_{CO2})) \tag{A.48}$$

$$\frac{dx_{PZ}}{dt} = \frac{4}{\pi D^2 l C^L}(x_{PZ}F^V_{out} + F_{in}(x_{PZ,in} - x_{PZ}) + F^L_{k=Ns}(x_{PZ,k=Ns} - x_{PZ})) \tag{A.49}$$

$$\frac{dT^L}{dt} = \frac{4}{\pi D^2 l C^L Cp^L}(F_{in}\hat{H}_{in} + F^L_{k=Ns}\hat{H}^L_{k=Ns} - (F^L_{out} + F^V_{out})\hat{H}^L - F^V_{out}\hat{H}^V) \tag{A.50}$$

The enthalpies in the flash tank energy balance are calculated according to Equations A.51–A.54.

$$\hat{H}_{in} = Cp^L(T_{in} - T^{ref}) + vf_{in}(y_{CO2,in}\Delta H_{CO2} + y_{H2O,in}\Delta H_{H2O}) \tag{A.51}$$

$$\hat{H}^L_{k=Ns} = Cp^L(T^L_{k=Ns} - T^{ref}) \tag{A.52}$$

$$\hat{H}^L = Cp^L(T^L - T^{ref}) \tag{A.53}$$

$$\hat{H}^V = (y_{CO2}\Delta H_{CO2} + y_{H2O}\Delta H_{H2O}) \tag{A.54}$$

A.9 Lean Surge Tank

The material balance equations for the lean surge tank are given in Equations A.55–A.57. This is a surge tank with no level control, so the total mole balance is included. The trim cooler is assumed to be a perfect exchanger and always keep the lean solvent inlet temperature to the absorber at 40°C; therefore the energy balance for the lean surge tank is not included.

$$\frac{dl}{dt} = \frac{4}{\pi D^2 C^L}(F^L_{in} + F^L_{H2O} - F^L_{out}) \tag{A.55}$$

$$\frac{dx_{CO2}}{dt} = \frac{4}{\pi D^2 l C^L}((x_{CO2,in} - x_{CO2})F^L_{in} - x_{CO2}F^L_{H2O} \tag{A.56}$$

$$\frac{dx_{PZ}}{dt} = \frac{4}{\pi D^2 l C^L}((x_{PZ,in} - x_{PZ})F^L_{in} - x_{PZ}F^L_{H2O} \tag{A.57}$$

F^L_{H2O} is a makeup flow to maintain the water balance. When the low-order model is compared to the high-order model, $F^L_{H2O} = 0$ since the water wash is included. When the low-order model is compared to the pilot plant, F^L_{H2O} is calculated to achieve the desired

lean solvent molality that was measured experimentally in the pilot plant. This flow approximately represents the condensate return from the stripper overhead, but is primarily included to ensure the water balance is maintained in the simulation. Without including this flow, the simulation of the pilot plant will never come to steady state.

A.10 Condenser

The stripper overhead condenser is not explicitly included in the simulation. It is assumed to be a perfect condenser which has a liquid outlet of pure H_2O and a vapor outlet of pure CO_2, both at 40°C.

A.11 Notation

Greek

ΔH_{CO2}	heat of desorption (kJ/mol CO_2)
ΔH_{H2O}	heat of vaporization (kJ/mol H_2O)
ε	hold-up (m^3/m^3)

Roman

a	wetted area (m^2/m^3)
C	concentration (mol/m^3)

Cp	specific heat capacity (kJ/mol·K)
D	diameter (m)
F	molar flowrate (mol/s)
$\hat{H}$	specific enthalpy (kJ/mol)
h	heat transfer coefficient (kW/m^2·K)
K	mass transfer coefficient (mol/m^2·Pa·s)
L	total length of packed section (m)
l	liquid level (m)
M	total moles (mol)
MW	molecular weight (kg/mol)
N	material or energy transfer rate (mol/s or kW)
P^*	equilibrium partial pressure (Pa)
P	total pressure (Pa)
P^{sat}	saturation pressure (Pa)
Q	heat duty (kW)
T	temperature (K)
t	time (s)
UA	overall heat transfer coefficient (kW/K)
vf	vapor fraction (mol/mol)

x_i	liquid mole fraction (mol i/mol liquid)
y_i	vapor mole fraction (mol i/mol vapor)
z_i	total mole fraction (mol i/mol total)

Subscripts

c	cold side
H	energy
h	hot side
i	apparent species (CO_2, PZ, H_2O, N_2, or O_2)
k	stage number (top stage is k = 1)
$loss$	loss to surroundings

Superscripts

L	liquid
ref	reference state
T	total
V	vapor

Appendix B

Medium-Order Model Equations

B.1 Absorber Equations

Equations with boundary conditions:

$$\frac{\partial}{\partial t}\left(\varepsilon^L C_i^L\right) = -\frac{1}{L \cdot S}\frac{\partial F_i^L}{\partial z} + N_i^L \qquad i = \mathrm{CO_2}, \mathrm{H_2O}, \mathrm{PZ};\ 0 \le z < 1 \qquad \text{(B.1)}$$

$$\frac{\partial}{\partial t}\left(\varepsilon^L U^L\right) = -\frac{1}{L \cdot S}\frac{\partial F_H^L}{\partial z} + N_H^L \qquad 0 \le z < 1 \qquad \text{(B.2)}$$

$$\sum x_i = 1 \qquad 0 \le z < 1 \qquad \text{(B.3)}$$

$$\frac{1}{L \cdot S}\frac{\partial F_i^V}{\partial z} = -N_i^V \qquad i = \mathrm{CO_2}, \mathrm{H_2O}, \mathrm{N_2}, \mathrm{O_2};\ 0 < z \le 1 \qquad \text{(B.4)}$$

$$\frac{1}{L \cdot S}\frac{\partial F_H^V}{\partial z} = -N_H^V \qquad 0 < z \le 1 \qquad \text{(B.5)}$$

$$\sum y_i = 1 \qquad 0 < z \le 1 \qquad \text{(B.6)}$$

$$N_i^L = N_i^V = K_{g,i} a_e (P_i - P_i^*) \qquad i = \mathrm{CO_2}, \mathrm{H_2O};\ 0 < z < 1 \qquad \text{(B.7)}$$

$$N_H^L = N_H^V = \sum_i \left(N_i^V \bar{H}_i^V\right) + ha(T^V - T^L) \qquad 0 < z < 1 \qquad \text{(B.8)}$$

$$P = P(z = 0) - z\left(\frac{\Delta P}{\Delta z}\right) \qquad 0 < z \le 1 \qquad \text{(B.9)}$$

Equations occurring at all z, where $f(\ldots)$ denotes a call to the CAPE-OPEN physical properties package:

$$\mathit{flash} = f(P^* \cdot 10^5, vf = 0, x_{CO}) \qquad \text{(B.10)}$$

$$U^L = C^L \hat{H}^L - P \cdot 10 \qquad \text{(B.11)}$$

$$\hat{H}^V = f(T^V, P \cdot 10^5, y_{CO}) \cdot 10^{-3} \tag{B.12}$$

$$\hat{V}^V = f(T^V, P \cdot 10^5, y_{CO}) \cdot 10^{3} \tag{B.13}$$

$$x_{CO,i} = x_i \quad i = \mathrm{CO_2}, \mathrm{PZ}, \mathrm{H_2O} \tag{B.14}$$

$$x_{CO,i} = 0 \quad i \neq \mathrm{CO_2}, \mathrm{PZ}, \mathrm{H_2O} \tag{B.15}$$

$$y_{CO,i} = y_i \quad i = \mathrm{CO_2}, \mathrm{H_2O}, \mathrm{N_2}, \mathrm{O_2} \tag{B.16}$$

$$y_{CO,i} = 0 \quad i \neq \mathrm{CO_2}, \mathrm{H_2O}, \mathrm{N_2}, \mathrm{O_2} \tag{B.17}$$

$$N_{PZ}^L = 0 \tag{B.18}$$

$$N_{N2}^V = N_{O2}^V = 0 \tag{B.19}$$

$$k_{g,i}a_e = \left(\frac{1.07 \cdot 10^6}{RT^V}\right)(v^V)^{0.506}\left(\frac{D_{i-flue}}{10^4}\right)^{0.667} \quad i = \mathrm{CO_2}, \mathrm{H_2O} \tag{B.20}$$

$$K_{g,H2O}a_e = k_{g,H2O}a_e \tag{B.21}$$

$$\frac{1}{K_{g,CO2}a_e} = \frac{1}{k_{g,CO2}a_e} + \frac{1}{k'_{g,CO2}a_e} \tag{B.22}$$

$$\ln\left(k'_{g,CO2}\right) = c_{k_l} - 9.90\alpha \tag{B.23}$$

$$\alpha = \frac{x_{CO2}}{2x_{PZ}} \tag{B.24}$$

$$\frac{a_e}{a_p} = 1.34\left(\frac{\rho^L g^{1/3}\left|F^L\right|}{\sigma C^L L_p^{4/3}}\right)^{0.116} \tag{B.25}$$

$$L_p = S\left(\frac{4L_{CS}}{L_{CB} \cdot L_{crimp}}\right) \tag{B.26}$$

$$\bar{H}_i^V \equiv \left(\frac{\partial H^V}{\partial n_i}\right)_{T,P,n_{j\neq i}} \approx \frac{H_{\delta_i}^V - \hat{H}^V}{\delta i_i} \quad i = \mathrm{CO_2}, \mathrm{H_2O} \tag{B.27}$$

$$\delta i_j = 10^{-4} \quad j = i \tag{B.28}$$

$$\delta i_j = 0 \quad j \neq i \tag{B.29}$$

$$H_{\delta_i}^V = f\left(T^V, P \cdot 10^5, y_{CO} + \delta i\right) \cdot 10^{-3} \quad i = \mathrm{CO_2}, \mathrm{H_2O} \tag{B.30}$$

$$ha_e = k_{g,H2O}a_e \cdot \left(\frac{RT^V}{10^2}\right) \cdot \left(C^V Cp^V\right)^{1/3} \cdot \left(\frac{10^4 \kappa^V}{D_{H2O-flue}}\right)^{2/3} \tag{B.31}$$

$$\varepsilon^L = \left(\frac{12\mu^L a_p^2 |v^L|}{\rho^L g}\right)^{1/3} \tag{B.32}$$

$$\ln\left(\frac{\mu^L}{\mu^L_{H2O}}\right) = \left[w_{PZ}\left((420.5w_{PZ} + 1349.3)T^L + (1.352w_{PZ} + 4.224)\right)\right] \left(\frac{\alpha(9.458w_{PZ} - 0.004515T^L - 0.1584) + 1}{T^{L^2}}\right) \tag{B.33}$$

$$\ln \mu^L_{H2O} = -52.843 + \frac{3703.6}{T^L} + 5.8660 \ln T^L - 5.8790 \cdot 10^{-29}\left(T^L\right)^{10} \tag{B.34}$$

$$F^L_H = F^L \hat{H}^L \tag{B.35}$$

$$F^V_H = F^V \hat{H}^V \tag{B.36}$$

$$C^L_i = x_i C^L \quad i = \mathrm{CO_2}, \mathrm{H_2O}, \mathrm{PZ} \tag{B.37}$$

$$F^L_i = x_i F^L \quad i = \mathrm{CO_2}, \mathrm{H_2O}, \mathrm{PZ} \tag{B.38}$$

$$P^*_i = y^*_i P^* \quad i = \mathrm{CO_2}, \mathrm{H_2O} \tag{B.39}$$

$$F^V_i = y_i F^V \quad i = \mathrm{CO_2}, \mathrm{H_2O}, \mathrm{N_2}, \mathrm{O_2} \tag{B.40}$$

$$P_i = y_i P \quad i = \mathrm{CO_2}, \mathrm{H_2O} \tag{B.41}$$

$$T^L = flash.T^L \tag{B.42}$$

$$\hat{H}^L = \left(flash.\hat{H}^L \cdot 10^{-3}\right)\left(\frac{MW^L_T}{MW^L_A}\right) \tag{B.43}$$

$$C^L = \left(\frac{10^{-3}}{flash.\hat{V}^L}\right)\left(\frac{MW^L_A}{MW^L_T}\right) \tag{B.44}$$

$$\rho^L = C^L MW^L_A \tag{B.45}$$

$$C^V = \frac{1}{\hat{V}^L} \tag{B.46}$$

$$y^* = flash.y^* \tag{B.47}$$

$$x_T = flash.x_T \tag{B.48}$$

$$F^L = v^L C^L S \tag{B.49}$$

$$MW_A^L = x_{CO2} MW_{CO2} + x_{H2O} MW_{H2O} + x_{PZ} MW_{PZ} \tag{B.50}$$

$$MW^V = y_{CO2} MW_{CO2} + y_{H2O} MW_{H2O} + y_{N2} MW_{N2} + y_{O2} MW_{O2} \tag{B.51}$$

$$MW_T^L = \sum_i \left(x_{T,i} MW_i\right) \tag{B.52}$$

$$D_{i-j} = \frac{1.8583 \cdot 10^{-3} \left(T^V\right)^{3/2} \sqrt{1/MW_i + 1/MW_j}}{0.9869 P {d_{i-j}}^2 \Omega_{i-j}} \quad i,\ j = \mathrm{CO_2, H_2O, N_2};\ i \neq j \tag{B.53}$$

$$\Omega_{i-j} = 1.46 (T^V k_B / \epsilon_{i-j})^{-0.485} \quad i,\ j = \mathrm{CO_2, H_2O, N_2};\ i \neq j \tag{B.54}$$

$$D_{i-flue} = \frac{\sum_j \left(y_j D_{i-j}\right)}{\sum_j \left(y_j\right)} \quad i = \mathrm{CO_2, H_2O};\ j = \mathrm{CO_2, H_2O, N_2},\ j \neq i \tag{B.55}$$

$$\kappa^V = f\left(T^V, P \cdot 10^5, y_{CO}\right) \cdot 10^{-6} \tag{B.56}$$

$$Cp^V = f\left(T^V, P \cdot 10^5, y_{CO}\right) \cdot 10^{-3} \tag{B.57}$$

Equations that are not a function of z, where $f(\ldots)$ denotes a call to the CAPE-OPEN physical properties package:

$$F^V(z = 0) = v^V \cdot C^V(z = 0) \cdot S \tag{B.58}$$

$$\sigma = f\left(T^L(z = 1), P(z = 1), x_T(z = 1), y_{CO}(z = 1)\right) \tag{B.59}$$

Boundary conditions at $z = 0$, where in^V is the inlet vapor stream and out^L is the outlet liquid stream:

$$N_i^L = N_i^V = 0 \qquad i = \mathrm{CO_2, H_2O} \tag{B.60}$$

$$N_H^L = N_H^V = 0 \tag{B.61}$$

$$F^V = in^V.F \tag{B.62}$$

$$\hat{H}^V = in^V.\hat{H} \tag{B.63}$$

$$y = in^V.y \tag{B.64}$$

$$in^V.P = P \tag{B.65}$$

$$out^L.F = -F^L \tag{B.66}$$

$$out^L.\hat{H} = \hat{H}^L \tag{B.67}$$

$$out^L.x = x \tag{B.68}$$

Boundary conditions at $z = 1$, where out^V is the outlet vapor stream and in^L is the inlet liquid stream:

$$N_i^L = N_i^V = 0 \qquad i = \mathrm{CO_2}, \mathrm{H_2O} \tag{B.69}$$

$$N_H^L = N_H^V = 0 \tag{B.70}$$

$$F^L = -in^L.F \tag{B.71}$$

$$\hat{H}^L = in^L.\hat{H} \tag{B.72}$$

$$x = in^L.x \tag{B.73}$$

$$in^L.P = P \tag{B.74}$$

$$out^V.F = F^V \tag{B.75}$$

$$out^V.\hat{H} = \hat{H}^V \tag{B.76}$$

$$out^V.y = y \tag{B.77}$$

$$P = out^V.P \tag{B.78}$$

Since no flux was allowed at $z = 0$ or $z = 1$, the volume where mass transfer can occur is effectively shorter by one finite section at each end of the column. To account for this, the length used in the continuity equations (L) is adjusted from the actual length of

the packing (L_{act}). Note that this adjustment artificially increases the residence time of the packing by a small amount.

$$L = L_{act}\left(1 + \frac{2}{Ns}\right) \tag{B.79}$$

B.1.1 Packing Parameters and Model Constants

Table B.1: MP250X Parameters

	value
a_p (m^2/m^3)	250
L_{CS} (m)	0.017
L_{CB} (m)	0.0241
L_{crimp} (m)	0.0119

Table B.2: Model Constants

	value
Ns	50
$d_{CO2-H2O}$ (Å)	3.291
d_{CO2-N2} (Å)	3.8695
d_{H2O-N2} (Å)	3.2195
$k_B/\epsilon_{CO2-H2O}$ (1/K)	0.002516
k_B/ϵ_{CO2-N2} (1/K)	0.008471
k_B/ϵ_{H2O-N2} (1/K)	0.004161

B.2 Water Wash Equations

Equations with boundary conditions:

$$\frac{\partial}{\partial t}\left(\varepsilon^L C^L\right) = -\frac{1}{L \cdot S}\frac{\partial F^L}{\partial z} + N^L_{H2O} \qquad 0 \le z < 1 \qquad \text{(B.80)}$$

$$\frac{\partial}{\partial t}\left(\varepsilon^L U^L\right) = -\frac{1}{L \cdot S}\frac{\partial F^L_H}{\partial z} + N^L_H \qquad 0 \le z < 1 \qquad \text{(B.81)}$$

$$\frac{1}{L \cdot S}\frac{\partial F^V_i}{\partial z} = -N^V_i \qquad i = \text{CO}_2, \text{H}_2\text{O}, \text{N}_2, \text{O}_2;\ 0 < z \le 1 \qquad \text{(B.82)}$$

$$\frac{1}{L \cdot S}\frac{\partial F^V_H}{\partial z} = -N^V_H \qquad 0 < z \le 1 \qquad \text{(B.83)}$$

$$\sum y_i = 1 \qquad 0 < z \le 1 \qquad \text{(B.84)}$$

$$N^L_{H2O} = N^V_{H2O} = k_{g,H2O} a_e (P_{H2O} - P^*_{H2O}) \qquad 0 < z < 1 \qquad \text{(B.85)}$$

$$N^L_H = N^V_H = N^V_{H2O} \bar{H}^V_{H2O} + ha(T^V - T^L) \qquad 0 < z < 1 \qquad \text{(B.86)}$$

$$P = P(z = 0) - z\left(\frac{\Delta P}{\Delta z}\right) \qquad 0 < z \le 1 \qquad \text{(B.87)}$$

Equations occurring at all z, where $f(\ldots)$ denotes a call to the CAPE-OPEN physical properties package:

$$flash = f(P^* \cdot 10^5, vf = 0, x_{CO}) \qquad \text{(B.88)}$$

$$U^L = C^L \hat{H}^L - P \cdot 10 \qquad \text{(B.89)}$$

$$\hat{H}^V = f(T^V, P \cdot 10^5, y_{CO}) \cdot 10^{-3} \qquad \text{(B.90)}$$

$$\hat{V}^V = f(T^V, P \cdot 10^5, y_{CO}) \cdot 10^3 \qquad \text{(B.91)}$$

$$x_{CO,H2O} = 1 \qquad \text{(B.92)}$$

$$x_{CO,i} = 0 \quad i \neq \text{H}_2\text{O} \qquad \text{(B.93)}$$

$$y_{CO,i} = y_i \quad i = \text{CO}_2, \text{H}_2\text{O}, \text{N}_2, \text{O}_2 \qquad \text{(B.94)}$$

$$y_{CO,i} = 0 \quad i \neq \mathrm{CO_2}, \mathrm{H_2O}, \mathrm{N_2}, \mathrm{O_2} \tag{B.95}$$

$$N^V_{CO2} = N^V_{N2} = N^V_{O2} = 0 \tag{B.96}$$

$$k_{g,H2O}a_e = \left(\frac{1.67 \cdot 10^6}{RT^V}\right)(v^V)^{0.683}\left(\frac{D_{H2O-flue}}{10^4}\right)^{0.667} \tag{B.97}$$

$$\bar{H}^V_{H2O} \equiv \left(\frac{\partial H^V}{\partial n_{H2O}}\right)_{T,P,n_{j\neq H2O}} \approx \frac{H^V_{\delta_{H2O}} - \hat{H}^V}{\delta H2O_{H2O}} \tag{B.98}$$

$$\delta H2O_{H2O} = 10^{-4} \quad j = i \tag{B.99}$$

$$\delta H2O_j = 0 \quad j \neq H2O \tag{B.100}$$

$$H^V_{\delta_{H2O}} = f\left(T^V, P \cdot 10^5, y_{CO} + \delta H2O\right) \cdot 10^{-3} \tag{B.101}$$

$$ha_e = k_{g,H2O}a_e \cdot \left(\frac{RT^V}{10^2}\right) \cdot \left(C^V Cp^V\right)^{1/3} \cdot \left(\frac{10^4 \kappa^V}{D_{H2O-flue}}\right)^{2/3} \tag{B.102}$$

$$\varepsilon^L = \left(\frac{12\mu^L_{H2O}a_p^2\left|v^L\right|}{\rho^L g}\right)^{1/3} \tag{B.103}$$

$$\ln \mu^L_{H2O} = -52.843 + \frac{3703.6}{T^L} + 5.8660 \ln T^L - 5.8790 \cdot 10^{-29}\left(T^L\right)^{10} \tag{B.104}$$

$$F^L_H = F^L \hat{H}^L \tag{B.105}$$

$$F^V_H = F^V \hat{H}^V \tag{B.106}$$

$$P^*_{H2O} = y^*_{H2O} P^* \tag{B.107}$$

$$F^V_i = y_i F^V \quad i = \mathrm{CO_2}, \mathrm{H_2O}, \mathrm{N_2}, \mathrm{O_2} \tag{B.108}$$

$$P_{H2O} = y_{H2O} P \tag{B.109}$$

$$T^L = flash.T^L \tag{B.110}$$

$$\hat{H}^L = flash.\hat{H}^L \cdot 10^{-3} \tag{B.111}$$

$$C^L = \frac{10^{-3}}{flash.\hat{V}^L} \tag{B.112}$$

$$\rho^L = C^L MW^L \tag{B.113}$$

$$C^V = \frac{1}{\hat{V}^L} \tag{B.114}$$

$$y^* = flash.y^* \tag{B.115}$$

$$F^L = v^L C^L S \tag{B.116}$$

$$MW^L = MW_{H2O} \tag{B.117}$$

$$MW^V = y_{CO2} MW_{CO2} + y_{H2O} MW_{H2O} + y_{N2} MW_{N2} + y_{O2} MW_{O2} \tag{B.118}$$

$$D_{H2O-j} = \frac{1.8583 \cdot 10^{-3} \left(T^V\right)^{3/2} \sqrt{1/MW_{H2O} + 1/MW_j}}{0.9869 P {d_{H2O-j}}^2 \Omega_{H2O-j}} \quad j = \mathrm{CO_2}, \mathrm{N_2} \tag{B.119}$$

$$\Omega_{H2O-j} = 1.46 (T^V k_B / \epsilon_{H2O-j})^{-0.485} \quad j = \mathrm{CO_2}, \mathrm{N_2} \tag{B.120}$$

$$D_{H2O-flue} = \frac{\sum_j \left(y_j D_{H2O-j}\right)}{\sum_j \left(y_j\right)} \quad j = \mathrm{CO_2}, \mathrm{N_2} \tag{B.121}$$

$$\kappa^V = f(T^V, P \cdot 10^5, y_{CO}) \cdot 10^{-6} \tag{B.122}$$

$$Cp^V = f(T^V, P \cdot 10^5, y_{CO}) \cdot 10^{-3} \tag{B.123}$$

Equations that are not a function of z, where $f(\ldots)$ denotes a call to the CAPE-OPEN physical properties package:

$$F^V(z=0) = v^V \cdot C^V(z=0) \cdot S \tag{B.124}$$

$$L = L_{act}\left(1 + \frac{2}{Ns}\right) \tag{B.125}$$

Boundary conditions at $z = 0$, where in^V is the inlet vapor stream, $recycle^L$ is the outlet liquid stream set by the water wash recycle control valve, and $overflow^L$ is the liquid overflowing to the distributor for the top section of absorber packing:

$$N^L_{H2O} = N^V_{H2O} = 0 \tag{B.126}$$

$$N^L_H = N^V_H = 0 \tag{B.127}$$

$$F^V = in^V.F \tag{B.128}$$

$$\hat{H}^V = in^V.\hat{H} \tag{B.129}$$

$$y = in^V.y \tag{B.130}$$

$$in^V.P = P \tag{B.131}$$

$$overflow^L.F = -F^L - recycle^L.F \tag{B.132}$$

$$recycle^L.\hat{H} = overflow^L.\hat{H} = \hat{H}^L \tag{B.133}$$

$$recycle^L.x = overflow^L.x = x \tag{B.134}$$

Boundary conditions at $z = 1$, where out^V is the outlet vapor stream and in^L is the inlet liquid stream:

$$N^L_{H2O} = N^V_{H2O} = 0 \tag{B.135}$$

$$N^L_H = N^V_H = 0 \tag{B.136}$$

$$F^L = -in^L.F \tag{B.137}$$

$$\hat{H}^L = in^L.\hat{H} \tag{B.138}$$

$$x = in^L.x \tag{B.139}$$

$$in^L.P = P \tag{B.140}$$

$$out^V.F = F^V \tag{B.141}$$

$$out^V.\hat{H} = \hat{H}^V \tag{B.142}$$

$$out^V.y = y \tag{B.143}$$

$$P = out^V.P \tag{B.144}$$

B.3 Notation

Greek

α	loading (mol CO_2/mol alkalinity)
$\frac{\Delta P}{\Delta z}$	pressure drop through a packed section (bar/m)
δi_j	vector with small perturbation amount for i and 0 for all other j (mol)
ϵ	Lennard-Jones force constant ($s^2/m^2 \cdot kg$)
ε	liquid hold-up (m^3/m^3)
κ	thermal conductivity (MW/m·K)
μ	viscosity (Pa·s)
Ω_{i-j}	diffusion collision integral (–)
ρ	mass density (kg/m^3)
σ	surface tension (N/m)

Roman

a_e	effective wetted area of packing (m^2/m^3)
a_p	specific area of packing (m^2/m^3)
C	concentration ($kmol/m^3$)
c_{k_l}	adjustable constant (–)
Cp	specific heat capacity (MJ/kmol·K)

D	diffusion coefficient (cm^2/s)
d	diameter (m)
d_{i-j}	mean molecular diameter of i-j gas pair (Å)
F	molar or energy flowrate (kmol/s or MW)
$flash$	vector returned by CAPE-OPEN flash call (–)
g	acceleration of gravity (m/s^2)
H	enthalpy (MJ)
h	convective heat transfer coefficient ($MW/m^2 \cdot K$)
$\hat{H}$	specific enthalpy (MJ/kmol)
H_{δ_i}	enthalpy calculated with perturbed amount of i (MJ)
$\bar{H}$	partial molar enthalpy (MJ/kmol)
k_B	Boltzmann constant ($m^2 \cdot kg/s^2 \cdot K$)
K_g	overall mass transfer coefficient ($kmol/bar \cdot m^2 \cdot s$)
k_g	gas side mass transfer coefficient ($kmol/bar \cdot m^2 \cdot s$)
k'_g	liquid side mass transfer coefficient ($kmol/bar \cdot m^2 \cdot s$)
L	height (m)
L_{CB}	channel base height of packing (m)
L_{crimp}	crimp height of packing (m)
L_{CS}	channel side height of packing (m)

L_p	wetted perimeter (m)
MW	molecular weight of the liquid or vapor (kg/kmol)
MW_i	molecular weight vector returned by physical properties package (kg i/kmol)
N	material or energy flux (kmol/m^3·s or MW/m^3)
n	molar amount (kmol)
Ns	number of discretization intervals (–)
P	pressure (bar)
P^*	equilibrium pressure (bar)
R	gas constant (J/mol·K)
S	cross sectional area (m^2)
T	temperature (K)
t	time (s)
U	specific internal energy (MJ/m^3)
v	superficial velocity (m/s)
vf	vapor fraction (kmol/kmol)
$\hat{V}$	specific volume (m^3/kmol)
w	mass fraction (kg/kg)
x	liquid mole fraction (kmol/kmol)
y	vapor mole fraction (kmol/kmol)

z	normalized axial domain (m/m)

Subscripts

A	apparent
CO	CAPE-OPEN
H	energy
i	component
T	true

Superscripts

L	liquid
V	vapor

Bibliography

Åkesson, J., Laird, C. D., Lavedan, G., Prölß, K., Tummescheit, H., Velut, S., and Zhu, Y. (2012). Nonlinear model predictive control of a CO_2 post-combustion absorption unit. *Chem. Eng. Technol.*, 35:445–454.

Arce, A., Mac Dowell, N., Shah, N., and Vega, L. F. (2012). Flexible operation of solvent regeneration systems for CO_2 capture processes using advanced control techniques: Towards operational cost minimisation. *Int. J. Greenh. Gas Control*, 11:236–250.

Austgen, D. M., Rochelle, G. T., Chen, C.-C., and Peng, X. (1989). Model of vapor-liquid equilibria for aqueous acid gas-alkanolamine systems using the electrolyte-NRTL equation. *Ind. Eng. Chem. Res.*, 28(7):1060–1073.

Baldea, M. and Daoutidis, P. (2012). *Dynamics and Nonlinear Control of Integrated Process Systems*. Cambridge University Press, New York.

Baldea, M. and Daoutidis, P. (2014). A general analysis and control framework for process systems with inventory recycling. *Int. J. Robust Nonlinear Control*, 24:2852–2866.

Baldea, M. and Harjunkoski, I. (2014). Integrated production scheduling and process control: A systematic review. *Comput. Chem. Eng.*, 71:377–390.

Bequette, B. W. and Edgar, T. F. (1989). Non-interacting control system design methods in distillation. *Comput. Chem. Eng.*, 13:641–650.

Billet, R. (1995). *Packed Towers in Processing and Environmental Technology*. VCH Publishers, Inc., New York.

Billet, R. and Schultes, M. (1993). Predicting mass transfer in packed columns. *Chem. Eng. Technol.*, 16:1–9.

Bird, R. B., Stewart, W. E., and Lightfoot, E. N. (2002). *Transport Phenomena*. John Wiley & Sons, Inc., New York, second edition.

Boot-Handford, M. E., Abanades, J. C., Anthony, E. J., Blunt, M. J., Brandani, S., Mac Dowell, N., Fernández, J. R., Ferrari, M.-C., Gross, R., Hallett, J. P., Haszeldine, R. S., Heptonstall, P., Lyngfelt, A., Makuch, Z., Mangano, E., Porter, R. T. J., Pourkashanian, M., Rochelle, G. T., Shah, N., Yao, J. G., and Fennell, P. S. (2014). Carbon capture and storage update. *Energy Environ. Sci.*, 7:130–189.

Bottoms, R. R. (1930). Process for separating acidic gases. U.S. Patent No. 1,783,901. Washington, DC: U.S. Patent and Trademark Office.

Bowman, D. M. J. S., Balch, J. K., Artaxo, P., Bond, W. J., Carlson, J. M., Cochrane, M. A., DAntonio, C. M., DeFries, R. S., Doyle, J. C., Harrison, S. P., Johnston, F. H., Keeley, J. E., Krawchuk, M. A., Kull, C. A., Marston, J. B., M., M. A., Prentice, I. C., Roos, C. I., Scott, A. C., Swetnam, T. W., van der Werf, G. R., and Pyne, S. J. (2009). Fire in the earth system. *Science*, 324:481–484.

Ceccarelli, N., van Leeuwen, M., Wolf, T., van Leeuwen, P., van der Vaart, R., Maas, W., and Ramos, A. (2014). Flexibility of low-CO_2 gas power plants: Integration of the CO_2 capture unit with CCGT operation. *Energy Procedia*, 63:1703–1726.

Chen, C.-C., Britt, H. I., Boston, J. F., and Evans, L. B. (1982). Local composition model for excess Gibbs energy of electrolyte systems. Part 1: Single solvent, single completely dissociated electrolyte systems. *AIChE J.*, 28(4):588–596.

Chen, E. (2015). Evaluated pilot plant results for 5 m piperazine with the advanced flash stripper. Presented at PCCC-3. Saskatchewan, CA.

Chen, E., Fulk, S., Sache, D., Lin, Y.-J., and Rochelle, G. T. (2014). Pilot plant activities with concentrated piperazine. *Energy Procedia*, 63:1376–1391.

Chen, E., Madan, T., Sachde, D., Walters, M. S., Nielsen, P., and Rochelle, G. T. (2013). Pilot plant results with piperazine. *Energy Procedia*, 37:1572–1583.

Chen, X., Heidarinejad, M., Liu, J., and Christofides, P. D. (2012). Composite fast-slow MPC design for nonlinear singularly perturbed systems. *AIChE J.*, 58(6):1802–1811.

Cohen, S. M. (2012). *A Techno-economic Plant- and Grid-Level Assessment of Flexible CO_2 Capture*. Phd dissertation, University of Texas at Austin.

Cohen, S. M., Rochelle, G. T., and Webber, M. E. (2012a). Optimizing post-combustion CO_2 capture in response to volatile electricity prices. *Int. J. Greenh. Gas Control*, 8:180–195.

Cohen, S. M., Webber, M. E., and Rochelle, G. T. (2012b). The impact of electricity market conditions on the value of flexible CO_2 capture. In *Proc. ASME 2012 Int. Mech. Eng. Congr. Expo.*, pages 1–13, Houston, TX.

Cooke, D. H. (1983). Modeling of off-design multistage turbine pressures by Stodola's ellipse. In *Energy Incorporated PEPSE® User's Group Meeting*, pages 205–234, Richmond, VA.

Davis, J. D. (2009). *Thermal Degradation of Aqueous Amines Used for Carbon Dioxide Capture*. Phd dissertation, University of Texas at Austin.

DIPPR (2016). Design Institute for Physical Properties Project 801.

Doney, S. C., Fabry, V. J., Feely, R. A., and Kleypas, J. A. (2009). Ocean acidification: The other CO_2 Problem. *Ann. Rev. Mar. Sci.*, 1:169–192.

Dugas, R. E. (2009). *Carbon Dioxide Absorption, Desorption, and Diffusion in Aqueous Piperazine and Monoethanolamine*. Phd dissertation, University of Texas at Austin.

Dugas, R. E. and Rochelle, G. T. (2011). CO_2 absorption rate into concentrated aqueous monoethanolamine and piperazine. *J. Chem. Eng. Data*, 56(5):2187–2195.

EIA (2015). U.S. Energy-Related Carbon Dioxide Emissions, 2014.

Enaasen Flø, N., Knuutila, H., Kvamsdal, H. M., and Hillestad, M. (2015). Dynamic model validation of the post-combustion CO_2 absorption process. *Int. J. Greenh. Gas Control*, 41:127–141.

EPA (2015). Carbon pollution emission guidelines for existing stationary sources: Electric utility generating units; final rule. 40 C.F.R. § 60.

EPA (2016). SIP Processing Manual.

Frailie, P. T. (2014). *Modeling of Carbon Dioxide Absorption/Stripping by Aqueous Methyldiethanolamine/Piperazine*. Phd dissertation, University of Texas at Austin.

Freeman, S. A. (2011). *Thermal Degradation and Oxidation of Aqueous Piperazine for Carbon Dioxide Capture*. Phd dissertation, University of Texas at Austin.

Harun, N., Nittaya, T., Douglas, P. L., Croiset, E., and Ricardez-Sandoval, L. A. (2012). Dynamic simulation of MEA absorption processes for CO_2 capture from fossil fuel power plant. *Int. J. Greenh. Gas Control*, 10:295–309.

He, Z., Sahraei, M., and Ricardez-Sandoval, L. (2016). Flexible operation and simultaneous scheduling and control of a CO_2 capture plant using model predictive control. *Int. J. Greenh. Gas Control*, page In Press.

Hegglin, M. I. and Shepherd, T. G. (2009). Large climate-induced changes in ultraviolet index and stratosphere-to-troposphere ozone flux. *Nat. Geosci.*, 2:687–691.

Hinkel, J., Lincke, D., Vafeidis, A. T., Perrette, M., Nicholls, R. J., Tol, R. S. J., Marzeion, B., Fettweis, X., Ionescu, C., and Levermann, A. (2014). Coastal flood damage and adaptation costs under 21st century sea-level rise. *Proc. Natl. Acad. Sci. U.S.A.*, 111:3292–7.

IEA (2015). *CO_2 Emissions from Fuel Combustion*. OECD/IEA, Paris.

Khalilpour, R. (2014). Flexible operation scheduling of a power plant integrated with PCC processes under market dynamics. *Ind. Eng. Chem. Res.*, 53:8132–8146.

Kokotović, P., Khalil, H. K., and O'Rielly, J. (1986). *Singular Perturbation Methods in Control: Analysis and Design*. Academic Press, London.

Kroeker, K. J., Kordas, R. L., Crim, R., Hendriks, I. E., Ramajo, L., Singh, G. S., Duarte, C. M., and Gattuso, J. P. (2013). Impacts of ocean acidification on marine organisms: Quantifying sensitivities and interaction with warming. *Glob. Chang. Biol.*, 19:1884–1896.

Kvamsdal, H., Jakobsen, J., and Hoff, K. (2009). Dynamic modeling and simulation of a CO_2 absorber column for post-combustion CO_2 capture. *Chem. Eng. Process. Process Intensif.*, 48:135–144.

Lawal, A., Wang, M., Stephenson, P., Koumpouras, G., and Yeung, H. (2010). Dynamic modelling and analysis of post-combustion CO_2 chemical absorption process for coal-fired power plants. *Fuel*, 89:2791–2801.

Lawal, A., Wang, M., Stephenson, P., and Obi, O. (2012). Demonstrating full-scale post-combustion CO_2 capture for coal-fired power plants through dynamic modelling and simulation. *Fuel*, 101:115–128.

Lawal, A., Wang, M., Stephenson, P., and Yeung, H. (2009). Dynamic modelling of CO_2 absorption for post combustion capture in coal-fired power plants. *Fuel*, 88:2455–2462.

Lewis, G. N. and Randall, M. (1923). *Themodynamics and the Free Energy of Chemical Substances*. McGraw-Hill Book Company, Inc, New York, 1st edition.

Lin, Y.-J., Chen, E., and Rochelle, G. (2016). Pilot plant test of the advanced flash stripper for CO_2 capture. *Faraday Discuss.*, In Press.

Lin, Y.-J., Madan, T., and Rochelle, G. T. (2014). Regeneration with rich bypass of aqueous piperazine and monoethanolamine for CO_2 capture. *Ind. Eng. Chem. Res.*, 53:4067–4074.

Lin, Y.-J., Pan, T.-H., Wong, D. S.-H., Jang, S.-S., Chi, Y.-W., and Yeh, C.-H. (2011). Plantwide control of CO_2 capture by absorption and stripping using monoethanolamine solution. *Ind. Eng. Chem. Res.*, 50:1338–1345.

Lin, Y.-J. and Rochelle, G. T. (2016). Approaching a reversible stripping process for CO_2 capture. *Chem. Eng. J.*, 283:1033–1043.

Lüdtke, K. H. (2004). *Process Centrifugal Compressors: Basics, Function, Operation, Design, Application*. Springer-Verlag, Berlin.

Luu, M. T., Abdul Manaf, N., and Abbas, A. (2015). Dynamic modelling and control strategies for flexible operation of amine-based post-combustion CO_2 capture systems. *Int. J. Greenh. Gas Control*, 39:377–389.

Luyben, W. L. (1993). Dynamics and control of recycle systems. 1. Simple open-loop and closed-loop systems. *Ind. Eng. Chem. Res.*, 32(3):466–475.

Ma, X., Kim, I., Beck, R., Knuutila, H., and Andreassen, J. P. (2012). Precipitation of piperazine in aqueous piperazine solutions with and without CO_2 loadings. *Ind. Eng. Chem. Res.*, 51(37):12126–12134.

Massachusetts v. EPA (2007). 549 U.S. 497.

Mathias, P. M. and O'Connell, J. P. (2012). The Gibbs-Helmholtz equation and the thermodynamic consistency of chemical absorption data. *Ind. Eng. Chem. Res.*, 51:5090–5097.

Mayne, D. Q., Rawlings, J. B., Rao, C. V., and Scokaert, P. O. (2000). Constrained model predictive control: Stability and optimality. *Automatica*, 36:789–814.

Mazari, S. A., Ali, B. S., Jan, B. M., and Saeed, I. M. (2014). Degradation study of piperazine, its blends and structural analogs for CO_2 capture: A review. *Int. J. Greenh. Gas Control*, 31:214–228.

Mehleri, E. D., Mac Dowell, N., and Thornhill, N. F. (2015). *Model predictive control of post-combustion CO_2 capture process integrated with a power plant*, volume 37.

Morari, M., Arkun, Y., and Stephanopoulos, G. (1980). Studies in the synthesis of control structures for chemical processes: Part I: Formulation of the problem. Process decomposition and the classification of the control tasks. Analysis of the optimizing control structures. *AIChE J.*, 26:220–232.

Morud, J. and Skogestad, S. (1996). Dynamic behaviour of integrated plants. *J. Process Control*, 6(2-3):145–156.

NETL (2010). Cost and performance baseline for fossil energy plants, Volume 1: Bituminous coal and natural gas to electricity final report, Revsion 2.

Nittaya, T., Douglas, P. L., Croiset, E., and Ricardez-Sandoval, L. A. (2014). Dynamic modeling and evaluation of an industrial-scale CO_2 capture plant using monoethanolamine absorption processes. *Ind. Eng. Chem. Res.*, 53:11411–11426.

Oh, M. and Pantelides, C. C. (1996). Combined lumped and distributed parameter systems. *Comput. Chem. Eng.*, 20(6):611–633.

Panahi, M. and Skogestad, S. (2011). Economically efficient operation of CO_2 capturing process part I: Self-optimizing procedure for selecting the best controlled variables. *Chem. Eng. Process. Process Intensif.*, 50:247–253.

Panahi, M. and Skogestad, S. (2012). Economically efficient operation of CO_2 capturing process. Part II. Design of control layer. *Chem. Eng. Process. Process Intensif.*, 52:112–124.

Peltier, R. (2005). Genesee Phase 3, Edmonton, Alberta, Canada. *Power*, 149:46–50.

Pimm, S. L., Jenkins, C. N., Abell, R., Brooks, T. M., Gittleman, J. L., Joppa, L. N., Raven, P. H., Roberts, C. M., and Sexton, J. O. (2014). The biodiversity of species and their rates of extinction, distribution, and protection. *Science*, 344:1246752–1246752.

Piñol, D., Rodriguez, J. C., Halloran, M., Drewitz, W., Szczepanski, R., Pons, M., Woodman, M., Banks, P., and van Baten, J. (2011). Thermodynamics and physical properties.

Plaza, J. M. (2011). *Modeling of Carbon Dioxide Absorption using Aqueous Monoethanolamine, Piperazine and Promoted Potassium Carbonate*. Phd dissertation, University of Texas at Austin.

Qin, S. and Badgwell, T. A. (2003). A survey of industrial model predictive control technology. *Control Eng. Pract.*, 11:733–764.

Radić, V., Bliss, A., Beedlow, A. C., Hock, R., Miles, E., and Cogley, J. G. (2014). Regional and global projections of twenty-first century glacier mass changes in response to climate scenarios from global climate models. *Clim. Dyn.*, 42:37–58.

Rochelle, G., Chen, E., Freeman, S., Van Wagener, D., Xu, Q., and Voice, A. (2011). Aqueous piperazine as the new standard for CO_2 capture technology. *Chem. Eng. J.*, 171(3):725–733.

Rochelle, G. T. (2009). Amine scrubbing for CO_2 capture. *Science*, 325(5948):1652–1654.

Rosenzweig, C., Elliott, J., Deryng, D., Ruane, A. C., Müller, C., Arneth, A., Boote, K. J., Folberth, C., Glotter, M., Khabarov, N., Neumann, K., Piontek, F., Pugh, T. A. M., Schmid, E., Stehfest, E., Yang, H., and Jones, J. W. (2014). Assessing agricultural risks of climate change in the 21st century in a global gridded crop model intercomparison. *Proc. Natl. Acad. Sci. U.S.A.*, 111:3268–73.

Sachde, D. and Rochelle, G. T. (2014). Absorber intercooling configurations using aqueous piperazine for capture from sources with 4 to 27% CO_2. *Energy Procedia*, 63:1637–1656.

Sachde, D. J. (2016). *Absorber Performance and Configurations for CO_2 Capture Using Aqueous Piperazine*. Phd dissertation, University of Texas at Austin.

Sahraei, M. and Ricardez-Sandoval, L. (2014). Controllability and optimal scheduling of a CO_2 capture plant using model predictive control. *Int. J. Greenh. Gas Control*, 30:58–71.

Scattolini, R. (2009). Architectures for distributed and hierarchical model predictive control – A review. *J. Process Control*, 19(5):723–731.

Scherffius, J. R., Reddy, S., Klumpyan, J. P., and Armpriester, A. (2013). Large-scale CO_2 capture demonstration plant using Fluor's Econamine FG^{SM} technology at NRG's WA Parish Electric Generating Station. *Energy Procedia*, 37:6553–6561.

Seborg, D. E., Mellichamp, D. A., Edgar, T. F., and Doyle III, F. J. (2011). *Process Dynamics and Control*. John Wiley & Sons, Inc., Hoboken, NJ, 3rd edition.

Skogestad, S. (2000). Plantwide control: The search for the self-optimizing control structure. *J. Process Control*, 10:487–507.

Stéphenne, K. (2014). Start-up of world's first commercial post-combustion coal fired CCS project: contribution of Shell Cansolv to SaskPower Boundary Dam ICCS Project. *Energy Procedia*, 63:6106–6110.

Taylor, R., Krishna, R., and Kooijman, H. (2003). Modeling of distillation. *Chem. Eng. Prog.*, pages 28–39.

Trenberth, K. E., Dai, A., van der Schrier, G., Jones, P. D., Barichivich, J., Briffa, K. R., and Sheffield, J. (2014). Global warming and changes in drought. *Nat. Clim. Chang.*, 4:17–22.

Trimeric Corporation (2015). Techno-Economic Analysis for CO_2 Capture by Concentrated Piperazine with Regeneration by Advanced Flash Stripper Configuration: Budget Period 1.

Tsai, R. E., Seibert, A. F., Eldridge, R. B., and Rochelle, G. T. (2011). A dimensionless model for predicting the mass-transfer area of structured packing. *AIChE J.*, 57:1173–1184.

Voice, A. K. and Rochelle, G. T. (2013). Products and process variables in oxidation of monoethanolamine for CO_2 capture. *Int. J. Greenh. Gas Control*, 12:472–477.

Walters, M. S., Edgar, T. F., and Rochelle, G. T. (2014). Dynamic modeling, validation, and time scale decomposition of an advanced post-combustion amine scrubbing process. *Energy Procedia*, 63:1296–1307.

Walters, M. S., Edgar, T. F., and Rochelle, G. T. (2016a). Dynamic modeling and control of an intercooled absorber for post-combustion CO_2 capture. *Chem. Eng. Process. Process Intensif.*, Submitted.

Walters, M. S., Edgar, T. F., and Rochelle, G. T. (2016b). Regulatory control of amine scrubbing for CO_2 capture from power plants. *Ind. Eng. Chem. Res.*, In Press.

Walters, M. S., Lin, Y.-J., Sachde, D. J., Edgar, T. F., and Rochelle, G. T. (2016c). Control relevant model of amine scrubbing for CO_2 capture from power plants. *Ind. Eng. Chem. Res.*, 55:1690–1700.

Walters, M. S., Osuofa, J. O., Lin, Y.-J., Edgar, T. F., and Rochelle, G. T. (2016d). Process control of the advanced flash stripper for CO_2 regeneration. *Chem. Eng. Process. Process Intensif.*, Submitted.

Wang, C. (2015). *Mass Transfer Coefficients and Effective Area of Packing*. Phd dissertation, University of Texas at Austin.

Weiland, R. H., Dingman, J. C., Cronin, D. B., and Browning, G. J. (1998). Density and viscosity of some partially carbonated aqueous alkanolamine solutions and their blends. *J. Chem. Eng. Data*, 43:378–382.

Xu, Q. (2011). *Thermodynamics of CO_2 Loaded Aqueous Amines*. Phd dissertation, University of Texas at Austin.

Zaman, M. and Lee, J. H. (2015). Optimization of the various modes of flexible operation for post-combustion CO_2 capture plant. *Comput. Chem. Eng.*, 75:14–27.

Zhang, Q., Turton, R., and Bhattacharyya, D. (2016). Development of model and model predictive control of a MEA-based postcombustion CO_2 capture process. *Ind. Eng. Chem. Res.*, 55:1292–1308.

Ziaii-Fashami, S. (2012). *Dynamic Modeling, Optimization, and Control of Monoethanolamine Scrubbing for CO_2 Capture*. Phd dissertation, University of Texas at Austin.

Vita

Matthew Scott Walters was born in Edgewood, Kentucky in 1989, the son of Michael R. Walters and Denise L. Walters. He received a B.S in Chemistry and a B.S. in Chemical Engineering from Purdue University in May 2011. He began his graduate studies in Chemical Engineering at the University of Texas at Austin in the fall of 2011. While at UT, he earned a coursework M.S. degree in Chemical Engineering in 2014 and completed a graduate internship at Dow Corning as a process engineer in the summer of 2015. He has accepted a full-time position at Optimized Gas Treating upon graduation with his Ph.D. degree.

Address: walters.matthew.scott@gmail.com

This manuscript was typed by the author.